Carnegie Mellon University

CARNEGIE INSTITUTE OF TECHNOLOGY

THESIS

SUBMITTED IN PARTIAL FULFILLMENT OF THE REQUIREMENTS

FOR THE DEGREE OF Doctor of Philosophy

TITLE Modeling and Stability of the Horizontal Ribbon Growth Process

PRESENTED BY German Andrés Oliveros Patiño

ACCEPTED BY THE DEPARTMENT OF

Chemical Engineering

B. ERIK YDSTIE

B. ERIK YDSTIE, CO-ADVISOR DATE

SRIDHAR SEETHARAMAN

SRIDHAR SEETHARAMAN, CO-ADVISOR DATE

LORENZ BIEGLER

LORENZ BIEGLER, DEPARTMENT HEAD DATE

APPROVED BY THE COLLEGE COUNCIL

VIJAYAKUMAR BHAGAVATULA

DEAN DATE

Modeling and Stability of the Horizontal Ribbon Growth Process

A Dissertation

Submitted in partial fulfillment of the requirements for the degree of

Doctor of Philosophy

in

Chemical Engineering

German Andrés Oliveros Patiño

B.S., Chemical Engineering, Universidad Industrial de Santander

Carnegie Mellon University

Pittsburgh, PA

October 7, 2014

Abstract

This thesis contains a theoretical analysis of the Horizontal Ribbon Growth (HRG) process for growing silicon wafers. In the HRG process, a thin silicon ribbon is crystallized and extracted continuously from the melt, using the fact that silicon floats on its melt just like ice floats on top of water. In our work, we assess two technical issues reported in previous experimental studies: meniscus stability and interface stability.

The first law of thermodynamics along with the tools of variational calculus are used to find the existence and stability conditions of the meniscus formed between the silicon wafer and the surface of the crucible. Analytical expressions describing the shapes of the meniscii are found in terms of a single-valued function and in parametric form. These functions give the feasible configurations of the HRG system in terms of operating parameters and material properties, such as ribbon length and thickness, melt level, pulling angle, contact angle, and crucible edge geometry. From the existence conditions we show that the feasible configurations place a part or the entire meniscus above the melt level. The stability condition shows that every part of the meniscus must remain above the surface of the crucible.

A dynamic crystallization model that incorporates an extended version of the Mullins-Sekerka analysis describes the stability of the solid-liquid interface. The effect of solute segregation in the system and its effect on interface stability is measured as a function of the crystallization velocity. Two surface cooling methods -active and passive- are used to model the crystallization of a silicon ribbon of a given thickness. We show that low temperature gradients promote the homogeneous segregation of impurities in the melt, whereas high temperature gradients induce the formation of a solute enriched boundary layer. For both cases we found the thermal conditions that impede the growth of applied sinusoidal perturbations to the interface. We found that setting the crystallization model in a Lagrangean frame of reference provides an alternative way to calculate the shape of the silicon wafer.

Acknowledgements

The first person I want to thank is my advisor, professor Erik Ydstie. His sharp intellectual insight, trusting guidance and incredible patience with me, made him the best mentor I could have asked for in the past five years. Now that my work has ended, I look back and feel very glad that Erik gave me such a challenging research project. Because of this, I had many intellectually satisfying moments throughout my Ph.D.. Thank you Erik!

Within my research group, I am specially grateful with Balaji Sukumar, Sudhir Ranjan, Krishna Iyengar and Ruochen Liu. They provided me with extensive knowledge and thoughts for discussion in how to tackle the problems that the HRG project constantly poured on us. I also want thank the National Science Foundation for the financial support of my doctoral project.

I am very indebted with the many undergraduate students involved in the development of the proof of concept experiments. Ray Wang, Yijie Qiu, Jim Church, among others, successfully brought to life the theories written on paper and the models built in the computer; some of their results are included in this thesis. I also want to thank my co-advisor, professor Sridhar Seetharaman and my doctoral committee members, Paul Sides, Larry Biegler and Anthony Rollett. They provided me with constructive criticism in all the stages of my Ph.D. project.

Outside Carnegie Mellon, I am very grateful with professor Carl Laird, who was my undergraduate research advisor at Texas A&M University. Carl introduced me to the ideas of systems engineering and motivated me to pursue a Ph.D. in this area.

I am convinced that a good part of my accomplishments here at CMU are due to his teachings and the researcher mentality that I developed under his supervision. I also want to thank Oliver J. Smith at Air Products for exposing me for the first time to industrially relevant problems during the summer of 2013.

Lastly, I want to thank all my friends in Pittsburgh, Erik's research group and my family in Colombia. They were my constant support and endless source of joy.

German Andrés Oliveros Patiño

This thesis is dedicated to my parents, Germán and Gloria.

Contents

List of Figures

Chapter 1

Introduction

1.1 The photovoltaic industry

The growing need to rely less on fossil fuels for electricity generation has encouraged the development of renewable energies, such as those provided by the wind -eolic-, the sun -solar-, the ocean -tidal- and the earth itself -geothermal-. These sources of energy have existed since the beginnings of times and played various and important roles in human development until the industrial revolution. In the 21^{st} century society acknowledged their value once again, and industry started shifting their manufacturing processes to more more clean and efficient ones. Currently, the share of renewable technologies in the energy market, though increasing, is still small compared to traditional energy sources like coal and oil. According to the Renewables 2014 Global Status Report [18], fossil fuels represent 80% of the total energy consumption worlwide. This scenario is due in part to the well established energy policies that favor fossil over renewable, as well as the lack of technological breakthroughs that reduce the manufacturing costs of alternative processes.

Silicon-based photovoltaic systems are one of the most promising renewable energy sources. Covering just 0.1% of the surface of the earth with 10% efficiency solar cells can satisfy our current energy needs [23]. The capacity of PV systems continues to increase throughout the years, as we show in Figure 1.1. We see from

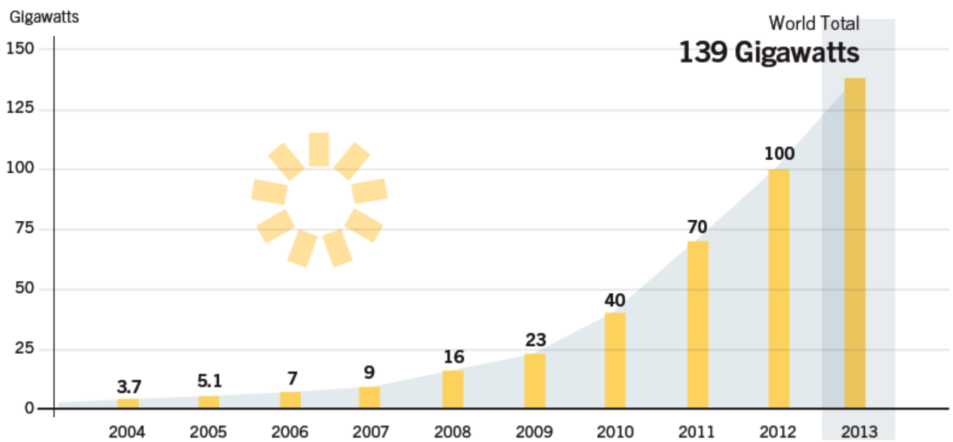

Figure 1.1: Installed solar PV Capacity from 2004 to 2013. As a point of comparison we note that a large coal plant provides about 1 GW per turbine-generator pair. Graphic taken from the Renewables 2014 Global Status Report [18].

this figure, that the worldwide capacity almost doubled from 2011 to 2013. This trend, along with the decrease in production costs and improvements in conversion efficiency [18], make continued growth in the PV markets very likely.

1.2 The solar silicon supply chain

The two current trends in the PV markets, increasing capacity and decreasing manufacturing costs, could become more pronounced by "simplifying" the solar cell supply chain. One of the most notable bottlenecks in the supply chain concerns the manufacture of the silicon wafer. The production process of the wafers is energy and capital intensive, and therefore limit the potential of the rapid expansion needed to meet the increasing demand for PV systems.

The wafering process begins with the transformation of silica into metallurgical grade silicon via thermal decomposition in an electrical arc furnace. In this part of the process, large amounts of electricity are used to break the silicon-oxygen bond.

About 10 MWh are needed per metric ton of product. The thermal decomposition brings the purity level of silicon to around 98.5%. The processed silicon is further purified via the Siemens process, in which silicon is reacted with hydrochloric acid to produce trichlorosilane (TCS). TCS is distilled to high purity and decomposed in the Siemens bell reactor where highly pure silicon (99.9999999%) is deposited. Besides being energy intensive, this process is also energy inefficient. Approximately 90% of the input power is lost through the cold walls of the bell reactor [8]. The resulting polycrystalline material is melted in large furnaces in order be grown as monocrystalline ingots via the Czochralski (CZ) process. The silicon ingots are grown batch-wise from the melt by dipping and slowly pulling a silicon seed attached to a rotating rod. The Czochralski process is also an energy intensive process since large amounts of silicon are heated at elevated temperatures for long periods of time. A posterior diamond wire-sawing process produces wafers between 100 and 600 microns in thickness. The Czochralski process along with the Bridgman (B) technique (not mentioned in this work) contribute to more than 80% of the silicon substrate used in both the semiconductor and the solar cell industry. The disadvantage of these processes is the large amount of material losses and high costs incurred in the ingot sawing; around 50% of the ingot material is lost in the sawing process. In other words, a silicon wafer is lost for each one that is produced. Also, it is difficult to realize the economy of scale observed with a batchwise operation. Scale-up of CZ- and B-processes implies duplicating equipment, resulting in a nearly linear relationship between CAPEX, OPEX and plant size. The crystal growth process represents one third of the wafer manufacturing cost, and sawing approximately another third, as we show in Figure 1.2. Developing more efficient techniques to grow the crystal and avoid the sawing process, via direct wafer growth methods, could considerably reduce the cost of the wafer significantly.

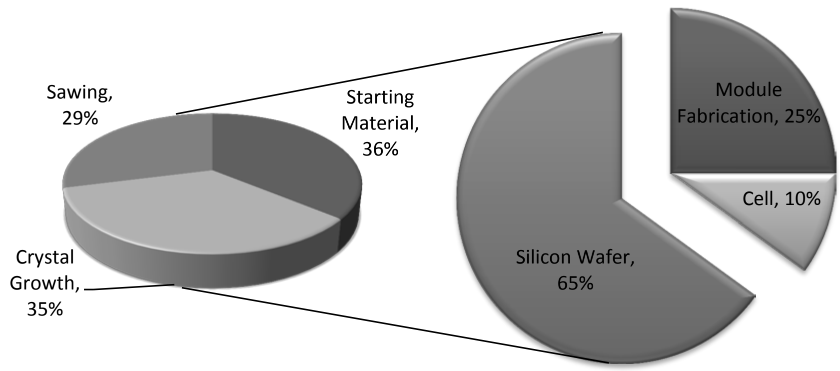

Figure 1.2: Cost distribution of a silicon wafer (2011). Adapted from Rodriguez et al. [49].

1.3 Alternative silicon wafering processes

Many processes have been proposed to produce wafers continuously and directly from the melt. Extensive research has been done in developing the scientific groundwork since the 1960s. The growth techniques can be categorized depending of the direction of pulling. Vertical growth methods include the Edge-defined Film-fed Growth (EFG) [10, 12, 58], Dendritic Web technique (WEB) [51, 52], and the String Ribbon (SR) [49]. Horizontal growth techniques include the Horizontal Ribbon Growth (HRG) [33, 3, 53], and the Ribbon Growth on Substrate (RGS) [34]. Table 1.1 compares the production rates of some of these ribbon growth technologies.

All of these processes address the two almost-conflicting issues of the future solar supply chain: to produce high quality crystals at a high production rate [9]. Technologies such as the RGS and the SR have already been commercialized, but they have not had a significant impact due to the high production cost (SR) and poor product quality (RGS). Commercialization of more mature technologies, like the EFG, the longest-living ribbon growth technology, has been recently interrupted. Others, like the HRG -the focus of this work-, are still in the research and develop-

Method	Pull Speed [cm/min]	Width [cm]	Throughput [cm^2/min]
EFG Octagon	1.65	8 x 15.6	165
WEB	1-2	8	5 - 16
STR	1-2	5-8	5-16
RGS	600-1000	15.6	7500-12500

Table 1.1: Current continuous processes to manufacture silicon ribbons and their characteristics. Adapted from [49].

ment phase. It is still not clear which emerging technique will dominate, but it is certain that a continuous process is urgently required to produce solar cell wafers

1.4 Outline of the thesis

We begin this thesis by summarizing the main scientific results obtained in the study of the Horizontal Ribbon Growth process and the technical challenges that have persisted since the discovery of the technique (Chapter 2). In Chapter 3, we address the problem of meniscus stability using the first law of thermodynamics and the methods of variational calculus. We find conditions for the existence and stability of the meniscus. The analysis is based on the first and second variation of the thermodynamic-based energy functional. This approach provides us with analytical expressions for the equilibrium height and shape of the meniscus, two findings we consider to be new. We show that the single-valued analytical solutions are stable if the conditions of existence are met. We show that this criterion is constrained by the Gibbs's pinning limits (the derivation of these are found in Appendix D). We illustrate the results by generating the feasible configurations for two different pulling angles. We validate our analytical solution with computational results reported in the literature, one concerning the HRG process, and the other two concerning the EFG process.

In Chapter 4, we address the problem of finding the additional solutions which might be unstable. We do so by resorting to Weierstrass's variational theory, for which give brief summary at the beginning of the chapter. Using Weierstrass's approach, we find analytical solutions representing the meniscus shape in parametric form and a generalized stability condition. The stability condition coincides with that derived in Chapter 3 but a range of unstable solutions are found as well. We validate the analytical solution with our own computational results. We show that the expression of the equilibrium height obtained in Chapter 2 is valid for the parametric solution as well. We find that for a given melt level height, there exist two possible confiugrations in the HRG process, one stable and one unstable. We believe this observation and the mathematical analysis that supports it is novel and hasn't been reported in the literature. We compare the shape of the unstable curves qualitatively with a proof of concept experiment, and observe that the unstable meniscus shapes are qualitatively similar to the shapes of a meniscus about to spill over from a container.

Chapter 5 deals with the issue of the impurity segregation and morphological stability of the interface. We construct a mathematical model using the Stefan [43] approach to describe the crystallization dynamics coupled with an extended version of the Mullins-Sekerka [41] formulation to analyze interface stability. The mathematical model is composed by the transient diffusion equations for heat and mass, and the interfacial moving boundary conditions for both fields. As an illustrative example, we perform the simulation of the segregation of aluminum when 50 ppm are present in the initial silicon melt. With the model we capture information about the concentration profiles in both the wafer and the melt, as well as the evolution of the temperature gradients as the ribbon grows. The extended Mullins-Sekerka formulation gives us the value of the perturbation function and hence the stability condition as a function of the position of the interface. We show that for the proposed operating parameters it is possible to achieve rates of crystallization that guarantee the formation and evolution of a stable interface. These values correspond closely to those observed experimentally by Kudo [33].

Chapter 2

The Horizontal Ribbon Growth Process

2.1 Introduction

The Horizontal Ribbon Growth (HRG) process is one of the most promising techniques for growing silicon wafers directly from the melt. In this technique, a thin crystal ribbon is produced and extracted continuously from a molten substrate. By inserting a thin film -the crystal seed- into the melt, and cooling the top surface using active and passive cooling (cooling devices and relying on heat released by radiation), it is possible to achieve the continuous production of a thin rectangular crystal from the melt. The HRG exploits a simple property of silicon: its solid phase is less dense than its liquid phase. Hence the silicon ribbon would float on top of its melt just like ice floats on top water. Its main advantage over the rest of the direct methods is its potential to achieve high growth rates since the direction of crystallization is perpendicular to the direction of pulling. In addition, the latent heat released by crystallization is easily dissipated from the surface. The HRG process does not require shaping dies or a strong reliance on surface tension forces. Also, the horizontal pulling diminishes the amount of mechanical stresses that are otherwise induced with the vertical pulling, since the ribbon is always resting on its melt. With this process it is also possible to produce wafers with large areas, in theory as large as the melt surface.

In this chapter, we summarize the efforts made in advancing the HRG technique for the past sixty years, and expose three of the main technical challenges that have been mentioned throughout the literature: melt spill-over, ribbon freeze-over and dendritic crystal growth. These three challenges motivate the work of this thesis.

2.2 A chronological review of the HRG process literature

The first design of the HRG process was proposed by William Shockley [53] at the beginning of the 1960's. In his patent, he illustrates the main ideas of the process: a planar thin film of crystal (e.g. silicon) is formed on top of a molten immiscible substrate (e.g. lead) in a furnace, by careful surface cooling close to the outlet of the system. A seeding process takes place at the outlet, allowing the thin sheet to grow in the direction opposite to the pulling direction. Pulling begins once the crystal grows and extends across a given portion of the melt surface. Inert gases are flown over the melt to prevent any undesirable reaction with ambient oxygen. Shockley was also the first to note the fact that this process serves as a purification process, similar to current industrial zone refining methods.

A decade afterwards, Carl Bleil [3], applied the concept for the first time to produce ice and germanium ribbons. In his experimental setup, he placed the crystal seed in contact with the melt and a heat sink (see Figure 2.1). Under these conditions, he claims the viability of the process if three conditions are met: 1) the crystal formed does not adhere to the sink, 2) the seed is properly placed so that it does not melt and 3) the crystal is thin enough so that it can be extracted from the crucible. In order to achieve this, he used an auxiliary heat sink to permit nucleation to occur away from the principal sink. To avoid melting of the seed, this

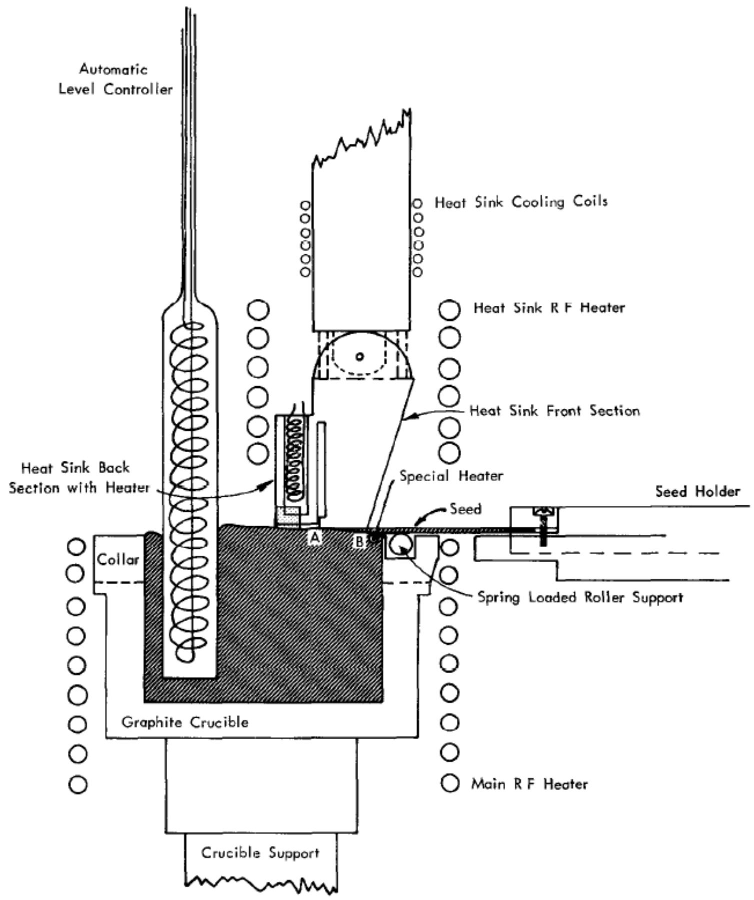

Figure 2.1: Schematic of Bleil's HRG design [3].

must cover a considerable area of the melt, extending beyond the heat sink before pulling it. Finally, the crystal can be prevented from growing too thick by implementing an independent temperature controller at the edge of the crucible. The ice and germanium ribbons he obtained in his experiments are shown in Figure 2.2. From these two photographs we see that despite the robustness of the experimental set-up, the crystals exhibit many and very visible irregularities. Bleil attributed this to the difficulty in maintaining and controlling a contant thermal heat flux to and from the ribbons.

In 1979, Bossi Kudo [33], inspired by Bleil's ideas, proposed a similar design, but

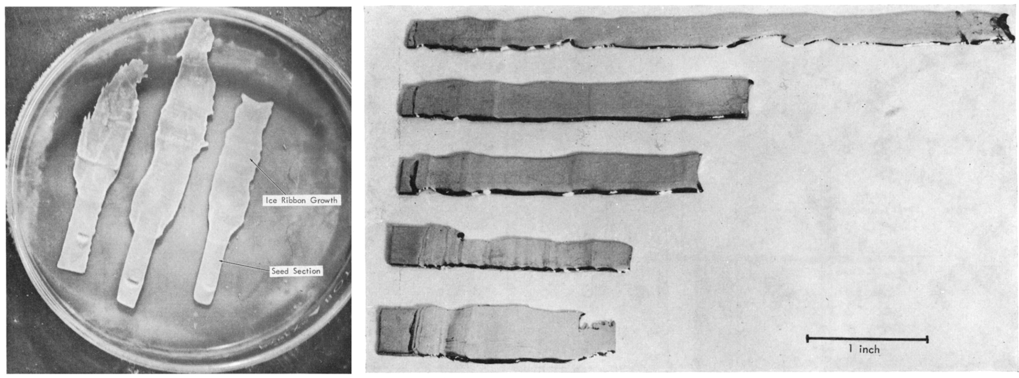

Figure 2.2: The ice and germanium ribbons obtained by Carl Bleil via the HRG process [3].

this time replacing the heat sink with a gas cooling system above the melt and close to the edge of the system. This in order to convect the heat of solidification away from the melt-crystal interface. With this improvement, Kudo successfully managed to manufacture silicon wafers for the first time in the history of the process. In his investigation he reported the pulling of polycrystalline ribbons at speeds up to 14 mm/s, and monocrystalline ribbons at speeds up to 7 mm/s. In his experiments, Kudo allowed the ribbon to achieve a large length-to-thickness ratio (approximately 10), which differed from Bleil's operation, where small ratios were used.

Despite his success, Kudo also reported several issues arising in the development of the concept. Most of them boiled down to the controllability of a system that is inherently sensitive to any perturbation and operating conditions, given the desired properties of the final product (uniform thickness and "smoothness" of a very thin film). Design issues such as the angle of the inserted seed with respect to the melt and controlling the dynamics of growth provided several complications. Also were the simultaneous supply of fresh melt and the extraction of the wafer, the excessive growth of material in a direction perpendicular to the pulling direction (down-growth) and its subsequent attempts to suppress it, the formation of polycrystalline dendritic crystals and the problem of melt spilling-over from the crucible

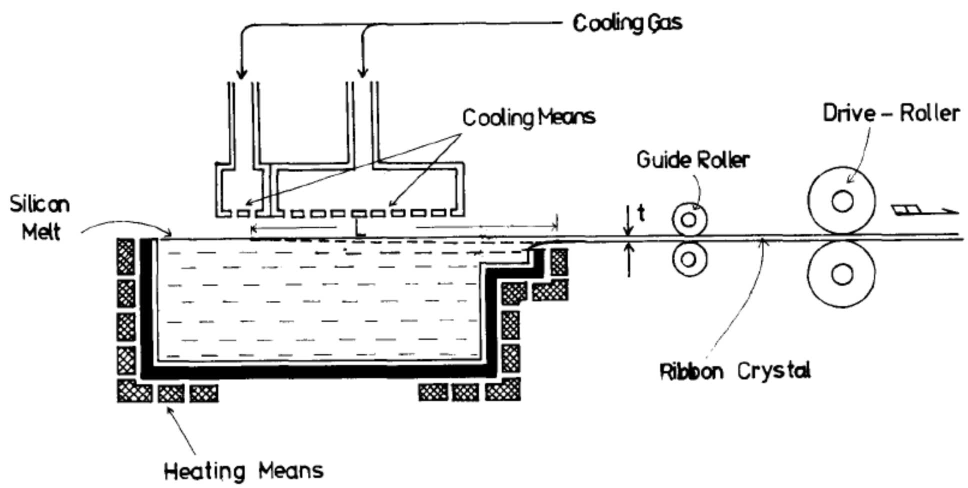

Figure 2.3: Schematic of Kudo's HRG design [33].

due to an unstable meniscus. Also mentioned but not thoroughly studied were the effects of convection in the melt, which in the case of all crystal growth processes, are of utmost importance [7]. Unfortunately, the silicon ribbons that Kudo obtained are not visible in the original research paper.

While these studies were being carried in Japan (1978-1980), John Zoutendyk [68], at the Jet Propulsion Laboratory in the United States, was evaluating the effects of forced convection in the melt due to the pulling of the seed (Zoutendyk's and Kudo's papers were published in the same journal edition). He acknowledged the influence of a velocity and thermal boundary layer underneath the melt-crystal interface and used this finding to suggest the inclusion of an "active" cooling zone (opposed to passive cooling due to radiation) in the HRG design, in order to support the crystal growth process and enhance the heat transport from the melt. Zoutendyk [67] was also the first person to develop an expression correlating the thickness and the pulling rate of the ribbon. In his theoretical model, Zoutendyk [67] assumed the ribbon to be of triangular shape, the operation to be at a steady state, and the effects of convection negligible. Under these assumptions, he used the fun-

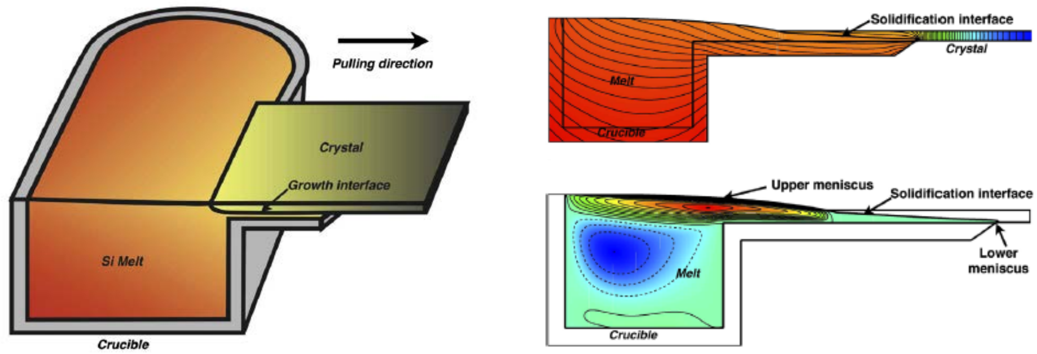

Figure 2.4: Schematic of Daggolu et.al. HRG system and its temperature and velocity profiles [44, 45].

damental energy transport equation to derive an analytical expression describing the relationship between the wafer thickness and its pulling velocity. He proved that the accuracy of his expression is valid for low values of pulling velocity. This theoretical analysis was complemented by Glicksman and Voorhess [22], where they assumed a wedge of parabolic shape. They limited the analysis to the cooling of a ribbon through a heat clamp (fixed temperature at the surface of the ribbon).

Also around 1980, Rhodes and co-workers [48] were investigating the issue of melt spill-over reported by Kudo [33] in his work. They developed a mathematical model based on hydrostatics, to describe the shape of the meniscus that must be formed between the ribbon and the crucible. They found that the hydrostatically feasible configurations, require the meniscus to be "taller" than the melt height, and that the ribbon be pulled at slight angle, which coincided with Kudo's experimental operation.

The academic output on the HRG process subsided completely from the beginnings of the 1980's until very recently. In 2012, Carl Bleil and researchers at the University of Minnesota -Parthiv Daggolu, Andrew Yeckel and Jeffrey Derby- [44, 45], started a joint project to implement a state-of-the-art computational model

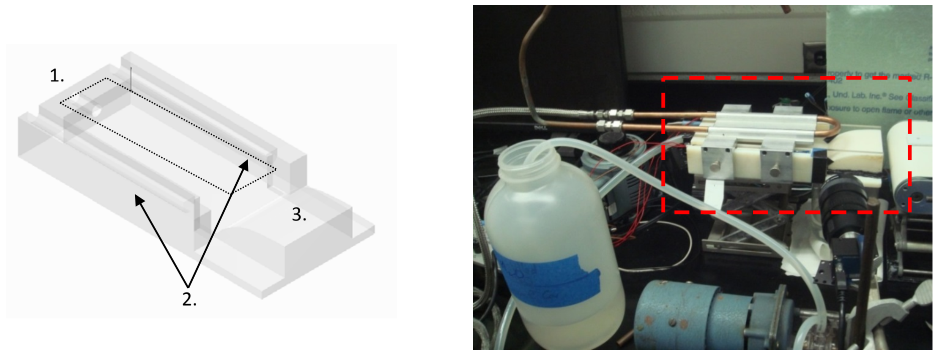

Figure 2.5: Schematic of HRG design used at CMU.

of the HRG proces. Daggolu and co-workers constructed a thermal-capillary, finite element model, describing the interaction between fluid flow and heat transfer occuring in the system, as shown in Figure 2.4. In their results, they calculated the relationship between the thickness and the pulling rate and found good agreement with Zoutendyk's [67] approximation. In addition, they were able to capture the nonlinearities in this relationship. Namely, the existence af multiple values of wedge-factors (l/t) for a given value of pulling speed. Their model also captures critical phenomena resulting in the interaction of momentum and energy transport: Marangoni currents and buoyant forces [7]. These two forces induce a vortex-type of flow at the free surfaces of the system (the melt surface and the meniscus between the ribbon and the crucible) and inside of the melt. The problems of melt spilling over and freezing to the crucible were assessed by doing a sensitivity analysis on the effects of the meniscus length as a function of the melt height and the pulling angle. Very recently, Daggolu and co-workers [15] included the effects of solute segregation in the melt in their thermal-capillary model. They found that Marangoni convection impacted the classical segregation profile seen in crystallization processes, but nonetheless the impurities kept being concentrated underneath the solid-liquid interface.

With regards to recent experimental efforts, since 2008, researchers at Carnegie

Mellon University, including the author, have been working on an experimental proof of concept of the HRG process, mimicking Kudo's design and using water as the working fluid. We constructed a small plastic bath (18 x 8 x 2.5 cm), shown in Figure 2.5, where liquid water is transported from an inlet orifice (1.) and exits through a curved surface at the end of the bath (3.) The free surface of the bath is cooled using liquid nitrogen flowing through a heat exchanger; the amount of cooling provided is controlled by the nitrogen flow from the tank and the distance between the water surface and the cold plates. The lateral walls of the bath are kept at a relatively high temperature using cartridge heaters to avoid undesired nucleation sites (2.). Once the ice sheet forms inside the bath, it is extracted by placing it on top of a conveyor belt.

In order to start the process, we used a long flat plastic piece previously cooled with liquid nitrogen and placed it into the middle of the water bath (shown in the left photograph of Figure 2.6). The cold piece acts as a nucleation point in which ice attaches preferentially since the walls of the bath are kept at a higher temperature. As ice builds up, the piece is moved by the conveyor belt outside of the system. The velocity should be high enough to prevent the attachment of the crystal to the lip of the bath and guarantee the placement of the wafer into the belt before it melts. Once the ribbon is grown and placed into the conveyor belt it was possible to keep the process running as long as there was enough traction between the ribbon and the melt (see right photograph in Figure 2.6). We found that the extraction of the film was easier if the film was slightly inclined upwards with respect to the horizontal axis, as suggested by both Kudo [33] and Rhodes [48].

Similar to previous investigations, we found that the seeding and the pulling angle play an important role in the production of the thin ribbon. With respect to the seeding, it is very difficult to know the optimal time for extracting the seed. If the seed is pulled slowly, the formation of an excessive amount of ice starts forming near the lip of the bath. If extracted too fast, the ice would get detached from the flat piece that serves as a nucleation point.

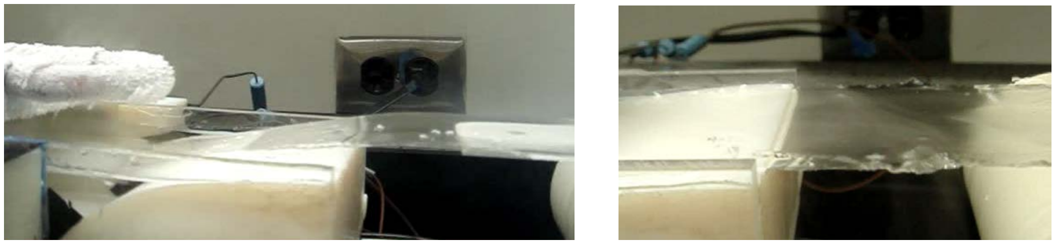

Figure 2.6: Ice ribbons obtained via the HRG process by CMU researchers.

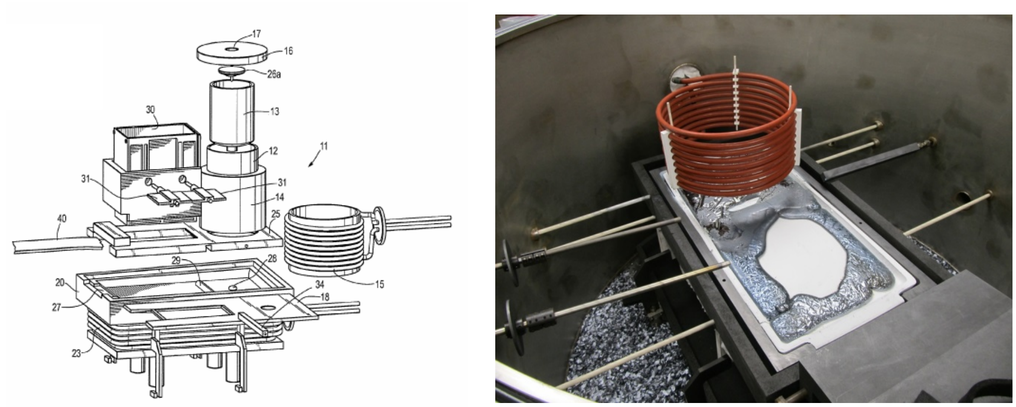

Figure 2.7: AMG Idealcast Solar Corporation HRG design.

In 2009, AMG Idealcast Solar Corporation [13] developed yet another HRG design, shown in Figure 2.7. The main parts of the system consist of a quartz crucible resting on a graphite crucible, a feed container surrounded by an induction coil, and a chimney located on top of the quartz crucible. Solid silicon chunks are melted via the induction heater and the melt is fed to the quartz crucible. A seeding process takes place close to the outlet of the furnace as the melt surface temperature is controlled by adjusting the aperture of the chimney. This equipment, now at CMU's laboratories, is currently being tested for process feasibility.

In December 2011, succesful experimental efforts were reported by researchers at Varian Semiconductor Equipment [30, 29, 27, 28, 50, 63, 31, 32, 54, 38]. Their HRG design, shown in Figure 2.8, comprises a vessel that holds the silicon melt, a

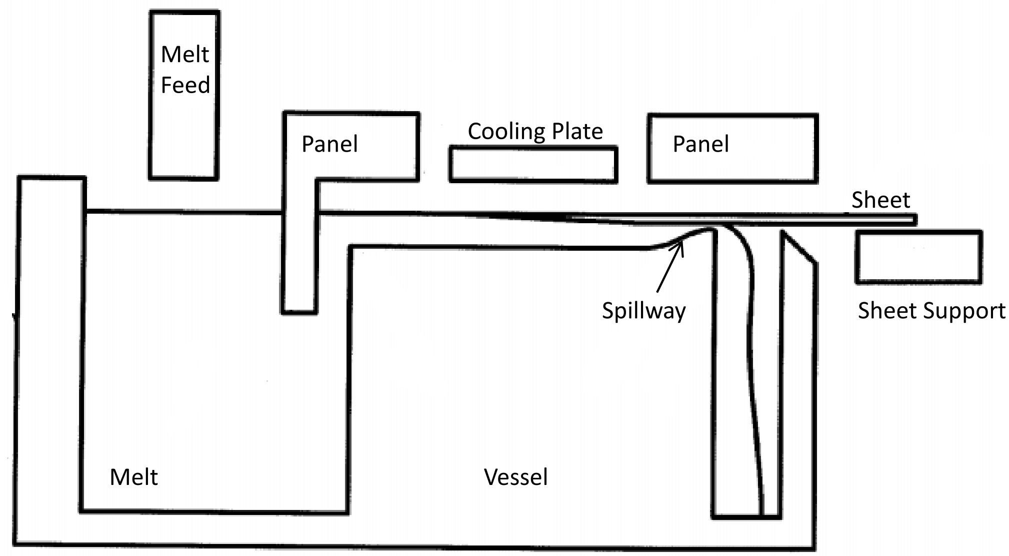

Figure 2.8: Varian Semiconductor Equipment HRG design.

set of panels and cooling plates. Molten silicon is replenished through the feed and conveyed to another section of the vessel, where the melt remains undisturbed due to the separating panel between the two sections. The outlet consists of a small ramp where the melt spills over and the ribbon is formed through a seeding process, similar to previous designs. The surface temperature is controlled by water-cooled panels located close to the surface of the melt.

Figure 2.9 shows the silicon ribbons extracted from the vessel for two different runs. The researchers were able to pull single-crystals ribbons of 2 centimeters in width, and 10 centimeters in length, at a velocity of around 0.5 mm/s (right photograph), and were able to produce a single crystal up to velocities of 2 mm/s, where dendritic growth started developing in the crystal (left photograph). These experiments are the most recent milestone in the development of the HRG technique. They attributed their success to the careful heat removal operation via the water-cooled panels, the stabilization of the meniscus provided by negative hydrostatic pressure,

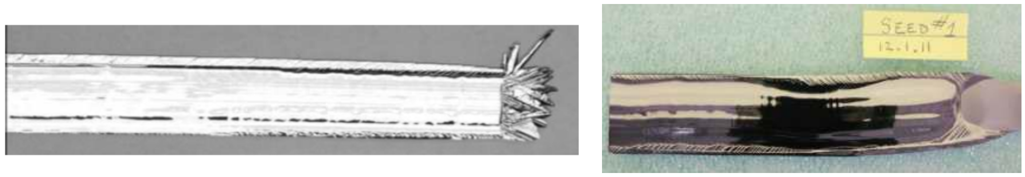

Figure 2.9: Silicon ribbons obtained by Varian Semiconductor Equipment. Ribbon to the left exhibits dendritic structure. Ribbon to the right is single crystal with (111) facets.

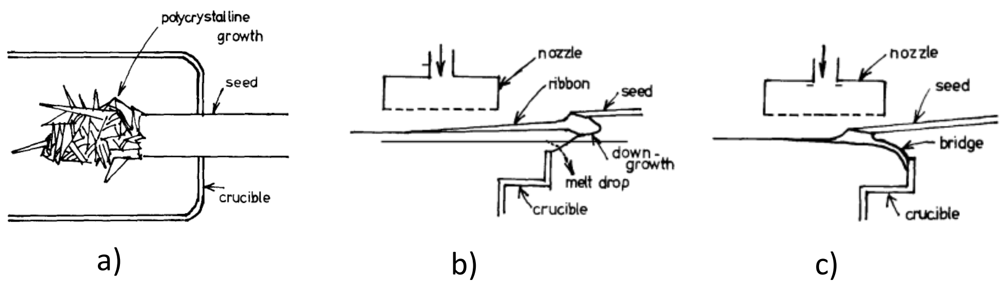

Figure 2.10: The three main technical issues in the HRG process: a) Dendritic growth, b) Melt spill-over, c) Ribbon freeze-over.

and improved seeding and extraction process. These last two were accomplished by exploiting the effect of buoyant forces in the melt and the elasticity of the formed ribbon.

2.3 Technical challenges in the HRG process

Ever since Kudo [33] first achieved the continuous extraction of the ribbon from the melt, three technical issues have constantly appeared in the reported experiments: the growth of dendrites in the crystal, the stabilization of the meniscus/melt spilling-over the crucible, and the problem of ribbon freezing into the crucible (also known as down-growth). The problem of dendritic growth have been attributed to the fluid flow disturbances in the melt (surface tension driven flow and buoyant forces) affecting the crystal growth kinetics -and therofore the micro-structure-, as well as the potential undercooling underneath the solid-liquid interface. The melt spill-over problem is attributed to incorrect seeding and growth process and inappropriate melt level control, which affect the stability of the meniscus between the ribbon and the crucible. Lastly, the freezing of the ribbon to the surface of the crucible is attributed to insufficient heat transport underneath the edge of the crucible, very low pulling angles, and insufficient melt -in the form of a meniscus- between the ribbon and the crucible.

In the following chapters we develop theoretical and computational solutions to these three main challenges, which have not yet been considered in the literature. We categorize these problems into two separate studies: meniscus stability and interface stability. The approach we take is to focus on each issue independently and study the fundamental physics that describe each problem. The analysis methods we use are based on the application of the fundamental concepts of thermodynamics and transport phenomena, and the solution methods we employ are based on variational and numerical discretization techniques.

Chapter 3

Meniscus Stability in the HRG Process. Part I: A Classical Approach

I hope that this application of analysis to one of the most curious objects of physics, may interest mathematicians, and excite them to increase more and more these applications, which unite the advantage of confirming physical theories and improving analysis itself, by requiring new processes of calculation.

– Pierre-Simon, marquis de Laplace on his theory of capillary attraction.

3.1 Introduction

The study of capillarity and meniscus stability is a necessary component in the understanding of crystal growth processes. The starting point of these studies is the well-known Young-Laplace equation, whose solution gives the shape of the meniscus as a function of the pressure exerted over it. Analytical and numerical solutions have been investigated since Laplace [35] first studied the phenomenon, and the use of these solutions in several crystal growth problems have been reported extensively for the last fifty years.

For the case of capillary-shaped systems (such as the edge-defined film-fed growth process), Tatarchenko found analytical solutions for the governing Young-Laplace equation in terms of Legendre's elliptic integrals [36], and found the conditions under which the feasible meniscii achieve concave, convexo-concave or convex shapes. The dynamic and static stability was addressed numerically by Tatarchenko [61, 62] using Lyapunov-based techniques and variational principles, respectively. For the specific case of the EFG process, the effects of capillarity and the shape of the feasible meniscii were calculated numerically by Swartz, Surek, Chalmers and Mlavksy [58, 59]; the problem of stability was addressed by Surek [56] using fact that the contact angle between the crystal and the melt should converge towards a constant value (11° in the case of silicon), for a given change in the shape of the crystal. For the Czochralski process a capillary analysis was developed by Hurle [26, 25] to find an approximate analytical solution of the shape of the meniscus in the Czochralski growth. For the Czochralski process a linearization of one of the principal curvatures is made in order to obtain a solution in analytical form. The shapes and static stability of the meniscii were also analyzed by Mika and Uelhoff [40] using a combined analytical and numerical approach. Using the concept of meniscus energy minimization along with the formalism of variational calculus, they found stationary curves which are unstable beyond a certain joining angle. For the case of the Bridgman process, analytical approximations and numerical studies regarding the shapes of meniscii have been reported by Braescu et al. [5, 6], Epure et al. [16] and by Volz and Mazuruk [65]. Very recently, Volz and Mazuruk [39] also addressed the static stability problem using numerical simulations to solve the governing variational problem.

A continuous crystallization process that has yet to produce substantial understanding meniscus stability is the HRG process. One of the principal problems reported by Kudo [33] was the freezing of the ribbon to the end lip of the crucible, also known as down-growth. The reason for down-growth is that there is no melt

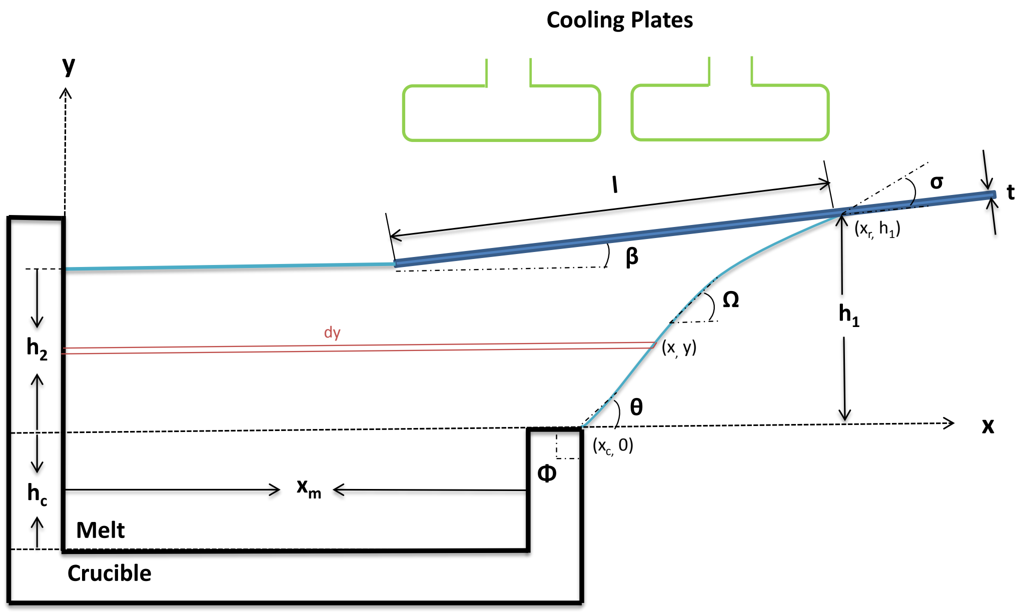

Figure 3.1: Representation of the Horizontal Ribbon Growth. A meniscus must be formed between the ribbon and the crucible to prevent melt spill-over and ribbon freeze-over.

present between the ribbon and the crucible, in the form of a meniscus. The solid surface of the crucible provide nucleation points for the ribbon to crystallize onto it as it is being pulled. The opposite problem can also arise: an excess of melt flow that causes the melt to spill over the crucible. In an ideal operation, a space between the ribbon and the lip of the crucible is maintained to avoid undesired nucleation points, and a meniscus is pinned between the crucible lip and the ribbon, to avoid melt spill-over, as illustrated in Figure 3.1.

Conditions that guarantee the existence of the meniscus and its pinning at the corner would solve these two problems. The issue was first addressed around the same time of Kudo's experiments by Rhodes and co-workers [48]. In their study, they used a mathematical model based on fluid hydrostatics to describe the section of the HRG process where down-growth takes place (depicted in Figure 3.1 as well).

Using numerical methods they determined the shape of the meniscus for several operating conditions as well as the relationship between melt height and meniscus height. They concluded from the computer simulations that in order to obtain a statically stable meniscus, the melt height should be below the meniscus height ($h_2 < h_1$) and therefore a slightly inclined pulling angle would be propitious for the stable operation of the process. In two recent papers, Daggolu et al. [44, 45], using a thermal-capillary model, analyzed the relationship between the pulling rate of the ribbon and the length of the meniscus. Using numerical simulations, they found a critical value of the pulling velocity for which the meniscus recedes and the melt spills over. They also found that due the highly non-linear dynamics of the process, multiple solutions for the meniscus length exist for a given pulling velocity. The numerical studies of Rhodes et al. [48] and Daggolu et al. [44, 45] raise the question whether it is possible to derive a general theory for the stability of the lower meniscus in the HRG process.

In this chapter we use an energy-based model to calculate the shapes and stability of the meniscus in the HRG process. Analog to the work of Pitts [46] and Mika et al. [40], we use the first law of thermodynamics to construct an energy functional, and, using variational principles, calculate the shape and stability of the meniscus. We first give a brief overview of the fundamental variational concepts, mainly, the Euler-Lagrange equation, used to calculate stationary curves, and the Legendre and Jacobi tests to find whether the stationary curve is stable or not. By solving analytically the Euler-Lagrange equation derived from the first variation (which is equivalent to the governing Young-Laplace equation), we find the shape of the meniscus as function of the operating parameters of the system, such as the pulling angle and the geometry of the wafer. Once the existence conditions have been found, we use the second variation (Legendre's and Jacobi's tests) to prove that the curves found by the analytical solution are stable. Based on this analysis, we show a straighforward practical methodology to find the existence of hydrostatically permissible configurations of the HRG system.

3.2 Fundamentals of the calculus of variations

The calculus of variations deals with integrals of the form [20]

$$U_0 = \int_0^{H_1} F\left(Y, X, \frac{dX}{dY}\right) dY, \tag{3.1}$$

where F represents a given functional form, and the relationship between X and Y is not known. The problem consists in finding the function $X(Y)$ for which U_0 is a maximum or a minimum. In many applications, including the study of capillary stability, U_0 represents the energy of the system.

The problem is solved as follows: let $X(Y)$ be the equation of a stationary curve, and let $X(Y) + \epsilon W(Y)$ a perturbation to such curve, where ϵ is a "small" arbitrary constant and $W(Y)$ is any arbitrary function of Y that satisfies

$$W(0) = 0 \quad \text{and} \quad W(H_1) = 0. \tag{3.2}$$

These type of perturbations are usually referred to as weak variations. The concept is illustrated in Figure 3.3.

We represent the integral for which U_0 is stationary by

$$U_0^s = \int_0^{H_1} F(Y, X_s, X_s')\, dY, \tag{3.3}$$

and the neighbouring curve by

$$U_0^s + \delta U_0^s = \int_0^{H_1} F(Y, X_s + \epsilon W, X_s' + \epsilon W')\, dY. \tag{3.4}$$

In these last two expressions, the prime represents differentiation with respect to Y. Expanding the right hand side term of the last equation in a Taylor series expansion around the stationary curve we have

$$\begin{aligned} F(Y, X + \epsilon W, X' + \epsilon W') = F(Y, X, X') + \epsilon \left(W \frac{\partial F}{\partial X} + W' \frac{\partial F}{\partial X'} \right) + \\ \frac{\epsilon^2}{2} \left(W^2 \frac{\partial^2 F}{\partial X^2} + 2WW' \frac{\partial^2 F}{\partial X \partial X'} + W'^2 \frac{\partial^2 F}{\partial X'^2} \right) + O(\epsilon^3). \end{aligned} \tag{3.5}$$

So we can represent the variation in the energy as

$$\begin{aligned}\delta U_0^s = \epsilon \int_0^{H_1} \left(W \frac{\partial F}{\partial X} + W' \frac{\partial F}{\partial X'} \right) dY + \\ \frac{\epsilon^2}{2} \int_0^{H_1} \left(W^2 \frac{\partial^2 F}{\partial X^2} + 2WW' \frac{\partial^2 F}{\partial X \partial X'} + W'^2 \frac{\partial^2 F}{\partial X'^2} \right) dY + O(\epsilon^3).\end{aligned} \tag{3.6}$$

The first term on the right hand side of the equation is referred to as the first variation and the second term as the second variation. Neglecting the higher order terms of ϵ, it is clear from this expression that if δU_0^s is negative then U_0 is a maximum, and if δU_0^s is positive then U_0 is a minimum. Given the structure of these two integrals, we also see that the sufficient conditions for having a maximum are that the first variation of the energy function vanishes and its second variation is less than zero. Similarly the sufficient conditions for a minimum are that the first variation vanishes and the second variation is greater than zero. The findings of Euler, Legendre and Jacobi allowed for a very convenient treatment of the first and second variation, and are summarized in the next sections.

3.2.1 The first variation

In 1744, Leonhard Euler (1707-1783) discovered an expression that, when satisfied, yields the stationary curves of U_0, which make the first variation equal to zero. The first variation in equation (3.6) can be transformed since

$$\int_0^{H_1} W' \frac{\partial F}{\partial X'} dY = W \frac{\partial F}{\partial X'}\bigg|_{Y=0} - W \frac{\partial F}{\partial X'}\bigg|_{Y=H_1} - \int_0^{H_1} W \frac{d}{dY} \left(\frac{\partial F}{\partial X'} \right) dY, \tag{3.7}$$

and $W(0) = W(H_1) = 0$. So the expression for the vanishing of first variation can be expressed as

$$\int_0^{H_1} W \left[\frac{\partial F}{\partial X} - \frac{d}{dY} \left(\frac{\partial F}{\partial X'} \right) \right] dY = 0. \tag{3.8}$$

From this expression Euler deduced that if W is an arbitrary function of Y, then the above equation can be satisfied if and only if

$$\frac{\partial F}{\partial X} - \frac{d}{dY} \left(\frac{\partial F}{\partial X'} \right) = 0, \tag{3.9}$$

for all values of Y between 0 and H_1. The solution to this equation yields the stationary curves $X(Y)$ of U_0. We summarize this result in the following theorem:

FUNDAMENTAL THEOREM I (Euler): *Every function X(Y) which minimizes or maximizes the integral*

$$U_0 = \int_0^{H_1} F(Y, X, X')\, dY, \tag{3.10}$$

must satisfy the differential equation

$$\frac{\partial F}{\partial X} - \frac{d}{dY}\left(\frac{\partial F}{\partial X'}\right) = 0. \tag{3.11}$$

This equation is commonly known as the Euler-Lagrange equation, and represents the first building block in the development of the calculus of variations.

3.2.2 The second variation

Once a stationary curve is found by means of the Euler-Lagrange equation, it is necessary to find whether such curve represents a maximum or a minimum. For a stationary curve, the total variation reduces to

$$\delta U_0^s = \frac{\epsilon^2}{2}\int_0^{H_1}\left(W^2\frac{\partial^2 F}{\partial X^2} + 2WW'\frac{\partial^2 F}{\partial X\partial X'} + W'^2\frac{\partial^2 F}{\partial X'^2}\right) dY. \tag{3.12}$$

In this expression we neglected the terms of third order and higher. In order to prove that U_0 is a minimum, we need to show that the sign of δU_0^s is positive regardless of the choice of $W(Y)$. In the same manner, in order to prove that U_0 is a maximum we need to show that the sign of the second variation is negative.

In 1786, Adrien-Marie Legendre discovered a necessary criterion to distinguish between a maximum or a minimum. He added to the expression of the second variation the following term

$$\frac{\epsilon^2}{2}\int_0^{H_1}(2WW'Z + W^2Z')dY, \tag{3.13}$$

where Z is an arbitrary function of Y. This integral is equal to zero since

$$\int_0^{H_1}\frac{d}{dY}(W^2Z)dY = \epsilon\left(W^2Z\Big|_{Y=H_1} - W^2Z\Big|_{Y=0}\right), \tag{3.14}$$

and W vanishes at the end points. Legendre thus converts the expression for the second variation into

$$\delta U_0^s = \frac{\epsilon^2}{2}\int_0^{H_1}\left[\left(\frac{\partial^2 F}{\partial X^2}+Z'\right)W^2+2\left(\frac{\partial^2 F}{\partial X\partial X'}+Z\right)WW'+\frac{\partial^2 F}{\partial X'^2}W'^2\right]dY, \tag{3.15}$$

and finds the arbitrary function Z using the condition that the discriminant of the quadratic form in the variables W and W' in the integrand vanish:

$$\left(\frac{\partial^2 F}{\partial X\partial X'}+Z\right)^2-\frac{\partial^2 F}{\partial X'^2}\left(\frac{\partial^2 F}{\partial X^2}+Z'\right)=0. \tag{3.16}$$

This reduces the the second variation to the following expression:

$$\delta U_0^s = \frac{\epsilon^2}{2}\int_0^{H_1}\left(\frac{\partial^2 F}{\partial X'^2}\left(W'+\frac{\frac{\partial^2 F}{\partial X\partial X'}+Z}{\frac{\partial^2 F}{\partial X'^2}}W\right)^2\right)dY. \tag{3.17}$$

From this expression, Legendre concludes that $\partial^2 F/\partial X'^2$ must not change sign in the interval $(0, H_1)$. We summarize this result in the following theorem:

FUNDAMENTAL THEOREM II (Legendre): *For a minimum (maximum) it is necessary that*

$$\frac{\partial^2 F}{\partial X'^2}\geq 0 \quad (\leq 0) \quad \text{in} \quad (0, H_1). \tag{3.18}$$

This is commonly known as Legendre's test and it is a necessary condition for an extrema.

We are only left with the study of the differential equation (3.16); Legendre's condition is valid if and only if there exist an integral to such equation that is continuous and finite. In 1837, Karl Jacobi (1804-1851) analyzed this differential equation by using the change variable

$$Z = -\frac{\partial^2 F}{\partial X\partial X'}-\frac{\partial^2 F}{\partial X'^2},\frac{V'}{V}, \tag{3.19}$$

transforming (3.16) into

$$\left[\frac{\partial^2 F}{\partial X^2}-\frac{d}{dY}\left(\frac{\partial^2 F}{\partial X\partial X'}\right)\right]V-\frac{d}{dY}\left(\frac{\partial^2 F}{\partial X'^2}\frac{dV}{dY}\right)=0. \tag{3.20}$$

This equation is commonly known as Jacobi's differential equation or Jacobi's accesory equation. If V has a solution different from zero throughout $(0, H_1)$ then the solution forms an integral for W as well. However, if the integral vanishes at least at one point, then Legendre's construction is not applicable throughout the interval $(0, H_1)$, and no conclusion can be established on the nature of the stationary curve.

Jacobi's criterion is usually put in terms of the concept of conjugate points. We say that if there exists a point P between 0 and H_1 such that $V(0) = V(P) = 0$ with $V(Y) \neq 0$ for all $Y \in (0, H_1)$, then P is a point conjugate to 0. The concept is illustrated in Figure 3.2.

Jacobi's accesory equation is linear and homogeneous, therefore if any nonzero solution $V(Y)$ has a conjugate point, every constant multiple of it (e.g. $kV(Y)$) will also have a conjugate point. If we can find any nonzero solution that doesn't vanish in the interval $(0, H_1)$ then Jacobi's test is satisfied. Without loss of generality we thus impose

$$V(0) = 0 \quad \text{and} \quad \left. \frac{dV}{dY} \right|_{Y=0} = 1, \tag{3.21}$$

and find whether the solution $V(Y)$ has any conjugate points. We summarize this analysis in the following theorem:

FUNDAMENTAL THEOREM III (Jacobi): *Let $X = F(Y)$ be the equation of the extremal through the points 0 and H_1 for which the integral $U_0 = \int_0^{H_1} F(Y, X, X')\, dY$ is stationary. Let 0 and P be two adjacent conjugate points on the curve. If H_1 lies between 0 and P and $\frac{\partial^2 F}{\partial X'^2}$ has constant sign for all points of the arc $(0, H_1)$, then for weak variations U_0 is a maximum when $\frac{\partial^2 F}{\partial X'^2}$ is negative and a minimum when it is positive.*

In the next section we show that, in our HRG system, the stationary curve defines the meniscus located between the ribbon and the surface of the crucible (see Figure 3.3), and is calculated by solving the Euler-Lagrange equation. The stability of the feasible meniscii with respect to weak variations is calculated using Legendre's and Jacobi's analyses.

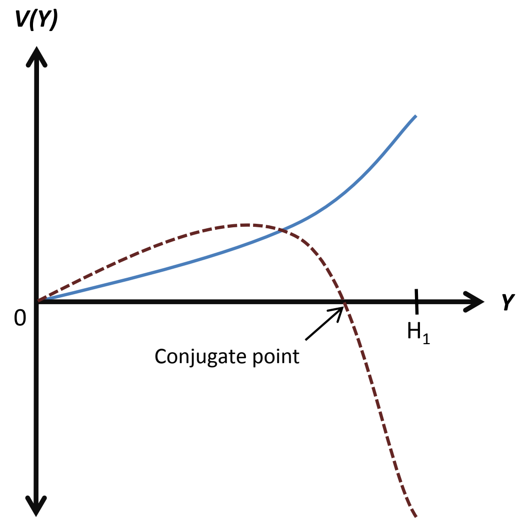

Figure 3.2: Two possible solutions of a Jacobi differential equation, dashed line has a conjugate point.

3.3 Problem statement

In order to address the issues of melt spill-over and down-growth, we study the mechanical equilibrium of the section of the HRG process depicted in Figure 3.1: a crystal ribbon of length l and thickness t rests on top of the melt and is pulled out of the crucible at an angle β with respect to the melt surface. The use of an inert gas or cooling fluid flowing through a set of plates placed on top of the surface serve as a suitable means to dissipate the heat of crystallization flowing from the bath. The length of these plates determine the length of the ribbon inside of the molten bath, and the gas flow rate help control -along with the pulling rate- its thickness. It is assumed that the upper meniscus location (the point where the melt surface joins the ribbon) is determined by the melt height, the pulling angle by the length of the cooling plates (which gives rise to a fixed ribbon length).

As we mentioned before, a meniscus must be formed between the ribbon and the crucible so that no attachment of the ribbon to the crucible occurs. The meniscus

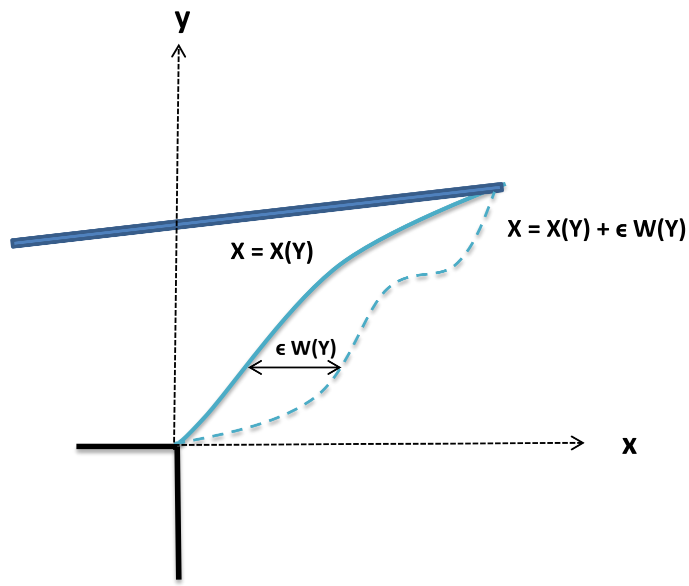

Figure 3.3: A variation is made to a stationary curve representing meniscus in the HRG process. Dashed line is the perturbed curve $X = X(Y) + \epsilon W(Y)$.

is assumed to be pinned at the outer corner of a crucible (that for now we assume to be rectangular). At this pinning point, the melt forms a contact angle θ with respect to the positive horizontal axis. The fact that the meniscus is hinged at a corner allows it to achieve a wide range of contact angles that might differ from the equilibrium angle θ_{eq}. The theoretical foundation of this phenomenon was developed by Gibbs [21] and is explained further in this work. Also, a growth angle σ is formed between the meniscus and the crystal; the observations of Surek and Chalmers [58] found that for a silicon system, the value is approximately $11°$. For our theoretical analysis, we neglect the effects of convection and the effects of thermal gradients. We also assume that the width of the ribbon is wide enough so that the meniscus is represented accurately in two dimensions.

3.4 The energy functional of the HRG process

In order to perform a variational treatment of the HRG process, we use the first law of thermodynamics to construct an expression for the total energy of the system. We have that the amount of energy required to add a melt slice of thickness dy (see Figure 3.1) into the system is

$$dU = \delta Q + dW_t, \tag{3.22}$$

where δQ is the incremental heat supplied to the system (which we assume to be zero), and dW_t is the total work done by the system on the melt slice. In our system the total work is that caused by the melt pressure on the volume differential, the increase in the surface area of the meniscus, and the change in the area of the melt in contact with the ribbon, thus

$$dU = -PdV + \gamma dA - (\gamma_{sv} - \gamma_{sl})dA'. \tag{3.23}$$

In the above equation P is the total pressure exerted over a slice of fluid of volume dV, γ is the liquid-vapor surface tension, dA is the change in the surface area of the meniscus, γ_{sv} is the solid-vapor interface tension, γ_{sl} the solid-liquid interfacial tension, and dA' the change in the surface area of the melt in contact with the ribbon. The overall pressure is given by the weight of the liquid plus the weight of the ribbon. In a two dimensional Cartesian coordinate system we have

$$P = \rho_l g(h_2 - y) + \rho_s g t, \tag{3.24}$$

and

$$dV = xdy. \tag{3.25}$$

Also, in a two dimensional Cartesian coordinate system we also have that

$$dA = ds = \sqrt{1 + \left(\frac{dx}{dy}\right)^2} dy, \tag{3.26}$$

where ds is an element of length along the meniscus profile. Similarly, we have that

$$dA' = ds' = \sqrt{1 + \left(\left.\frac{dx}{dy}\right|_{x=x_r}\right)^2} dy = \sqrt{1 + \cot^2(\sigma + \beta)}dy = \frac{dy}{\sin(\sigma + \beta)}. \tag{3.27}$$

Putting all these terms together, yields the following expression:

$$dU = -(\rho_l g(h_2 - y)) + \rho_s g t) x dy + \gamma \sqrt{1 + \left(\frac{dx}{dy}\right)^2} dy - \frac{(\gamma_{sv} - \gamma_{sl})}{\sin(\sigma + \beta)} dy. \tag{3.28}$$

Thus, the total change in energy of the HRG system is

$$\Delta U \left(y, x, \frac{dx}{dy}\right) = \int_0^{h_1} \left[-(\rho_l g(h_2 - y)) + \rho_s g t) x + \gamma \sqrt{1 + \left(\frac{dx}{dy}\right)^2} - \gamma \cot(\sigma + \beta) \right] dy. \tag{3.29}$$

In the last term of the integral we used Young's relationship:

$$\gamma_{sv} - \gamma_{sl} = \gamma \cos(\sigma + \beta). \tag{3.30}$$

Nondimensionalizing length scales with respect to the capillary constant,

$$a = \sqrt{\frac{\gamma}{\rho_l g}}, \tag{3.31}$$

yields the following expression

$$U_0 \left(Y, X, \frac{dX}{dY}\right) = \int_0^{H_1} \left[-\left(H_2 - Y + \frac{\rho_s}{\rho_l} T\right) X + \sqrt{1 + \left(\frac{dX}{dY}\right)^2} - \cot(\sigma + \beta) \right] dY, \tag{3.32}$$

where

$$U_0 = \Delta U \gamma^{-\frac{3}{2}} (\rho_l g)^{\frac{1}{2}},\ x = aX,\ y = aY,\ t = aT,\ h_1 = aH_1 \text{ and } h_2 = aH_2. \tag{3.33}$$

We see that the form of the energy functional of the HRG process allows us to use the classic variational concepts.

3.5 Existence of the meniscus in the HRG process

We find the stationary curves of our system by solving the Euler-Lagrange equation [20]:

$$\frac{\partial F}{\partial X} - \frac{d}{dY}\left(\frac{\partial F}{\partial X'}\right) = 0. \tag{3.34}$$

In our case we have,

$$F = -(H_2 - Y + \frac{\rho_s}{\rho_l}T)X + \sqrt{1 + \left(\frac{dX}{dY}\right)^2} - \cot(\sigma + \beta), \quad (3.35)$$

$$\frac{\partial F}{\partial X} = -(H_2 - Y + \frac{\rho_s}{\rho_l}T), \quad (3.36)$$

$$\frac{\partial F}{\partial X'} = \frac{\frac{dX}{dY}}{\sqrt{1 + \left(\frac{dX}{dY}\right)^2}}, \quad (3.37)$$

$$\frac{d}{dY}\left(\frac{\partial F}{\partial X'}\right) = \frac{\frac{d^2X}{dY^2}}{\left(1 + \left(\frac{dX}{dY}\right)^2\right)^{3/2}}, \quad (3.38)$$

so the resulting Euler-Lagrange equation is

$$-(H_1 - L\sin\beta - Y + \frac{\rho_s}{\rho_l}T) - \frac{\frac{d^2X}{dY^2}}{\left(1 + \left(\frac{dX}{dY}\right)^2\right)^{3/2}} = 0. \quad (3.39)$$

In the equation above we used the geometrical relationship

$$H_2 = H_1 - L\sin\beta, \quad (3.40)$$

where L is the dimensionless ribbon length.

We see that the first variation of the energy function, yields the governing Young-Laplace equation for the HRG process. The Young-Laplace equation is a second order differential equation and requires two boundary conditions to close its formulation. We set the pinning condition and the contact angle condition

$$X = X_c \text{ when } Y = 0, \quad (3.41)$$

$$\frac{dX}{dY} = \cot\theta \text{ when } Y = 0. \quad (3.42)$$

In equation (3.39) the value of the equilibrium height H_1 is unknown. Nonetheless, we know that at this point the following condition must hold

$$\frac{dX}{dY} = \cot(\sigma + \beta) \text{ when } Y = H_1. \quad (3.43)$$

This last additional expression is used to find the value of H_1. This approach is different from the one taken by Rhodes and collaborators (see Section 3.8). In their work they integrate numerically the Young-Laplace equation up to the point at which condition (3.43) is satisfied; this point corresponds to the value of the meniscus height but there is no previous knowledge if this value is attainable or not. In the next section we find an explicit expression of the equilibrium height, and use the calculated expression for solving the Young-Laplace equation.

3.5.1 The equilibrium height of the meniscus

Using $\frac{dX}{dY} = \cot\Omega$, we transform equation (3.39) into

$$(-H_1 + L\sin\beta + Y - \frac{\rho_s}{\rho_l}T)dY = -\sin\Omega d\Omega. \tag{3.44}$$

In this equation Ω is the angle formed between the tangent line to the meniscus at any point (X, Y) and the horizontal (see Figure 3.1). Integrating the left hand side from 0 to H_1, the right hand side from θ to $\sigma+\beta$, and solving for H_1, we obtain

$$H_{1\pm} = L\sin\beta - \frac{\rho_s}{\rho_l}T \pm \sqrt{\left(\frac{\rho_s}{\rho_l}T - L\sin\beta\right)^2 + 2\cos\theta - 2\cos(\sigma+\beta)} = H_{11} \pm H_{12}. \tag{3.45}$$

The existence of a real value of the equilibrium height H_1 is a necessary condition for the existence of the meniscus. Thus we require that

$$\frac{1}{2}\left(\frac{\rho_s}{\rho_l}T - L\sin\beta\right)^2 \geq \cos(\sigma+\beta) - \cos\theta. \tag{3.46}$$

In addition, we also require the equilibrium height to be always positive, i.e.

$$H_{11} \pm H_{12} > 0. \tag{3.47}$$

3.5.2 Shape and existence of the meniscus

Integrating equation (3.44) from the lower limits ($Y = 0$ and $\Omega = \theta$) to an arbitrary set of values Y and Ω, we solve for the angle Ω in terms of Y,

$$\Omega(Y) = \arccos\left(\frac{Y^2}{2} \mp H_{12}Y + \cos\theta\right). \tag{3.48}$$

Putting this expression into $\frac{dX}{dY} = \cot\Omega$ yields the following differential equation:

$$\frac{dX}{dY} = \cot\left(\arccos\left(\frac{Y^2}{2} \mp H_{12}Y + \cos\theta\right)\right) = \frac{\frac{Y^2}{2} \mp H_{12}Y + \cos\theta}{\sqrt{1 - \left(\frac{Y^2}{2} \mp H_{12}Y + \cos\theta\right)^2}}, \tag{3.49}$$

with initial condition

$$X = X_c \text{ when } Y = 0. \tag{3.50}$$

The solution to this equation is

$$X(Y) = X_c + \sqrt{A+2}[\mathbf{E}(\Psi_Y, \kappa) - \mathbf{E}(\Psi_0, \kappa)] - \frac{2}{\sqrt{A+2}}[\mathbf{F}(\Psi_Y, \kappa) - \mathbf{F}(\Psi_0, \kappa)], \tag{3.51}$$

where $\mathbf{F}(\Theta, \kappa)$ and $\mathbf{E}(\Theta, \kappa)$ are the incomplete elliptic integrals of the first and second kind respectively and,

$$\Psi_Y = \arcsin\left(\frac{Y \mp \sqrt{2\cos\theta - A}}{\sqrt{2-A}}\right), \tag{3.52}$$

$$\Psi_0 = \arcsin\left(\mp\sqrt{\frac{2\cos\theta - A}{2-A}}\right), \tag{3.53}$$

$$A = 2\cos(\sigma+\beta) - \left(\frac{\rho_s}{\rho_l}T - L\sin\beta\right)^2, \tag{3.54}$$

$$\kappa = \sqrt{\frac{A-2}{A+2}}. \tag{3.55}$$

The complete solution method is shown in Appendix A. The form of this solution is akin to the results found in the literature of capillarity phenomena and shaped crystal growth (see Laplace [35], Tatarchenko [60], Myshkis [42] and Anderson [1]). Also, single-valuedness of the solution is presupposed. The plus and minus signs in the equation indicate that the solution is composed by two branches. We analyze their existence using the argument of the inverse cosine in equation (3.48):

$$f(Y)_{\mp} = \frac{Y^2}{2} \mp H_{12}Y + \cos\theta. \tag{3.56}$$

This function must be continuous and must satisy the following condition:

$$-1 < f(Y)_{\mp} < 1 \quad \forall \quad Y \in [0, H_{1\pm}]. \tag{3.57}$$

Note that the use of a minus sign in f corresponds to the use of a positive sign in the expression for the equilibrium height shown in equation (3.45), and viceversa when the plus sign is used. In order to have a feasible meniscus, conditions (3.47) and (3.46) must satisfied as well as the following conditions (see Appendix B):

- The branch $f(Y)_+$ exists if:

$$\theta > \sigma + \beta \;\; \wedge \;\; \beta > \arcsin\left(\frac{\rho_s T}{\rho_l L}\right). \tag{3.58}$$

- The branch $f(Y)_-$ exists if:

$$1 + \cos(\sigma + \beta) \geq \frac{1}{2}\left(\frac{\rho_s}{\rho_l}T - L\sin\beta\right)^2, \tag{3.59}$$

$$[\theta < \sigma + \beta] \wedge \left[\theta > \sigma + \beta \;\; \wedge \;\; \beta > \arcsin\left(\frac{\rho_s T}{\rho_l L}\right)\right]. \tag{3.60}$$

- Both solution branches $f(Y)$ exist if:

$$1 + \cos(\sigma + \beta) \geq \frac{1}{2}\left(\frac{\rho_s}{\rho_l}T - L\sin\beta\right)^2, \tag{3.61}$$

$$\theta > \sigma + \beta \;\; \wedge \;\; \beta > \arcsin\left(\frac{\rho_s T}{\rho_l L}\right). \tag{3.62}$$

3.6 Stability of the meniscus in the HRG process

To guarantee that the stationary curve $X(Y)$ is stable, the Legendre test must be satisfied and the nontrivial solution to the governing Jacobi's differential equation must have no conjugate points. The (strengthened) Legendre conditions for a minimum requires that the condition,

$$\frac{\partial}{\partial X'}\left(\frac{\partial F}{\partial X'}\right) > 0, \tag{3.63}$$

must be satisfied at every point of the stationary curve. In our case we have that,

$$\frac{\partial}{\partial X'}\left(\frac{\partial F}{\partial X'}\right) = \frac{1}{\left(1 + (\frac{dX}{dY})^2\right)^{3/2}}, \tag{3.64}$$

which is always positive at every point of the admissible stationary curve described by equation (3.51) and its existence conditions. Thus, Legendre test is satisfied.

The Jacobi differential equation

$$\left[\frac{\partial^2 F}{\partial X^2} - \frac{d}{dY}\left(\frac{\partial^2 F}{\partial X \partial X'}\right)\right] V - \frac{d}{dY}\left(\frac{\partial^2 F}{\partial X'^2}\frac{dV}{dY}\right) = 0, \tag{3.65}$$

with conditions

$$V(0) = 0 \quad \text{and} \quad \left.\frac{dV}{dY}\right|_{Y=0} = 1, \tag{3.66}$$

applied to our case yields

$$\frac{\partial^2 F}{\partial X^2} = 0, \tag{3.67}$$

$$\frac{\partial}{\partial X}\left(\frac{\partial F}{\partial X'}\right) = \frac{\partial}{\partial X}\left(\frac{\frac{dX}{dY}}{\sqrt{1+\left(\frac{dX}{dY}\right)^2}}\right) = 0, \tag{3.68}$$

$$\frac{\partial}{\partial X'}\left(\frac{\partial F}{\partial X'}\right) = \frac{\partial}{\partial X'}\left(\frac{\frac{dX}{dY}}{\sqrt{1+\left(\frac{dX}{dY}\right)^2}}\right) = \frac{1}{\left(1+\left(\frac{dX}{dY}\right)^2\right)^{3/2}}. \tag{3.69}$$

So our Jacobi differential equation reduces to

$$-\frac{d}{dY}\left(\frac{\partial^2 F}{\partial X'^2}\frac{dV}{dY}\right) = 0. \tag{3.70}$$

Integrating once we have

$$\frac{\partial^2 F}{\partial X'^2} V' = K_1. \tag{3.71}$$

Imposing $V'(0) = 1$, and knowing that at the origin $X' = \cot\theta$ we get

$$\frac{1}{(1+\cot^2\theta)^{3/2}} \cdot 1 = \sin^3\theta = K_1. \tag{3.72}$$

Updating our differential equation, we have

$$\frac{dV}{dY} = \sin^3\theta \left(1 + \left(\frac{dX}{dY}\right)^2\right)^{3/2}. \tag{3.73}$$

Imposing the remaining boundary condition gives,

$$\begin{aligned} V(Y) &= V(0) + \sin^3\theta \int_0^Y \left(1 + \left(\frac{dX(\overline{Y})}{d\overline{Y}}\right)^2\right)^{3/2} d\overline{Y} \\ &= \sin^3\theta \int_0^Y \left(1 + \left(\frac{dX(\overline{Y})}{d\overline{Y}}\right)^2\right)^{3/2} d\overline{Y}. \end{aligned} \tag{3.74}$$

The above function does not vanish for any value of $Y \in (0, H_1)$ and values of $\theta \in (0°, 180°)$. Thus, the solution $V(Y)$ has no conjugate points, and the stationary curves described by equation (3.51) are a minimum and stable with respect to weak perturbations. The values $\theta = 0°$ and $\theta = 180°$ represent stability limits, but as we show in the next section, these angles are never realized due to the pinning conditions found by Gibbs.

3.6.1 Analyzing the pinning condition via the Gibbs's limit

So far we have worked under the assumption that the meniscus remains hinged at the corner of the crucible. However, this assumption is only valid for a given range of contact angles. In his work on thermodynamics, Gibbs [21] found the range of contact angles under which the surface of a liquid placed at the corner of a solid surface remains at equilibrium (see Figure 3.4). These criteria allows us to know the contact angles at which the meniscus either recedes or spills over from the corner of the crucible. The classical representation of the limits is (see Appendix E):

$$\theta_{eq} < \theta_g < 180° - \phi + \theta_{eq}. \tag{3.75}$$

The angle θ_g in this expression is the *supplement* of the angle θ that we employ throughout this work, ϕ is the angle of the corner of the two solid surfaces (90° for a rectangular crucible) and θ_{eq} is the equilibrium wetting angle. Angles below the lower limit forces the meniscus backwards into the crucible and those above the upper limit induces the melt to spill over.

3.7 Illustration of the theory

In order to illustrate the applicability of our theory, we present an analysis using the properties and parameters for a silicon system. All the equations and results presented above are dimensionalized using the values in Table 3.1. The values of the wetting angles were taken from the observations by Swartz et al. [59], Surek

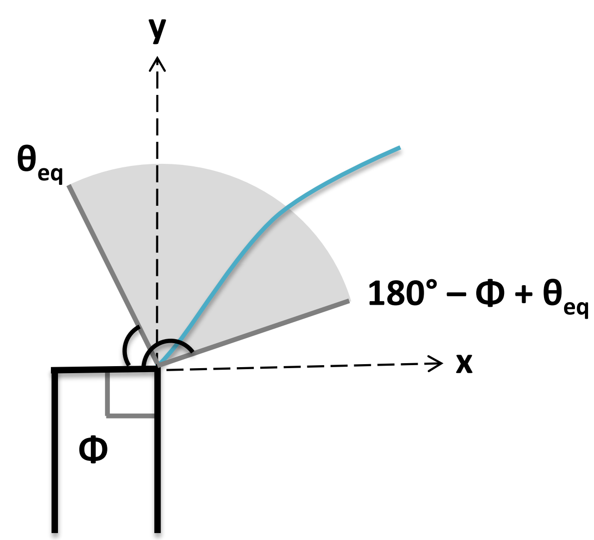

Figure 3.4: The contact angle θ must be between the Gibbs' limits to ensure its pinning to the corner of the crucible. The values of θ must lie within the shaded region (see equation (3.75)).

et al. [57] and Champion et al. [11]. The wetting angles are measured from the liquid-solid interface to the liquid-vapor interface, as shown in Figure 3.5. With these values, we develop a straightforward methodology to find the hydrostatically feasible configuration for producing a silicon ribbon of 6 centimeters in length and 400 micrometers in thickness. The decision variables are the pulling angle β and the type and shape of crucible to use (which determines the range of possible contact angles θ).

3.7.1 The existence of the meniscus in terms of θ and β

The conditions of existence found in Section 3.5.2 allows us to know all the possible hydrostatically feasible configurations that satisfy the boundary conditions for a given set of operating parameters (wafer thickness, wafer length and pulling angle). From a process design perspective, the ribbon length and thickness can be considered degrees of freedom, so we can exert controllable actions on them: the length of the

Parameter	Symbol	Value
Density of solid silicon	ρ_s	2293 $[kg\ m^{-3}]$
Density of liquid silicon	ρ_l	2570 $[kg\ m^{-3}]$
Acceleration of gravity	g	9.8 $[m\ s^{-2}]$
Surface tension of silicon	γ	0.72 $[J\ m^{-2}]$
Silicon growth angle	σ	$11°$
Melt-graphite wetting angle	θ_{eq_c}	$30°$
Melt-quartz wetting angle	θ_{eq_s}	$87°$

Table 3.1: Material properties and parameters used in the illustrative example.

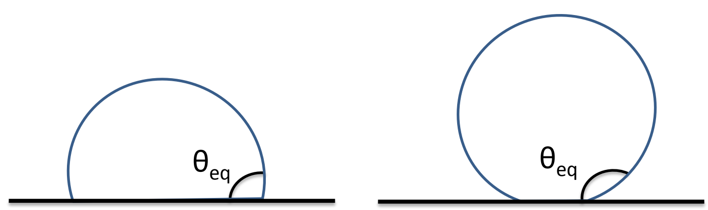

Figure 3.5: The contact angle for a wetting material (left) and a non-wetting material (right). A silicon melt in contact with a graphite crucible exhibits high wettability, whereas low wettability is observed in a silicon melt sitting on a quartz crucible. See Table 3.1.

Condition	Expression/Function
Existence	$\theta(\beta) = \arccos\left(\cos(\sigma+\beta) - \frac{1}{2}\left(\frac{\rho_s}{\rho_l}T - L\sin(\beta)\right)^2\right)$
$f_\pm$ to f_- boundary	$\theta(\beta) = \sigma + \beta$
$f_\pm$ to f_+ boundary	$0 = \frac{1}{2}\left(\frac{\rho_s}{\rho_l}T - L\sin(\beta)\right)^2 - 1 - \cos(\sigma+\beta)$
β_{crit}	$\beta = \arcsin\left(\frac{\rho_s T}{\rho_l L}\right)$
Spill-over	$\theta = \phi - \theta_{eq}$
Receding meniscus	$\theta = 180° - \theta_{eq}$

Table 3.2: Functions constraining the area of static stability for molten silicon on a graphite crucible. The value of β in the equation describing the $f_\pm$ to f_+ boundary is calculated numerically.

wafer can be controlled by setting the length of the cooling plates placed on top of the melt. And the thickness of the ribbon can be controlled by adjusting the cooling rate and the pulling speed of the ribbon. With these values under control, we are left with an additional degree of freedom, the pulling angle, and a process variable that depends primarily on the wetting properties of the interacting materials, the contact angle. Although this last variable cannot be controlled while the system is in operation, we address this issue by finding feasible configurations that, given a pulling angle, allow for the existence of a wide range of contact angles. Once we find this range, we show its correlation with the range of permissible melt levels.

Figure 3.6 and Figure 3.7 show the regions of existence for a HRG system corresponding to the production of a silicon ribbon of 6 centimeters in length and 400 microns in thickness. We assume that the crucible is made of graphite and that we have two possible crucible edge geometries: one with a rectangular corner ($\phi = 90°$) and one with a relatively sharp corner ($\phi = 45°$). The solid curves representing the conditions found in Section 3.5.2 divide the $\beta - \theta$ space into six operating zones, three of which give rise to hydrostatically feasible configurations (where the solution branches $f_{\pm}, f_{-}$ or f_{+} exist). The dashed lines representing the Gibbs' limits for both the rectangular and sharp-cornered crucible constrain further the feasible values of the contact angle θ. The uppermost horizontal line is the value of the contact angle where the meniscus recedes from the corner and displaces towards the inner surface of the crucible. The other horizontal lines are the values of the contact angle where the meniscus unpins from the corner of crucible and the melt spills over. We see that the use of a sharp-edged crucible is preferable over a rectangular-edged one.

Within the three regions where we have feasible configurations, we find that there exists values of pulling angles that further enhances the flexibility of the operation. We mentioned earlier that the contact angle is a variable that cannot be controlled in the system, and that, what we would like to find is a set of pulling angles that correspond to the existence of a wide range of contact angles. For example, when the ribbon is pulled at an angle of $10°$ and the meniscus is pinned to a sharp-edged corner, the hydrostatically feasible configuration corresponding to the solution branch f_{-} exist for values of θ ranging from $15°$ (the spill-over limit) to $146.8°$ (the existence limit); for the case of the solution branch f_{+} it exists from a value of $21°$ (the $f_{\pm}$ to f_{-} boundary) to $146.8°$ (the existence limit). By pulling the ribbon at $10°$, the range of possible contact angles for both solution branches is relatively wide, which implies a more flexible operating condition. Contrasting this with pulling the ribbon at $5°$, we have that in order to obtain a feasible configuration, the contact angle is constrained from below by values between $15°$ and approximately $56.9°$ for both solution branches. The case worsens if one uses relatively large pulling angles (e.g. $12°$, as only one solution branch exists). Also pulling the ribbon completely horizontal is an inflexible operating condition, both from the point of view of hydrostatics (the window of operability in terms of θ is very small) and thermodynamics (the feasible contact angle corresponding to a zero pulling angle are below the Gibbs' limits).

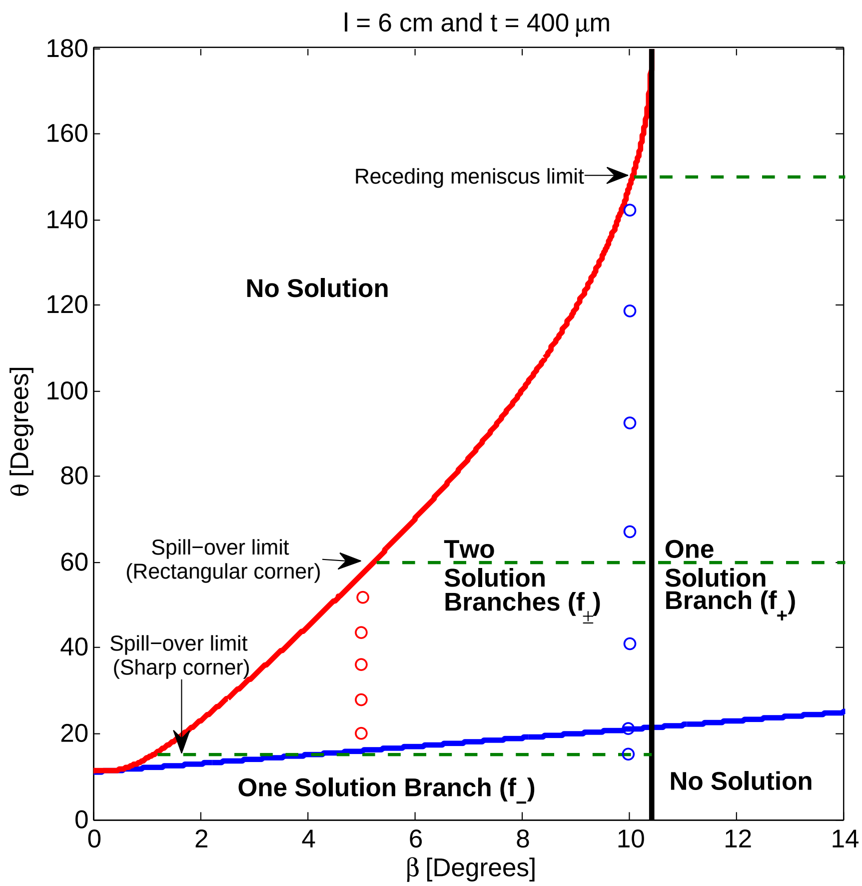

Figure 3.6: Regions of meniscus existence for a 6 centimeter long and 400 microns thick ribbon. Solid lines are the existence conditions found in Section 3.5.2. The dashed lines represent the Gibbs' limits. Meniscii shown in Section 3.7.3 correspond to the circles in the existence diagram.

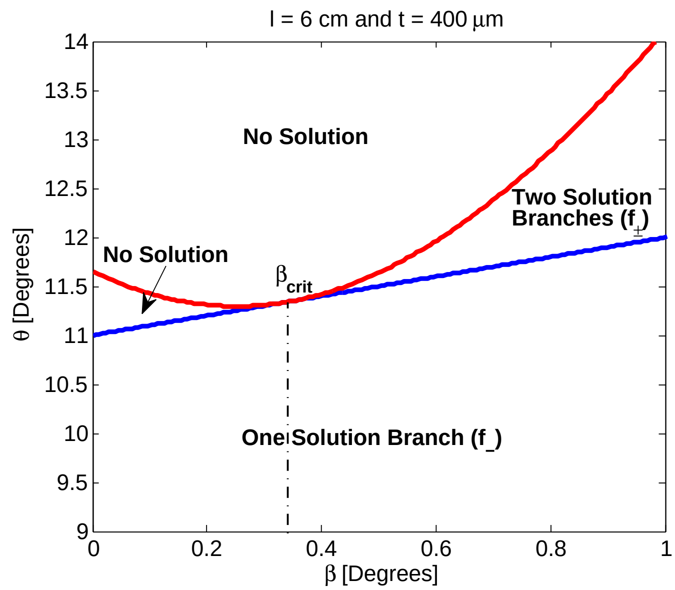

Figure 3.7: Expanded view of existence region close to the origin.

Another aspect to mention, not shown in the figure, is the difference in the Gibbs' limits between the graphite crucible and a silica crucible. In the figure we show that for a rectangular-cornered graphite crucible, the Gibbs' limits are between $\theta = 60°$ and $\theta = 150°$, and that the lower limit can be reduced to $\theta = 15°$ by using of a sharp-edged crucible. In the case of silica, the limits for a rectangular-cornered crucible are between $\theta = 3°$ and $\theta = 93°$. The value of the lower limit implies that there is very little difference in using a sharp-edged silica crucible, since the lower limit could be reduced by at most three degrees. This means that the large enhancement of the pinning condition that is achieved by using a sharp-edged crucible cannot be obtained in silica crucibles.

3.7.2 The equilibrium height of the meniscus and its relationship with the melt height

In the previous section, we showed that there are pulling angles that ensure the existence of the meniscus for a wide range of contact angles. In Figure 3.8 we plot

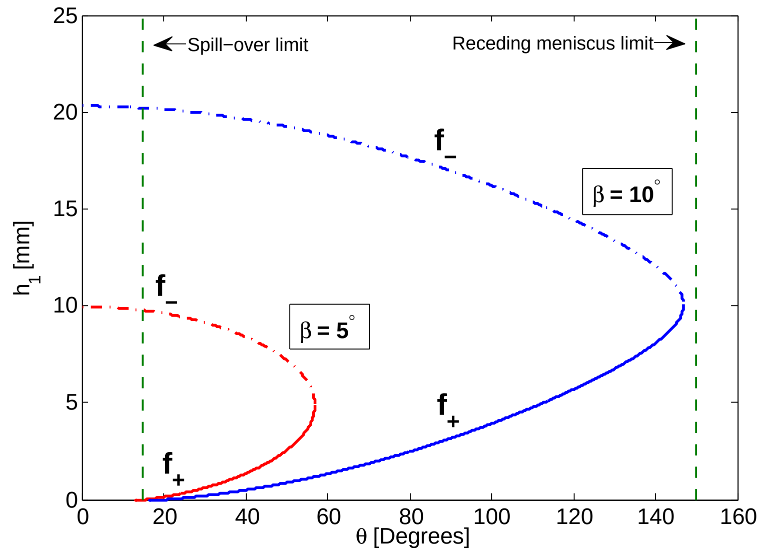

Figure 3.8: Equilibrium height as a function of the contact angle for two different pulling angles. The realization of a wider range of contact angles can be achieved by using large values of β.

the equilibrium height as a function of the contact angle, for the cases when $\beta = 5°$ and $\beta = 10°$. We see clearly that a wider range of possible meniscii are achievable when a pulling the ribbon at $10°$ than at $5°$. The "trajectory" of the solution corresponding to $\beta = 10°$ encompasses a wider range of feasible meniscii. We also see the behaviour of the two solution branches, f_- and f_+, each corresponding to the dashed and solid line respectively. The equilibrium height for the solution branches have the opposite trend as the contact angle increases: for the case of f_- it decreases monotonically and for the case of f_+ it increases monotonically. Both solution branches have the same equilibrium height at the vertex of the parabola, where they reach the existence limit described by equation (3.46) with the equality enforced. Since the meniscus height is related to the melt height by $h_2 = h_1 - l \sin \beta$, the behaviour of the solution also means that as the melt level increases from a lower bound to a critical point (the value of h_2 at the vertex) the contact angle increases; once it crosses this point, as the melt level keeps increasing, the contact angle will decrease until it reaches the spill-over limit. The vertex of the parabola represents the point where the combined pressure of the ribbon and the melt acting upon the meniscus is equal to zero (i.e. $\rho_s g t + \rho_l g h_2 = 0$), so that the overall pressure across the meniscus $\Delta P(y)$ is always less than or equal to zero at this point. As the melt level increases, the exerted pressure across a section of the meniscus can be positive in one section and negative in another section. This change in pressure induces the formation of meniscii with convexo-concave shapes.

The solution branch f_- exists for values of θ ranging from $0°$ to $146.8°$, but is constrained by the spill-over condition at $\theta = 15°$. The case for f_+ is different, for its existence is constrained by the condition $\theta > \sigma + \beta$, represented by the diagonal line in the existence diagram. For $\beta = 5°$, $\theta_{min} = 16°$, and for $\beta = 10°$, $\theta_{min} = 21°$. At these contact angles, the equilibrium height of the configuration corresponding to the solution branch f_+ is zero and the ribbon is at risk of freezing to the crucible. The union of these two solution branches with their imposed constraints represent the overall solution of the hydrostatic problem of the HRG process.

Finally, we correlate the existence of the meniscus heights to their corresponding melt levels. From Figure 3.9 we see that pulling a 6 centimeter long, 400 microns thick ribbon at 10 degrees is a feasible configuration if the surface of the silicon melt is kept at around 1 centimeter above or below the crucible lip. Values outside this range provoke the freezing of the ribbon to the crucible or the melt spilling over from it. For the case when the ribbon is pulled at 5 degrees, these limits narrow to approximately ± 0.5 centimeters. This result offers useful insights as it points directly into a variable that can and must be measured and controlled while the process is in operation.

3.7.3 The shape of the meniscus and the hydrostatically feasible configurations

Having already calculated the relationship between the height of the meniscus and the height of the melt, we proceed to plot the shape of the meniscii for both solution

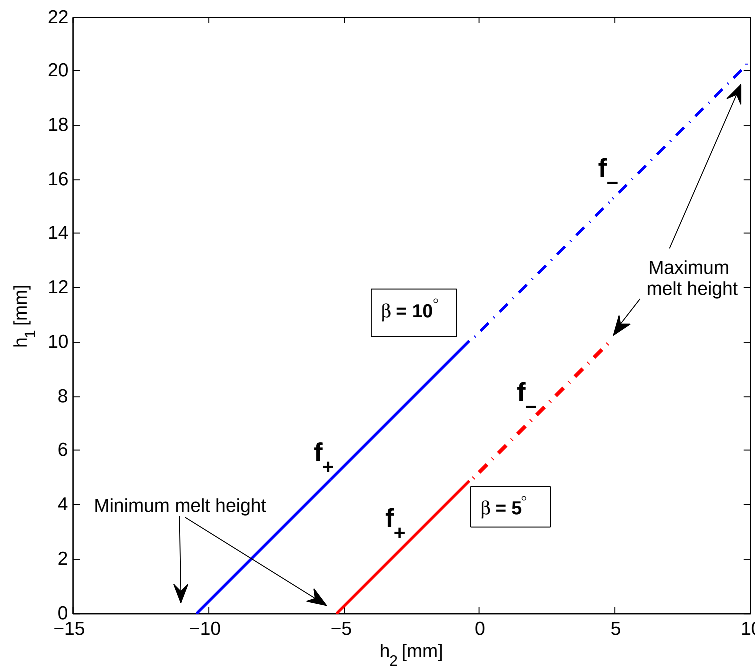

Figure 3.9: Meniscus height as a function of the melt height.

branches. In Figure 3.10 we plot several meniscii that correspond to the solution branch f_+. From Figure 3.9 we see that this branch gives us the minimum melt level allowed in the system, which is equal to approximately 10.4 milimeters below the edge of the crucible. Starting from this point, as the melt level increases, the equilibrium height and the contact angle increase as well; the meniscus takes a concave shape, up to the critical value of approximately 0.35 milimeters below the crucible edge (corresponding to $\theta \approx 146°$). At this point the shape of the meniscus is described by the solution branch f_- shown in Figure 3.11; as the melt level increases, it starts exerting pressure over the meniscus, which explains the bulking of the meniscus close to its pinning point and the decrease in the value of the contact angle. This induces the formation of a meniscus with a convexo-concave shape. The concave portion of the meniscus corresponds to a negative pressure differential exerted over it, and the convex to a positive differential. This pressure differential is attributed more to the melt level than to the weight of the wafer. In this particular configuration, the contact angle starts decreasing as we increase the height of the melt, up to a value of approximately 9.79 milimeters (corresponding to $\theta = 15°$), where we reach the spill-over limit.

In Figures 3.12 and 3.13 we plot the different meniscus shapes when pulling the ribbon at 5 degrees for each solution branch. Pulling the ribbon at $\beta = 10°$ gives rise to meniscii with larger heights and permits the extraction of the ribbon at a wide range of melt levels. This is specially important if the static equilibrium is perturbed by a sudden increase or decrease of the melt level. This flexible configuration also gives rise to meniscii with surfaces closer to the inside of the crucible. Potentially unstable meniscii are flatter and more elongated towards the outside of the crucible, and a narrower range of melt heights guarantees hydrostatic equilibrium. Figures 3.14 and 3.15 illustrate two hydrostatically feasible configurations drawn to scale. In Figure 3.14 we sketch the configuration of an HRG system with the melt placed at a level slightly below the surface of the crucible lip, in Figure 3.15 we sketch a configuration with the surface of the melt at the maximum level; a higher pressure exerted over the meniscus will induce the meniscus to unpin from the corner of the crucible and cause the melt to spill over.

3.7.4 Stability analysis

In this section we illustrate the stability of the meniscii by plotting the dimensional form of the perturbation function, $v(y)$, as a function of y. In Section 3.6 we found that the Legendre test is satisfied and that the stationary curves correspond to a minimum; we also found that the solution of the Jacobi differential equation has no conjugate points, and therefore the meniscii described by our analytical solution are always stable. Figure 3.16 shows the solution of the Jacobi differential equation for the meniscii curves shown in Figure 3.11. These curves correspond to the integration of expression (3.73), which we solved using MATLAB's ode15s function.

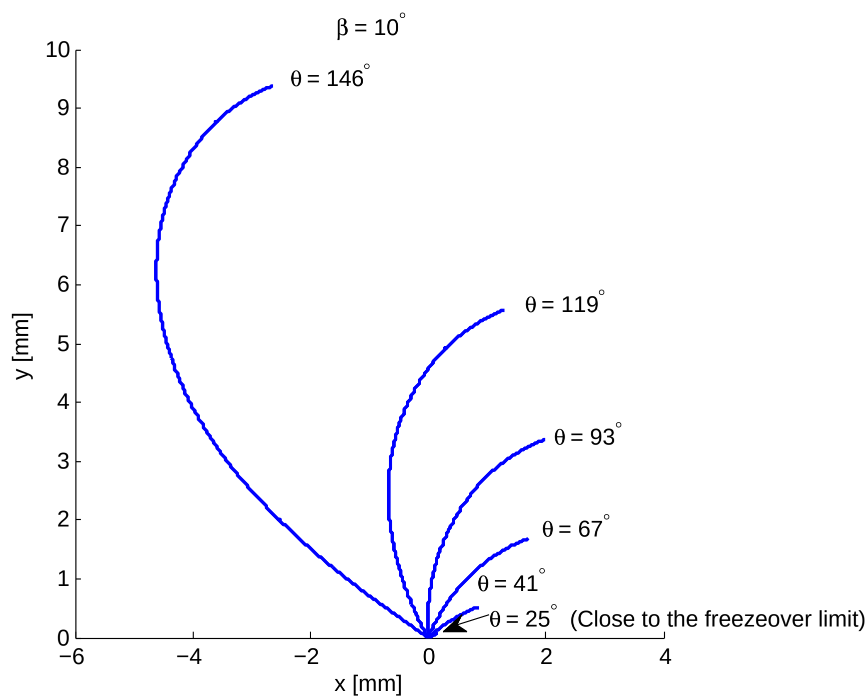

Figure 3.10: Plots of analytical solution (equation (3.51)) of the governing Young-Laplace equation for the HRG process. Plots show the shape of the meniscus for a 400 microns thick and 6 centimeters long ribbon and a pulling angle of $\beta = 10°$. Meniscii shapes correspond to the solution branch f_+.

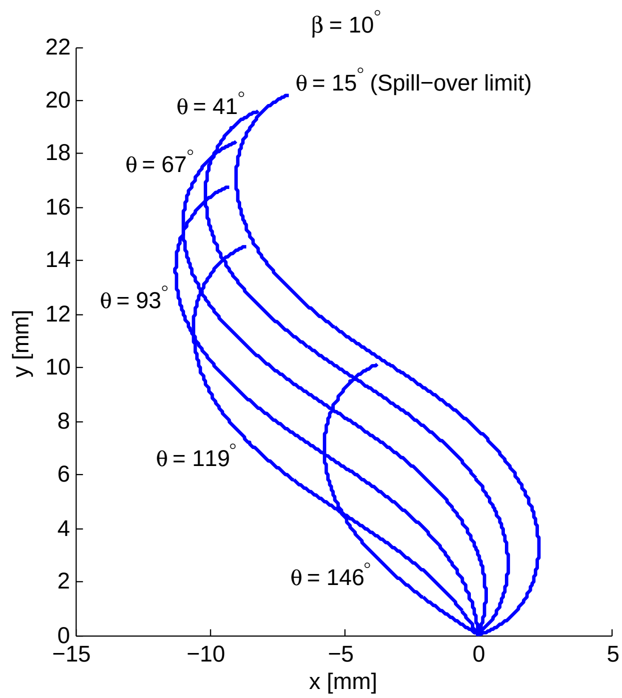

Figure 3.11: Plots of analytical solution (equation (3.51)) of the governing Young-Laplace equation for the HRG process. Plots show the shape of the meniscus for a 400 microns thick and 6 centimeters long ribbon and a pulling angle of $\beta = 10°$. Meniscii shapes correspond to the solution branch f_{-}.

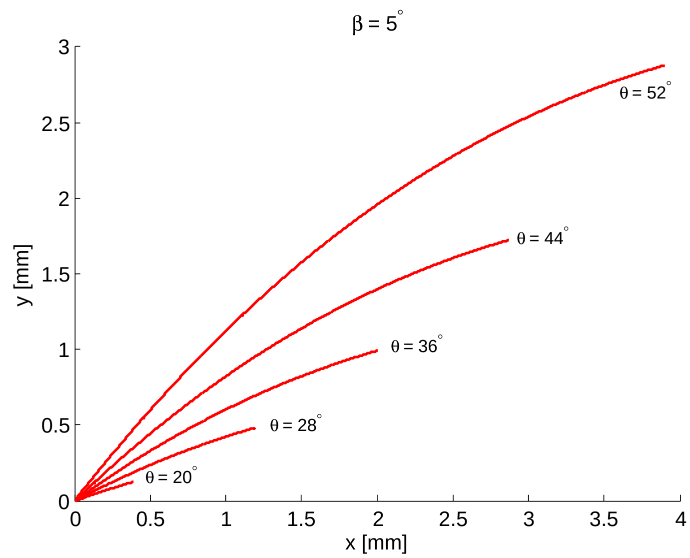

Figure 3.12: Plots of analytical solution (equation (3.51)) of the governing Young-Laplace equation for the HRG process. Plots show the shape of the meniscus for a 400 microns thick and 6 centimeters long ribbon and a pulling angle of $\beta = 5°$. Meniscii shapes correspond to the solution branch f_+.

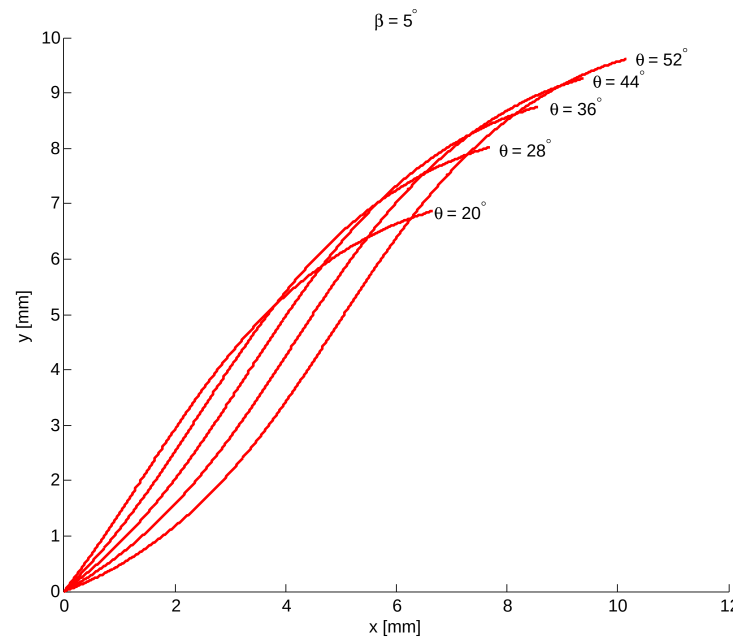

Figure 3.13: Plots of analytical solution (equation (3.51)) of the governing Young-Laplace equation for the HRG process. Plots show the shape of the meniscus for a 400 microns thick and 6 centimeters long ribbon and a pulling angle of $\beta = 5°$. Meniscii shapes correspond to the solution branch f_{-}.

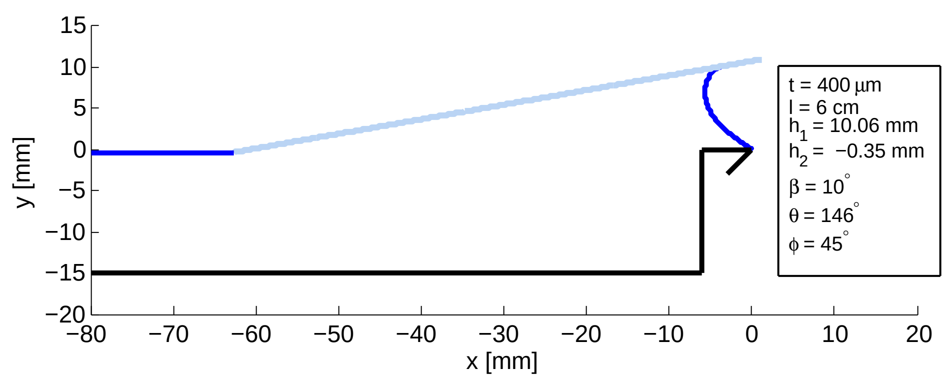

Figure 3.14: Schematic of hydrostatically feasible operation for producing a 6 centimeter long and 400 microns thick wafer.

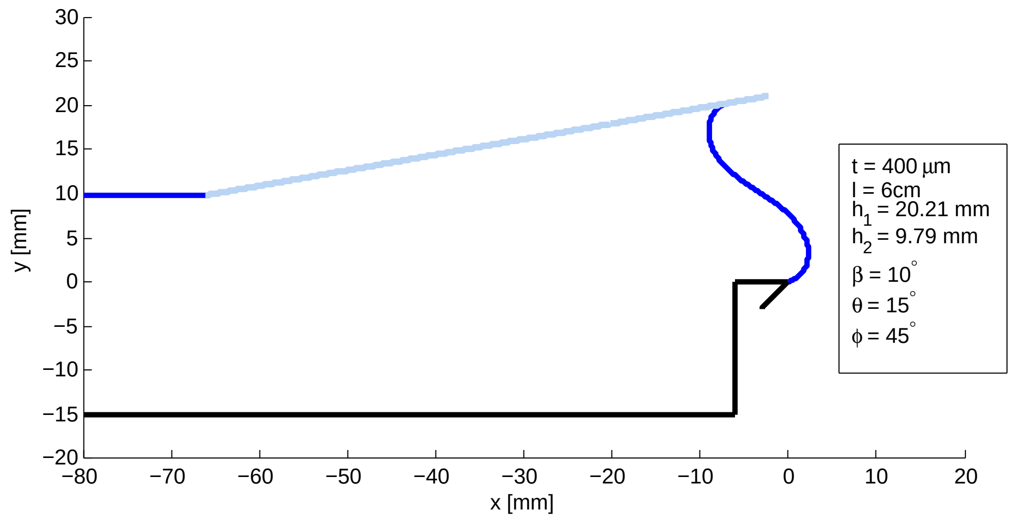

Figure 3.15: Schematic of hydrostatically feasible operation for producing a 6 centimeter long and 400 microns thick wafer. This configuration is prone to melt-spill over, as the contact angle θ is equal to the lower value of the Gibbs' limit.

3.8 Comparison of analytical solution with existing literature

In this section, we compare our theoretical findings with three works reported in the ribbon growth literature. The first is the computational work carried by Rhodes and co-workers [48] on the shape of the meniscus in the HRG process. The other two are computational calculations on the shape and equilibrium height of the meniscus in the EFG process. In both processes, the meniscus is described by the Young-Laplace equation that we derived in the main section. The only differences are the terms describing the value of the pressure differential, ΔP, sustained across the meniscus.

3.8.1 The analysis by Rhodes, Sarraf and Liu on the HRG Process (1980)

In order to validate our solution strategy, we compare our results with the computational work of Rhodes and coworkers [48]. In their investigation, *Meniscus stability*

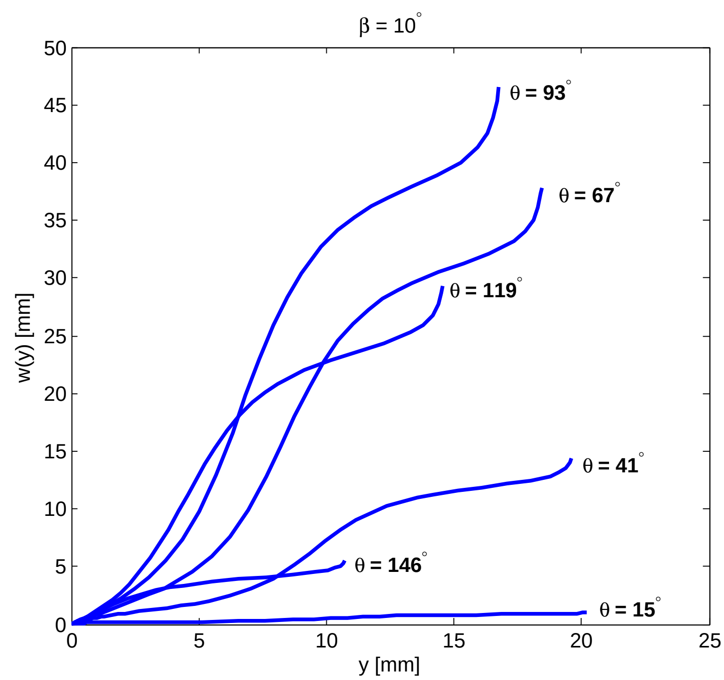

Figure 3.16: The solution of Jacobi's differential equation in dimensional form for the meniscii plotted in figure 3.11. The function $v(y)$ has no conjugate points in the interval $(0, H_1)$.

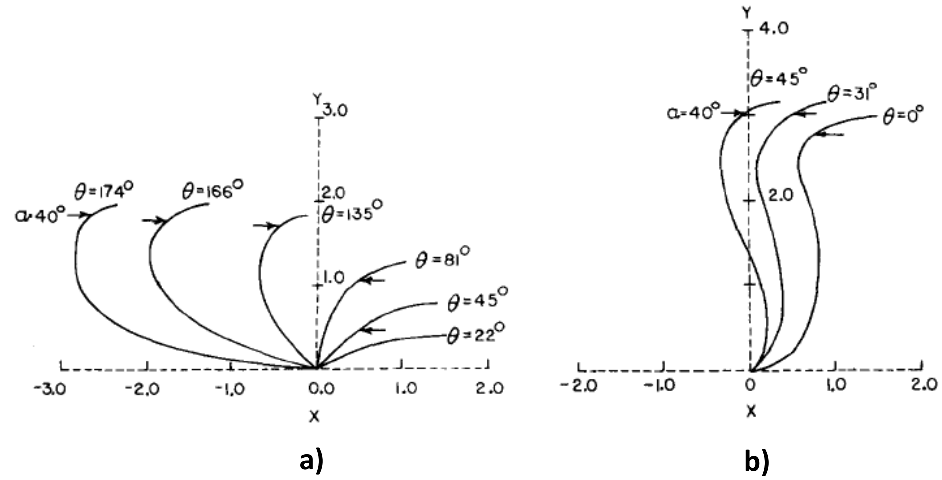

Figure 3.17: Meniscus shapes for different contact angles and melt levels calculated by Rhodes and collaborators. a) Meniscus shapes for $H_2 = 0$, b) Meniscus shapes for $H_2 = 1.5$. Figures are extracted from the original research paper (see reference [48]).

in horizontal ribbon growth, they perform a capillary analysis of the lower meniscus of the HRG process. Using the Young-Laplace equation as the starting point and neglecting the weight of the wafer, they calculate numerically the shapes of several meniscii as a function of the melt height, H_2. The differential equation they solve is (equation (4) in their paper)

$$H_2 - Y = \frac{\frac{d^2Y}{dX^2}}{\left(1 + \left(\frac{dY}{dX}\right)^2\right)^{3/2}}, \tag{3.76}$$

with boundary conditions $Y = 0$ at $X = 0$ and $dY/dX = \tan(\theta)$ at $X = 0$. They solved the initial boundary value problem by integrating via finite differences up to the point where the condition $dY/dX = \tan(\sigma + \beta)$ is attained. This is the point where $Y = H_1$. With our solution strategy shown in Section 3.5.1, we find an a priori analytical expression for the equilibrium height,

$$H_1 = H_2 \pm \sqrt{H_2^2 + 2(\cos(\sigma + \beta) - \cos(\theta))}, \tag{3.77}$$

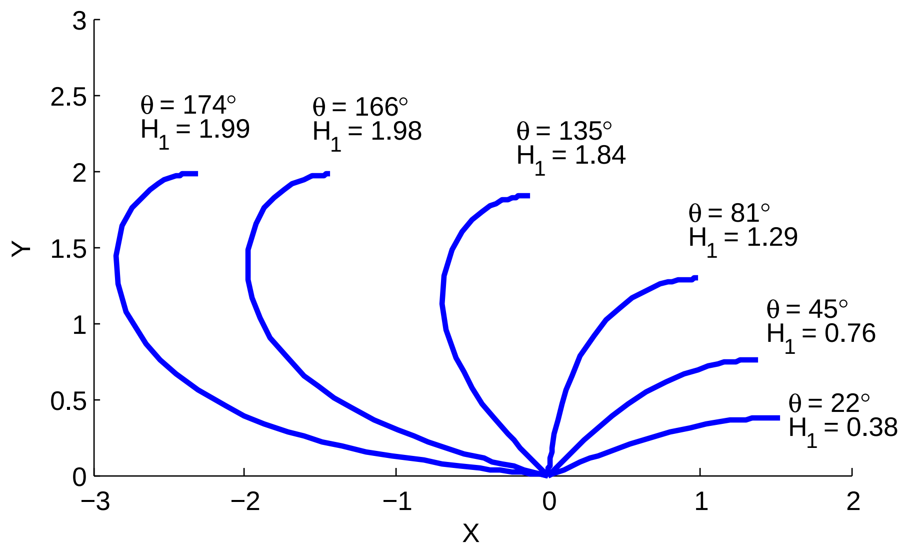

Figure 3.18: Meniscus shapes for $H_2 = 0$ calculated with equation (3.78). The meniscus shapes calculated analytically match the modeling results by Rhodes [48].

and the analytical expression describing the shape of the meniscus

$$X(Y) = \sqrt{2+A}\left[\mathbf{E}\left(\arcsin\left(\frac{Y-H_2}{\sqrt{2-A}}\right)\middle|\frac{A-2}{A+2}\right) - \mathbf{E}\left(\arcsin\left(\frac{-H_2}{\sqrt{2-A}}\right)\middle|\frac{A-2}{A+2}\right)\right]$$
$$-\frac{2}{\sqrt{A+2}}\left[\mathbf{F}\left(\arcsin\left(\frac{Y-H_2}{\sqrt{2-A}}\right)\middle|\frac{A-2}{A+2}\right) - \mathbf{F}\left(\arcsin\left(\frac{-H_2}{\sqrt{2-A}}\right)\middle|\frac{A-2}{A+2}\right)\right], \tag{3.78}$$

with

$$A = 2\cos(\theta) - H_2^2. \tag{3.79}$$

Figure 3.18 and 3.19 show plots of the analytical solution corresponding to the two cases studies by Rhodes and co-workers ($H_2 = 0$ and $H_2 = 1.5$). The values of equilibrium heights are determined by equation (3.77) using the positive sign. From this equation we see that if $H_2 = 0$, $\sigma = 0$ and $\beta = 0$, as $\theta \to \pi$, H_1 tends to the maximum equilibrium height, which is 2. Also, we see that if $H_2 = 1.5$, $\sigma = 0$ and $\beta = 0$, as $\theta \to 0$, H_1 tends to 3. It's worth noting that in the latter case, the meniscus shape corresponding to $\theta = 0°$ is the stability limit.

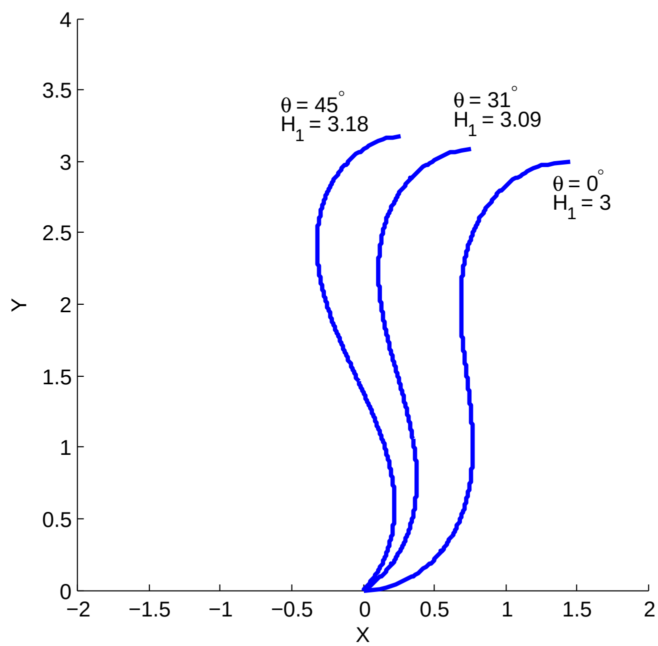

Figure 3.19: Meniscus shapes for $H_2 = 1.5$, calculated with equation (3.78). The meniscus shapes calculated analytically match the modeling results by Rhodes [48].

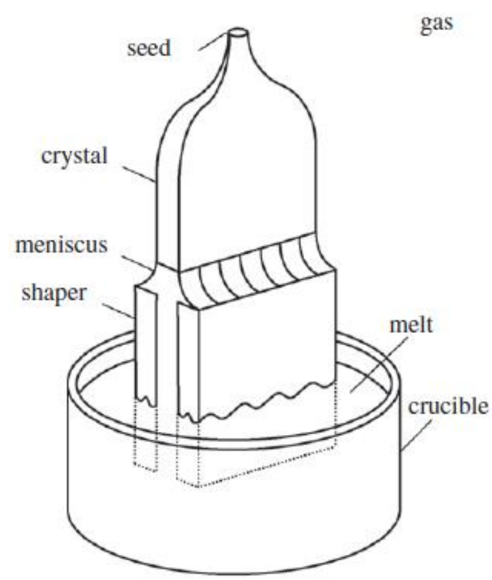

Figure 3.20: A sketch of the EFG process to grow silicon ribbons.

3.8.2 The analysis by Swartz, Surek and Chalmers on the EFG process (1974)

In one of the seminal works on the Edge-defined, film-fed growth process, *The EFG Process Applied to the Growth of Silicon Ribbons*, Swartz, Surek and Chalmers [59] perform a capillary analysis to calculate the shape of the meniscus as a function of an effective height h_{eff}. The meniscus existence and stability is critical in determining the thickness of the ribbon (see Figure 3.20). The formulation they use to calculate the shape of the meniscus of the ribbon *side* is the following (equations (2), (3) and (6) of their paper):

$$\rho g(h_{eff} - z) = \gamma \left(\frac{\frac{d^2x}{dz^2}}{\left(1 + \left(\frac{dx}{dz}\right)^2\right)^{3/2}} \right). \tag{3.80}$$

The boundary conditions are $x = t/2$ and $dx/dz = \tan\phi_0$ at z = 0. Here t is the thickness of the ribbon (0.04 cm), ϕ_0 is the growth angle (10°), γ the surface tension ($720\, erg/cm^2$) and ρ is the fluid density ($2.53\, g/cm^3$). The problem was integrated numerically, so we can use it to compare it with our theoretical solution. The explicit expression of the height of the meniscus is given by

$$h_{eq} = h_{eff} \pm \sqrt{h_{eff}^2 - \frac{2\gamma(\sin\alpha - \sin\phi_0)}{\rho g}}. \tag{3.81}$$

In this equation, α is the angle attained at the lower part of the meniscus. The limiting meniscus height mentioned in the original research paper is calculated by setting this value to 90°. The analytical solution for this problem in dimensionless form is

$$\begin{aligned} X(Z) = {} & \frac{T_r}{2} + \\ & \sqrt{2+A}\left[\mathbf{E}\left(\arcsin\left(\frac{Z-H_{eff}}{\sqrt{2-A}}\right)\middle|\frac{A-2}{A+2}\right) - \mathbf{E}\left(\arcsin\left(\frac{-H_{eff}}{\sqrt{2-A}}\right)\middle|\frac{A-2}{A+2}\right)\right] \\ & - \frac{2}{\sqrt{A+2}}\left[\mathbf{F}\left(\arcsin\left(\frac{Z-H_{eff}}{\sqrt{2-A}}\right)\middle|\frac{A-2}{A+2}\right) - \mathbf{F}\left(\arcsin\left(\frac{-H_{eff}}{\sqrt{2-A}}\right)\middle|\frac{A-2}{A+2}\right)\right], \end{aligned} \tag{3.82}$$

with,

$$A = -2\sin(\phi_0) - H_{eff}^2, \tag{3.83}$$

and

$$x = aX,\; z = aZ,\; t_r = aT_r,\; h_{eff} = aH_{eff}, \tag{3.84}$$

where a is the capillary constant.

Figure 3.21 shows the the original meniscus shapes calculated numerically by Surek an co-workers and the meniscus shapes calculated with the analytical expression given by equation (3.82). We show that with our solution strategy it is possible to calculate the shapes of the meniscii, as well as the limiting meniscus heights.

3.8.3 The analysis of Balint and Balint on the EFG process (2008)

We finalize the validation of our analytical work by comparing a recent result on the EFG process, which concerns the dependency of the equilibrium height of the

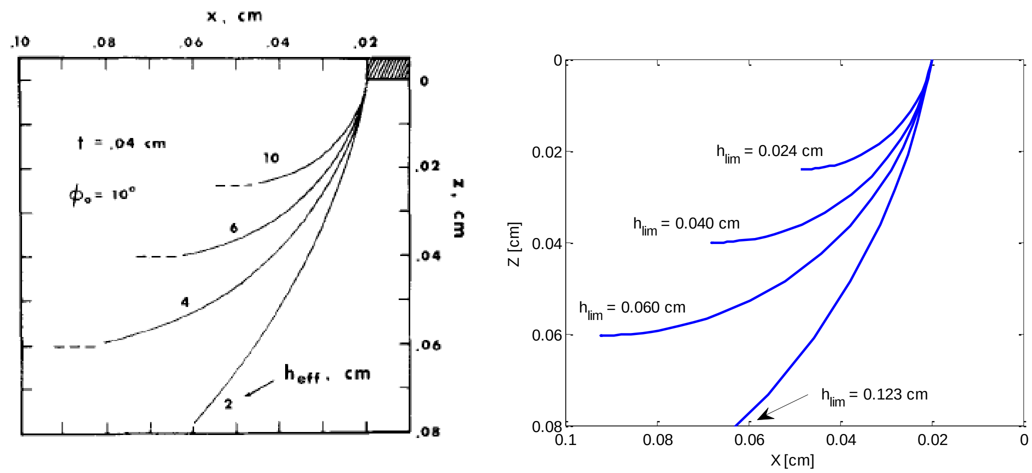

Figure 3.21: Meniscus shapes calculated by Swartz, Surek and Chalmers [59] (left), and calculated with theoretical expression (3.82) (right). The values of the limiting meniscus heights are determined by equation (3.81) with the negative sign.

meniscus on the total applied pressure of the system. The form of the starting Young-Laplace equation is

$$z'' = \frac{\rho g z - p}{\gamma}[1 + z'^2]^{3/2}. \tag{3.85}$$

The two boundary conditions and the condition required to satisfy the growth angle condition are

$$z'(x_1) = -\tan(\pi/2\alpha_g), \qquad z'(x_0) = -\tan\alpha_c, \qquad z(x_0) = 0. \tag{3.86}$$

Using our solution strategy, we find the relationship between the applied pressure and the equilibrium height

$$h(p) = \frac{p}{\rho g} \pm \sqrt{\left(\frac{p}{\rho g}\right)^2 - \frac{2\gamma(\sin\alpha_g - \cos\alpha_c)}{\rho g}}. \tag{3.87}$$

Figure 3.22 shows the plot of equation (3.87) and the plot in the original paper. We see that both curves are identical to each other.

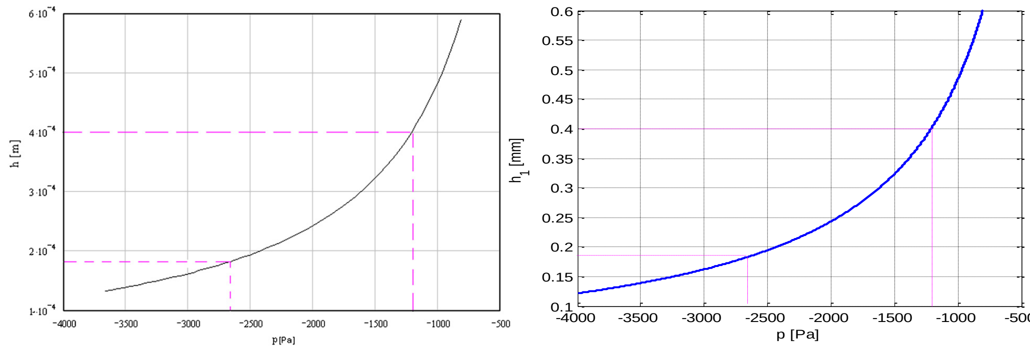

Figure 3.22: Relationship between meniscus height and applied pressure in the system. Figure on the left calculate by Balint and Balint [2]. Right figure is plotted using analytical expression (3.87).

3.9 The validity of the hydrostatic approximation in the HRG process

The validity of the hydrostatic assumption is tested by estimating two dimensionless numbers: the Weber number and the Froude number. The Weber number compares the effect of the inertial forces with respect to capillary forces and is defined by $We = \rho_l V_{pull}^2 h_1/\gamma$. For a pulling velocity of 85 cm/min (value reported by Kudo [33]), and using an equilibrium height of 10 milimeters, the Weber number is around 0.0072. The Froude number relates the inertial forces to gravity forces and is defined by $Fr = V_{pull}/(gh_1)^{1/2}$. For the conditions mentioned above, the Froude number is around 0.045. Since these two values are smaller than unity, the hydrostatic assumption is a reasonable approximation to describe the optimal operating configurations in the HRG process.

3.10 Conclusions and contributions

We presented a theoretical analysis of the lower meniscus in the horizontal ribbon growth process. By using a relatively straighforward solution method, we found an analytical expression for the height of the meniscus, an explicit solution of the governing Young-Laplace equation for the HRG process and the stability criteria for such meniscii. The solutions obtained with the analytical expressions are stable for values of $\theta \in (0, 180°)$. We noted that the stability of the meniscus is further constrained by the Gibbs's pinning limits. With these expressions, we analyzed the areas of existence of the solution for a fixed ribbon geometry, and used them to find a range of optimal pulling angles. Then, we correlated the values of the optimal region of the $\theta - \beta$ space to the corresponding values of melt levels that must be maintained to guarantee hydrostatic stability. Our results support the current design guidelines reported in the literature for an efficient extraction of a thin ribbon from the melt. Specifically, pulling the wafer at a non-zero angle in order to guarantee the existence of the lower meniscus. Pulling at an angle, implies that, the point at which the meniscus contacts the ribbon will always be higher than the melt level. Additionally, we mentioned that the use of a graphite crucible with a sharp corner is preferable over one made of silica due to its ability to allow for a wide range of contact angles. The analysis of this work presupposed that the curves describing the meniscii are single valued. In the next chapter, further theoretical analysis is done to find analytical expressions describing multi-valued solutions and their stability.

Chapter 4

Meniscus Stability in the HRG Process. Part II: The Weierstrass's Approach

All the truths of mathematics are linked to each other, and all means of discovering them are equally admissible.

– Adrien-Marie Legendre.

4.1 Introduction

The solution to geometrical problems that use variational principles can rarely be described by functions of the form $Y = F(X)$ in a Cartesian coordinate system, as we did in Chapter 3. In most cases, the stationary curves arising from the solution of the Euler-Lagrange equation are complex multivalued functions, and therefore require a less restricting and "natural" representation. Describing such curves in parametric form not only satisfies these requirements, but, as we show in this chapter, expands the solution space of the original variational problem. The variational treatment of such curves differ substantially from the classical approach that we deem it merits a separate discussion.

We begin this chapter by summarizing the fundamental concepts and main results of the variational problem in parametric form. The principal contributor to this topic was the German mathematician Karl Weierstrass (1815-1897), who, in his lectures laid the mathematical groundwork for the calculation of the first and second variation of functionals represented in parametric form. The also German mathematician Oskar Bolza (1857-1942)) presented Weierstrass's analysis in his book on calculus of variations [4], from which our summary is based upon (other useful references on this topic that we used in this section are the books by Andrew Forsyth [19] and Charles Fox [20]). We then formulate the meniscus problem within this theoretical framework, by constructing the corresponding energy function in parametric form and finding the stationary curves via the solution of the Weierstrass's form of the first variation. We find single-valued analytical solutions for the shape of the meniscus in terms of Jacobi's elliptic functions and Legendre's elliptic integrals, which we compare with a computer simulation. After finding the stationary curves, we assess their static stability by employing Weierstrass's transformation of the second variation, and finding a stability function that allows us to categorize whether a meniscus curve is at a minimum or not, via Legendre's and Jacobi's test. The hydrostatically stable curves are defined as those curves in which the total variation of the energy is positive, and the unstable curves are defined as curves in which is not possible to ensure the positivity of the variation in the energy. After finding the statically unstable shapes, we show by doing a simple proof-of-concept experiment that these unstable curves resemble the shapes of a real meniscus spilling over the corner of a crucible.

We also show how the solution to this problem is simply a special case of a more generalized Young-Laplace problem.

4.2 Fundamentals of Weierstrass's theory

In this section we present a review of Weierstrass's study of the variational problem represented in parametric form. In brief, Weierstrass found conditions under which the "classical" variational integral remains invariant when it is subject to a parametric transformation. Using straightforward calculus, he derived an expression for the first variation that provides the stationary solutions of the variational problem in terms of functions $X = \zeta(S)$ and $Y = \chi(S)$. Using a nonlinear transformation, Weierstrass also simplified the lengthy expression of the second variation and turned it into a classic quadratic functional. This transformation allowed him to apply directly the traditional results of the calculus of variations, namely Legendre's condition and Jacobi's test. A brief review of these ideas is provided next.

4.2.1 Curves in parameter representation and the condition for invariance of the integral U_0

In a two dimensional Cartesian coordinate system, a curve represented in parametric form is defined by the two equations

$$X = \zeta(S), \qquad Y = \chi(S), \tag{4.1}$$

where ζ and χ are functions of the parameter S, defined and continuous in the interval $[0, S_t]$. Consequently, the "classical" variational integral

$$U_0 = \int_0^{H_1} F\left(X, Y, \frac{dX}{dY}\right) dY, \tag{4.2}$$

becomes

$$U_0 = \int_0^{S_t} G\left(X, Y, \frac{dX}{dS}, \frac{dY}{dS}\right) dS. \tag{4.3}$$

In performing this transformation, the value of U_0 must remain invariant for any type of parametric form chosen for X and Y. Weierstrass showed that the necessary and sufficient condition for the invariance of U_0 is that the functional G be homogeneous and of degree one in the variables X' and Y', i.e.

$$G(X, Y, KX', KY') = KG(X, Y, X', Y'), \tag{4.4}$$

where the prime represents differentiation with respect to S. From this homogeneity condition, there follow several relationships between the partial derivatives of G, which are useful in constructing the expressions for the first and second variation of U_0.

4.2.2 The Weierstrass's form of the first variation

Let a stationary curve of $X-Y$ coordinates $(\zeta(S), \chi(S))$ be displaced by a small variation to the position $(\zeta(S)+\xi(S), \chi(S)+\eta(S))$, where $\xi(S)$ and $\eta(S)$ are arbitrary functions of S that vanish at the end points, so that

$$\xi(0) = \xi(S_t) = \eta(0) = \eta(S_t) = 0. \tag{4.5}$$

Let also consider the following type of variations:

$$\xi = \epsilon P(S), \qquad \eta = \epsilon Q(S), \tag{4.6}$$

where ϵ is a constant and P and Q are arbitary functions of S. Under these conditions, the first variation is defined similarly to the classical approach:

$$\delta U_0 = \int_0^{S_t} (G_X\xi + G_Y\eta + G_{X'}\xi' + G_{Y'}\eta')\, dS. \tag{4.7}$$

In this expression the subscripts of G represent differentiation with respect to X, X', Y and Y'. The structure of this formulation allowed Weierstrass to use the same logic employed in the classical variational analysis. Mainly that U_0 is stationary if X and Y, being functions of S, satisfy the Euler-Lagrange equations,

$$G_X - \frac{d}{dS}G_{X'} = 0, \qquad G_Y - \frac{d}{dS}G_{Y'} = 0. \tag{4.8}$$

Due to the homogeneity condition (4.4), these two equations are not independent of each other, as we proceed to show. Differentiating equation (4.4) with respect to K, and putting $K = 1$, yields

$$X'G_{X'} + Y'G_{Y'} = G. \tag{4.9}$$

Differentiating this expression with respect to X' and then to Y', Weierstrass showed that

$$\frac{1}{Y'^2} G_{X'X'} = -\frac{1}{X'Y'} G_{X'Y'} = \frac{1}{X'^2} G_{Y'Y'} = G_1, \tag{4.10}$$

where G_1 is the common value of these expressions. Weierstrass used this property to derive a single expression for the calculation of the first variation in the following way: Differentiating (4.4) partially with respect to X he gets

$$G_X = X' G_{XX'} + Y' G_{XY'}. \tag{4.11}$$

Using (4.10) and (4.11) in the Euler-Lagrange equation for X, yields:

$$G_X - \frac{d}{dS} G_{X'} = Y'(G_{XY'} - G_{YX'} - G_1(Y'X'' - X'Y'')). \tag{4.12}$$

Doing the same two operations for Y yields:

$$G_Y - \frac{d}{dS} G_{Y'} = -X'(G_{XY'} - G_{YX'} - G_1(Y'X'' - X'Y'')). \tag{4.13}$$

Assuming that X and Y don't vanish simultaneously in the interval $[0, S_t]$, the two expressions above are equivalent to the following differential equation:

$$G_{XY'} - G_{YX'} - G_1(Y'X'' - X'Y'') = 0. \tag{4.14}$$

This equation is the *Weierstrass's form of the Euler-Lagrange equation.* In order to solve this equation, we need to define the parameter S and its relationship with X and Y. The choice of the parameter must be such that both functions come out as single-valued functions of S; once defined, it is possible to obtain the stationary values $X = \zeta(S)$ and $Y = \chi(S)$.

4.2.3 The Weierstrass's form of the second variation

Using Taylor series representation, the second variation in parameter representation is expressed as follows:

$$\delta^2 U_0 = \int_0^{S_t} \delta^2 G \, dS, \tag{4.15}$$

where

$$\begin{aligned}\delta^2 G = G_{XX}\xi^2 + 2G_{XY}\xi\eta + G_{YY}\eta^2 + 2G_{XX'}\xi\xi' + 2G_{YY'}\eta\eta' + \\ 2G_{XY'}\xi\eta' + 2G_{YX'}\eta\xi' + G_{X'X'}\xi'^2 + 2G_{X'Y'}\xi'\eta' + G_{Y'Y'}\eta'^2.\end{aligned} \tag{4.16}$$

Recall that in order for the curve described by $Y(S)$ and $X(S)$ to be a minimum -and therefore stable-, its second variation should be positive; so the value of the intgral above must be always positive in the range of integration. Using a lengthy factorization, Weierstrass transformed the second variation into the classical quadratic functional

$$\delta^2 U_0 = \int_0^{S_t} \left[G_1 \left(\frac{d\omega}{dS} \right)^2 + G_2 \omega^2 \right] dS. \tag{4.17}$$

In the above integral we have that

$$\omega = Y'\xi - X'\eta, \tag{4.18}$$

and G_2 satisfies the following relationships:

$$G_2 = \frac{L_2}{Y'^2} = \frac{M_1}{-X'Y'} = \frac{N_1}{X'^2}, \tag{4.19}$$

with

$$L_2 = G_{XX} - Y''G_1 - \frac{dL_1}{dS}, \tag{4.20}$$

$$M_2 = G_{XY} + X''Y''G_1 - \frac{dM_1}{dS}, \tag{4.21}$$

$$N_2 = G_{YY} - X''^2 G_1 - \frac{dN_1}{dS}, \tag{4.22}$$

$$L_1 = G_{XX'} - Y'Y''G_1, \tag{4.23}$$

$$M_1 = G_{XY'} + X'Y''G_1 = G_{YX'} + Y'X''G_1, \tag{4.24}$$

$$N_1 = G_{YY'} - X'X''G_1. \tag{4.25}$$

The form of the integral allowed Weierstrass to apply the classical results of the calculus of variations. Namely, Legendre's necessary condition and Jacobi's test. Legendre's necessary condition for a minimum requires that,

$$G_1 \geq 0, \tag{4.26}$$

along the stationary curve described by $X(S)$ and $Y(S)$.

Jacobi's test requires that the solution to the differential equation,

$$G_2 u - \frac{d}{dS}\left(G_1 \frac{du}{dS}\right) = 0, \tag{4.27}$$

must not have conjugate points in the integration interval, i.e:

$$u(S) \neq 0 \quad \text{for} \quad 0 < S < S_t. \tag{4.28}$$

The strength of this theory lies in the fact that it is possible to find an extended solution space to the original meniscus problem and a more general criterion for static stability, which is not possible to accomplish with the usual Cartesian representation of a function, such as $X = X(Y)$.

4.3 Defining an energy functional in parametric form for the HRG process

In this section we use Weierstrass's theory to assess the problem of finding the additional meniscus shapes and find the unstable modes that until now we have not found. In the previous chapter, we showed that the change in the energy of the HRG process by reversibly adding a slice of melt of infinitesimal thickness is

$$dU = -PdV + \gamma dA - \gamma \cos(\sigma + \beta) dA'. \tag{4.29}$$

We also showed that in a two dimensional Cartesian coordinate system we have

$$P = \rho_l g(h_2 - y) + \rho_s g t, \quad dV = xdy. \tag{4.30}$$

In order to find the shapes of feasible meniscii described by the curves $X = \zeta(S)$ and $Y = \chi(S)$, we use the arc length s to parameterize x and y, thus defining dA as follows

$$dA = \sqrt{\left(\frac{dx}{ds}\right)^2 + \left(\frac{dy}{ds}\right)^2} ds, \tag{4.31}$$

where ds is an element of length along the meniscus profile. Similarly, we have that

$$dA' = \sqrt{\left(\left.\frac{dx}{ds}\right|_{s=s_r}\right)^2 + \left(\left.\frac{dy}{ds}\right|_{ds=s_r}\right)^2} ds = ds. \tag{4.32}$$

Putting all these terms together, yields the following expression

$$dU = -(\rho_l g(h_2 - y)) + \rho_s g t) x dy + \gamma \sqrt{\left(\frac{dx}{ds}\right)^2 + \left(\frac{dy}{ds}\right)^2} ds - \gamma \cos(\sigma + \beta) ds. \tag{4.33}$$

Nondimensionalizing length scales with respect to a capillary constant

$$a = \sqrt{\gamma/(\rho_l g)}, \tag{4.34}$$

and integrating yields the expression for the energy functional of the HRG process

$$\begin{aligned} &U_0\left(X, Y, \frac{dX}{dS}, \frac{dY}{dS}\right) = \\ &\int_0^{S_t} \left[X\left(Y - H_2 - \frac{\rho_s}{\rho_l}T\right)\frac{dY}{dS} + \sqrt{\left(\frac{dX}{dS}\right)^2 + \left(\frac{dY}{dS}\right)^2} - \cos(\sigma + \beta)\right] dS, \end{aligned} \tag{4.35}$$

where

$$U_0 = \Delta U \gamma^{-\frac{3}{2}} (\rho_l g)^{\frac{1}{2}},\ x = aX,\ y = aY,\ t = aT,\ s_t = aS_t \text{ and } h_2 = aH_2. \tag{4.36}$$

The functional inside of the integral is homogeneous degree one in the variables X' and Y', thus the results of Weirstrass's can be applied to find the stationary curves and stability conditions.

4.4 Calculating the stationary curves via the first variation

The stationary curves are found by solving the Weierstrass's form of the Euler-Lagrange equation

$$G_{XY'} - G_{YX'} - G_1(Y'X'' - X'Y'') = 0. \tag{4.37}$$

In our case we have that

$$
\begin{aligned}
G_1 &= \frac{1}{(X'^2+Y'^2)^{3/2}}, && (4.38)\\
G_{XY'} &= Y - H_2 - \frac{\rho_s}{\rho_l}T, && (4.39)\\
G_{YX'} &= 0. && (4.40)
\end{aligned}
$$

So the Euler-Lagrange equation becomes:

$$H_2 + \frac{\rho_s}{\rho_l}T - Y = \frac{X'Y'' - X''Y'}{(X'^2+Y'^2)^{3/2}}. \tag{4.41}$$

Equation (4.41) is the governing Young-Laplace equation of the HRG process in parametric form. The term to the right hand side of the equation is also known as the *curvature*. In order to find the parametric solutions $X = \zeta(S)$ and $Y = \chi(S)$ we use the relationships

$$
\begin{aligned}
X' &= \cos\Omega, && (4.42)\\
Y' &= \sin\Omega, && (4.43)\\
X'' &= -\sin\Omega\Omega', && (4.44)\\
Y'' &= \cos\Omega\Omega', && (4.45)
\end{aligned}
$$

where Ω is the tangential angle to the meniscus, and turn the Young-Laplace equation into

$$\Omega' = H_2 - Y + \frac{\rho_s}{\rho_l}T = H_1 - L\sin\beta - Y + \frac{\rho_s}{\rho_l}T. \tag{4.46}$$

From this transformation, we see that the Young-Laplace equation is split into a system of three differential equations: equations (4.42), (4.43) and (4.46). The conditions at the boundary are

$$X(0) = X_c, \quad Y(0) = 0, \quad \Omega(0) = \theta. \tag{4.47}$$

The integration of this system of equations is carried up to the point where the following conditions are met

$$Y(S_t) = H_1, \tag{4.48}$$

$$\Omega(S_t) = \sigma + \beta. \tag{4.49}$$

The analytical solution for $Y(S)$ is given by

$$\begin{aligned} Y(S) = \pm\sqrt{\left(\frac{\rho_s}{\rho_l}T - L\sin\beta\right)^2 + 2\cos\theta - 2\cos(\sigma+\beta)} \\ +\sqrt{2-A}\,\mathbf{sn}\left(\frac{\sqrt{2+A}}{2}S + \mathbf{F}(\Psi_0|\kappa)\middle|\kappa\right), \end{aligned} \tag{4.50}$$

where $\mathbf{sn}(\boldsymbol{\Theta}|\kappa)$ is one of the twelve Jacobi elliptic functions, $\mathbf{F}(\Psi_0|\kappa)$ is the incomplete elliptic integral of the first kind, and

$$\Psi_0 = \arcsin\left(\mp\sqrt{\frac{2\cos\theta - A}{2-A}}\right), \tag{4.51}$$

$$A = 2\cos(\sigma+\beta) - \left(\frac{\rho_s}{\rho_l}T - L\sin\beta\right)^2, \tag{4.52}$$

$$\kappa = \sqrt{\frac{A-2}{A+2}}. \tag{4.53}$$

The solution for $X(S)$ is given by

$$\begin{aligned} X(S) = X_c - S + \sqrt{A+2}\left[\frac{\mathbf{E}(\mathbf{am}(\Psi_S|\kappa)|\kappa)\sqrt{1-\kappa^2\,\mathbf{sn}(\Psi_S|\kappa)^2}}{\mathbf{dn}(\Psi_S|\kappa)}\right] - \\ \sqrt{A+2}\left[\frac{\mathbf{E}(\Psi_0|\kappa)\sqrt{1-\kappa^2\,\mathbf{sn}\left(\mathbf{F}(\Psi_0|\kappa)|\kappa\right)^2}}{\mathbf{dn}\left(\mathbf{F}(\Psi_0|\kappa)|\kappa\right)}\right], \end{aligned} \tag{4.54}$$

where $\mathbf{E}(\Theta|\kappa)$ is the incomplete elliptic integral of the first kind, $\mathbf{am}(\Theta|\kappa)$ is the Jacobi amplitude, $\mathbf{dn}(\Theta|\kappa)$ is a Jacobi elliptic function, and,

$$\Psi_S = \frac{\sqrt{2+A}}{2}S + \mathbf{F}(\Psi_0|\kappa). \tag{4.55}$$

Lastly, the solution for $\Omega(S)$ is:

$$\Omega(S) = 2\,\mathbf{am}\left(\mp\frac{\sqrt{2-A}}{2}S + \mathbf{F}\left(\frac{\theta}{2}\middle|\frac{2}{2-A}\right)\middle|\frac{4}{2-A}\right). \tag{4.56}$$

The detailed solution method for the system of differential equation and its comparison with the numerical integration are shown in the Appendix C. The definitions of the elliptic functions and elliptic integrals are found in Appendix D.

4.5 Finding the conditions for stability via the second variation

Assuming that the curves are perturbed by the same function (i.e. $\eta = \xi$), Weierstrass's transformation

$$\delta^2 U_0 = \int_0^{S_t} \left[G_1 \left(\frac{d\omega}{dt} \right) + G_2 \omega^2 \right] dS, \tag{4.57}$$

applied to our problem yields

$$\begin{aligned}
\omega &= Y'\xi - X'\eta = \eta(Y' - X'), \\
L_1 &= G_{XX'} - Y'Y''G_1 = -Y'Y'', \\
N_1 &= G_{YY'} - X'X''G_1 = X - X'X'', \\
M_1 &= G_{XY'} + X'Y''G_1 = G_{YX'} + Y'X''G_1 = Y - H_2 - \frac{\rho_s}{\rho_l}T + X'Y'' = Y'X'', \\
L_2 &= G_{XX} - Y''^2 G_1 - L_1' = Y'Y''', \\
M_2 &= G_{XY} + X''Y''G_1 - M_1' = -X'Y''' = Y' - Y'X''', \\
N_2 &= G_{YY} - X''^2 G_1 - N_1' = -X' + X'X'''.
\end{aligned}$$

Weierstrass showed that there exists a function G_2 such that,

$$G_2 = \frac{L_2}{Y'^2} = \frac{-M_2}{X'Y'} = \frac{N_2}{X'^2}. \tag{4.58}$$

In our case, we have that

$$G_2 = \frac{X''' - 1}{X'} = \frac{Y'''}{Y'}. \tag{4.59}$$

Also, recall that

$$G_1 = \frac{1}{(X'^2 + Y'^2)^{3/2}}. \tag{4.60}$$

We see immediately from these expressions that Legendre's condition for a minimum is satisfied, since $G_1 \geq 0$ throughout the curve.

In order to have the Jacobi test satisfied we require that the solution to the differential equation

$$G_2 u - (G_1 u')' = \frac{Y'''}{Y'} u - u'' = 0, \tag{4.61}$$

must not have conjugate points in the interval of integration, i.e.

$$u(S) \neq 0 \text{ for } 0 < S < S_t. \tag{4.62}$$

Expression (4.61) is equivalent to:

$$(Y'u' - Y''u)' = 0. \tag{4.63}$$

Thus

$$Y'u' - Y''u = K_1. \tag{4.64}$$

Dividing the expression above by Y'^2 we get:

$$\frac{Y'u' - Y''u}{Y'^2} = \left(\frac{u}{Y'}\right)' = \frac{K_1}{Y'^2}. \tag{4.65}$$

So the condition for stability becomes,

$$u(S) = K_1 Y(S)' \int_0^{S_t} \frac{dS}{Y(S)'^2} \neq 0 \text{ for } 0 < S < S_t. \tag{4.66}$$

The integral in expression (4.66) is always positive as long as $Y(S) \neq 0$ between 0 and S_t (given $S_t > 0$), otherwise the integral does not converge. The term $K_1 Y(S)'$ does not change sign as long as $Y(S)'$ does not change sign in the $(0, S_t)$ interval. Therefore the issue of stability reduces to finding the range of values for which $Y(S)'$ crosses zero in the $(0, S_t)$ interval. This is easier to analyze recalling the fact that $Y(S)' = \sin \Omega(S)$, where $\Omega(S)$ is the tangential angle of the meniscus with respect to the horizontal axis. If $\sin \Omega(S)$ is always positive or always negative in the integration interval, the function $u(S)$ will be a well defined function with no conjugate points. Thus we simplify our stability criterion to the following expression:

$$\sin(\Omega(S)) > 0 \vee \sin(\Omega(S)) < 0 \ \forall \ S \in (0, S_t), \tag{4.67}$$

where,

$$\begin{aligned} \sin(\Omega(S)) = P(S) = 2\,\mathbf{sn}\left(\mp\frac{\sqrt{2-A}}{2}S + \mathbf{F}\left(\frac{\theta}{2}\middle|\frac{2}{2-A}\right)\middle|\frac{4}{2-A}\right) \times \\ \mathbf{cn}\left(\mp\frac{\sqrt{2-A}}{2}S + \mathbf{F}\left(\frac{\theta}{2}\middle|\frac{2}{2-A}\right)\middle|\frac{4}{2-A}\right) \end{aligned} \tag{4.68}$$

In this expression, $\mathbf{cn}(\Theta|\kappa)$ is a Jacobi elliptic function. Thus, Jacobi's necessary condition requires that $P(S)$ does not change sign in the interval $(0, S_t)$.

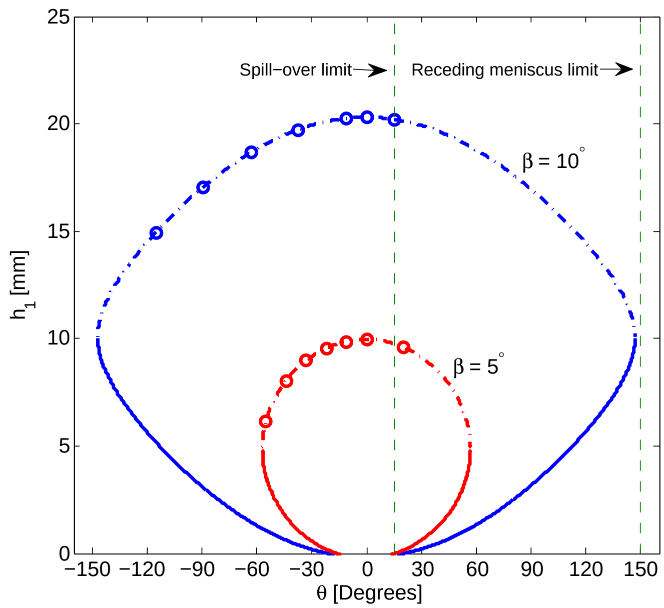

Figure 4.1: The extended diagram of the relationship between the equilibrium height and the contact angle. Circles correspond to the meniscii plotted in figures 4.2 and 4.3.

4.6 Illustration of the results

In this section we show that the parametric solutions to the meniscus problem capture an array of feasible multivalued functions that satisfy the Young-Laplace equation but are not necessarily stable. We use the same case study as in previous chapter: a silicon ribbon of 400 microns in thickness and 6 centimeters in length pulled out from the molten bath at angles of 5° and 10°; the melt rests on a graphite crucible with a sharp edge ($\phi = 45°$). In order to plot the meniscii, we first use the expression for the meniscus height to calculate the point where the ribbon touches the ribbon at an angle of $\sigma + \beta$; then, using the analytical expression for $Y(S)$, we find the value of the arc length S_t that yields the value of $Y(S_t) = H_1$. Once we find this value, we plot parametrically the curve described by $X(S)$ and $Y(S)$ from 0 to S_t.

In Figure 4.1 we show the extended diagram of the relationship between the equilibrium height of the meniscus and the contact angle, for pulling angles of 5° and 10°. The extended region is the symmetric counterpart to the region we showed in the previous chapter. We see that all meniscii in this region lie outside the Gibbs's limits defining spill-over and receding conditions, and therefore are never pinned to the corner of the crucible. The fact that these additional configurations lie to the left of the spill-over limit, can be interpreted as snapshots of meniscii that are "in the process" of spilling over from the corner of the crucible. From the diagram we also see that due to symmetry of the curves it is possible to obtain two different meniscii with the same equilibrium height, and therefore the same melt level (since $h_2 = h_1 - l \sin \beta$); this means that a transition from a pinned stable to a pinned unstable configuration can occur while keeping having the same melt level, pulling angle, ribbon thickness and ribbon length.

The additional meniscii are those corresponding to values of contact angles lower than zero, and are represented by the parametric solution, which we plot in Figures (4.2) and (4.3). These curves correspond to the blue and red circles in the $h_1 - \theta$ digram, respectively. With our parametric solution, we capture the whole solution space of the meniscus problem (in figures 4.2 and 4.3 we show two meniscii with values of $\theta > 0$), and show that the newly found curves are characterized mathematically by the multi-valued relationship between X and Y. From a physical point of view, these meniscii are "bulked" at the bottom, suggesting a hydrostatically unstable configuration.

In order to illustrate the concept of the stability of the newly found curves, we focus on the results obtained from Jacobi's test (Legendre's condition for a minimum is always satisfied for all shapes). Figures 4.4 and 4.5 show the stability function $P(S)$ for the two cases under study. As we mentioned before, the stability function must not have conjugate points between 0 and S_t. In other words, the function $P(S)$ must not cross zero in the said interval. From these figures we see that the stability limit is given by $\theta = 0$. Contact angles greater than zero are statically

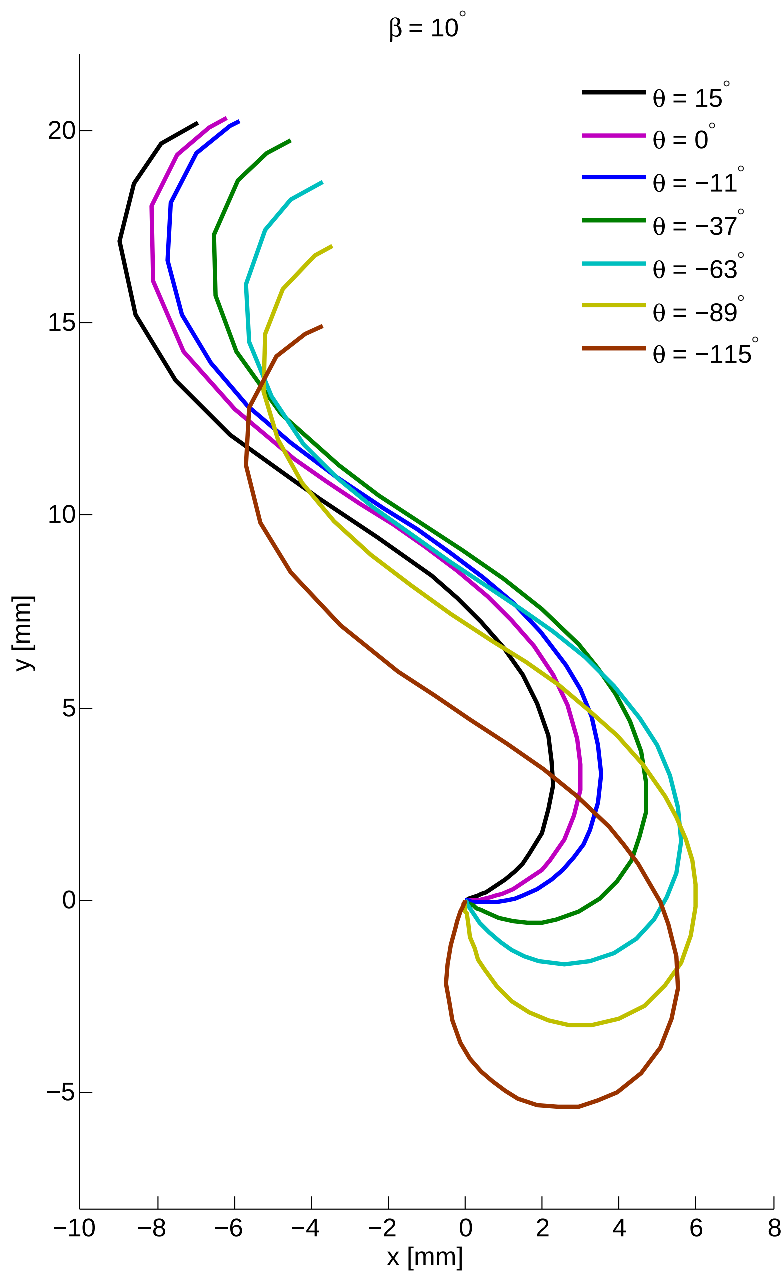

Figure 4.2: The additional meniscus shapes obtained with the analytical solution in parametric form. Curves correspond to a value of $\beta = 10°$.

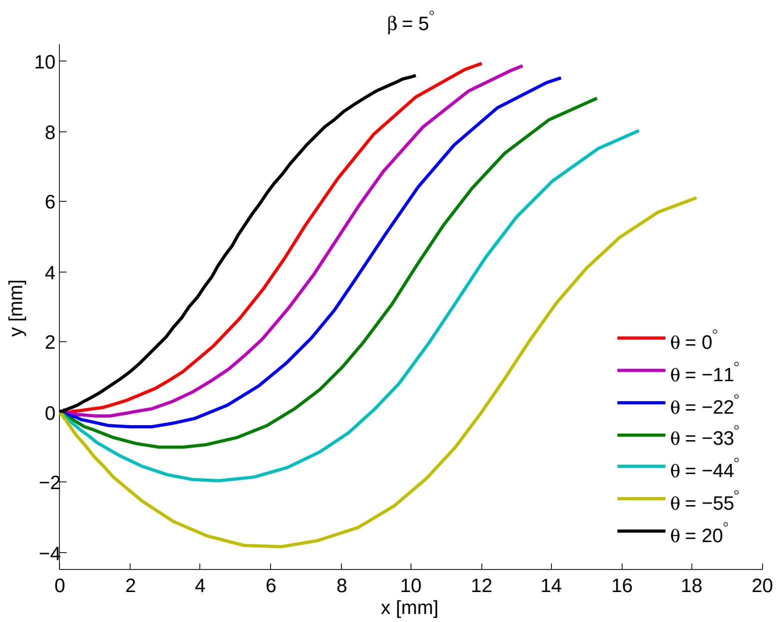

Figure 4.3: The additional meniscus shapes obtained with the analytical solution in parametric form. Curves correspond to a value of $\beta = 5°$.

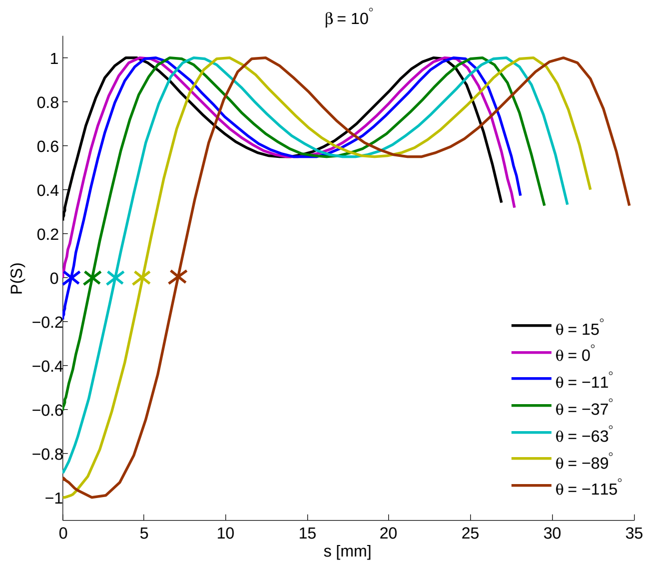

Figure 4.4: The stability function $P(S)$ for different contact angles and $\beta = 10°$. The cross in each curve indicate where the curves cross zero.

stable, as we show in the case when $\beta = 10°$ and $\theta = 15°$ in figure (4.2), and in the case when $\beta = 5°$ and $\theta = 20°$ in figure (4.3). The stability function in these two cases is always positive, never crossing zero, whereas the curves for values of contact angle lower than zero cross the horizontal axis and therefore have conjugate points. All meniscii with contact angles less than zero are pinned unstable and statically unstable.

A possible cause of transition from the stable to unstable modes in an HRG operation is better understood by constructing a representation to scale of the HRG system. Figures 4.6 and 4.7 show to sets of HRG configurations, where we represent graphically the melt level, the ribbon length, the crucible, and the shape of the meniscus (ribbon thickness is the only variable not drawn to scale). Each HRG configuration shows a stable (solid line) and an unstable mode (dashed line). We plot configurations that correspond to opposite points in the $h_1 - \theta$ diagram which yield the same melt height for two different values of contact angle. In both repre-

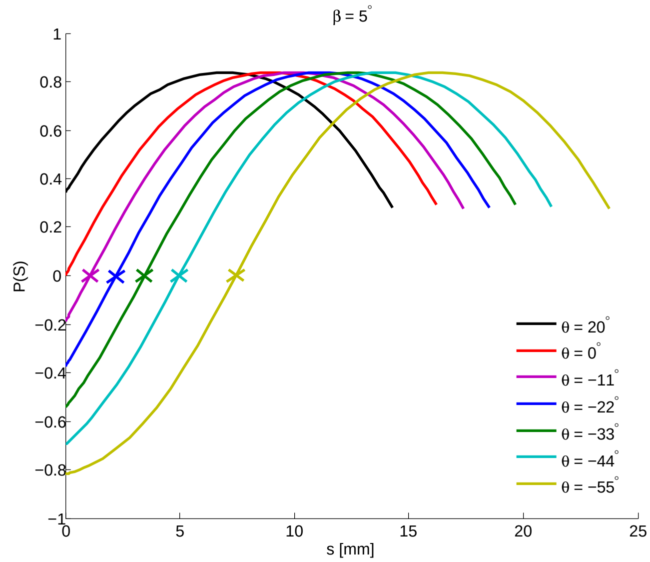

Figure 4.5: The stability function $P(S)$ for different contact angles and $\beta = 5°$. The cross in each curve indicate where the curves cross zero.

sentations, the unstable modes place the melt-gas-ribbon triple point to the right of the stable mode, which intuitively suggest that the unstable modes and potential spill-over could be caused by a sudden increase in the pulling speed of the system.

In order to test qualitatively our hypothesis of the proposed spill-over mechanism we use a miniature proof-of-concept HRG system, in which we use a polyethlyene ribbon ($\rho_{pe} = 0.93kg/m^3 > \rho_{water}$), resting on water contained in the plastic bath. The ribbon rests completely on top of the water and is extracted from the batch with a conveyor belt. We induce the spill-over by slowly increasing the conveyor belt speed while photographing the change in the shape of the water meniscus. Figure (4.8) shows the bulking of the meniscus as the pulling speed increases. Despite the difference in the materials, the shapes of the stable (top-left photograph) and the spilling meniscus (bottom-right photograph) are very similar to those obtained with our theoretical findings. We would expect the same pattern in a silicon system.

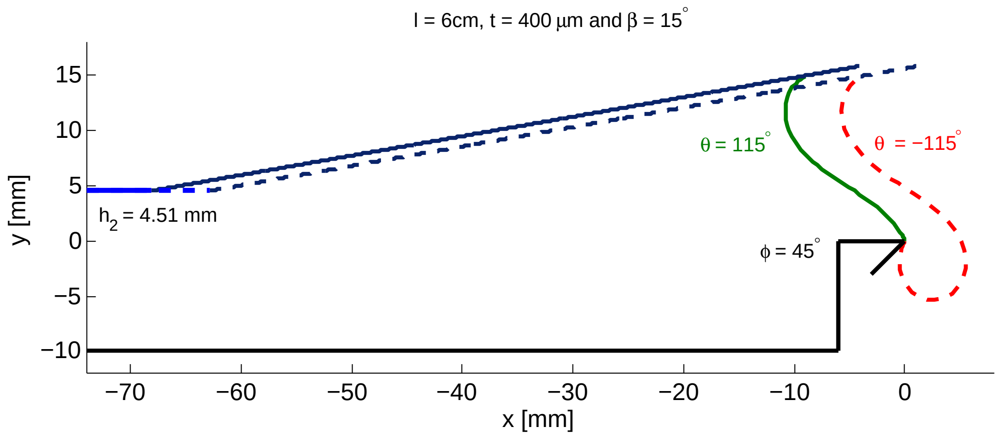

Figure 4.6: A sketch of a hydrostatically stable (green) and unstable (red) configuration for $\beta = 10°$. The unstable mode does not satisfy the Jacobi test nor Gibbs' pinning condition.

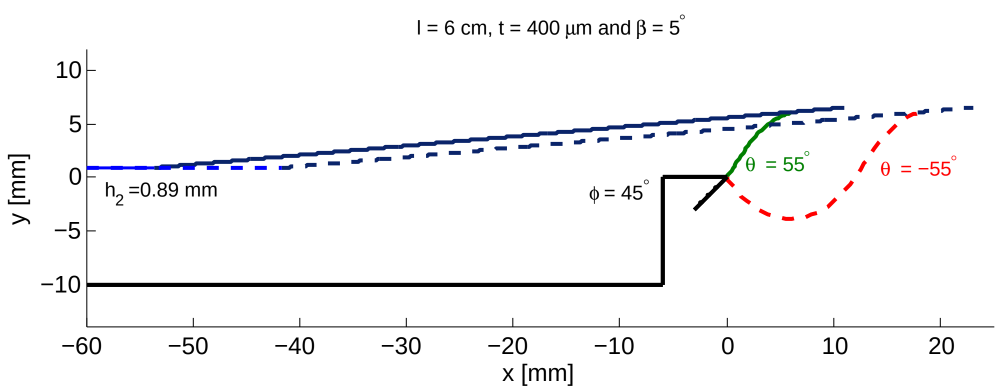

Figure 4.7: A sketch of a hydrostatically stable (green) and unstable (red) configuration for $\beta = 5°$. The unstable mode does not satisfy the Jacobi test nor Gibbs' pinning condition.

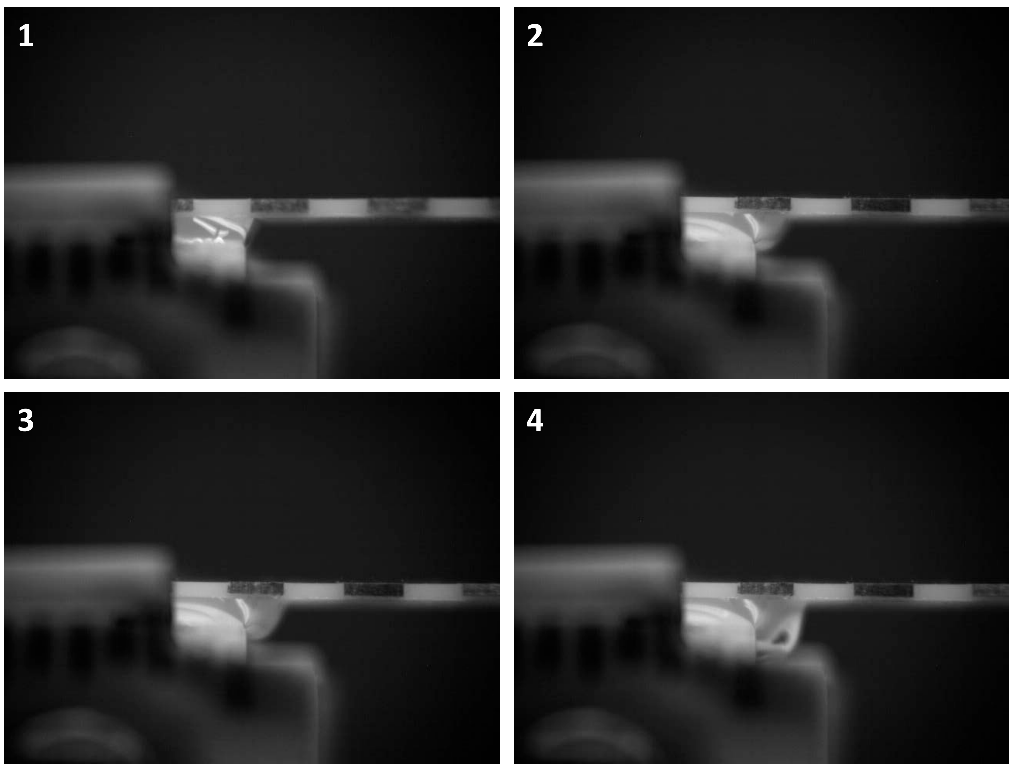

Figure 4.8: A sequence of photographs showing the meniscus spilling over from the corner of the plastic bath.

4.7 Generalized solutions of a Young-Laplace equation

For a two dimensional curve described in parametric form by $X(S)$ and $Y(S)$, a general form of the Young-Laplace equation can be stated as follows:

$$H - Y = \frac{X'Y'' - X''Y'}{(X'^2 + Y'^2)^{3/2}}, \tag{4.69}$$

where H is the applied -and dimensionless- pressure. We showed that this equation can be split into a system of three differential equations

$$\frac{dY}{dS} = \sin\Omega, \quad \frac{dX}{dS} = \cos\Omega, \quad \frac{d\Omega}{dS} = H - Y. \tag{4.70}$$

For a general case, the initial conditions are

$$Y(0) = 0, \quad X(0) = 0, \quad \Omega(0) = \theta, \tag{4.71}$$

where θ is angle at which the curve departs from the origin. In this chapter we derived analytical solutions for $X(S)$, $Y(S)$ and $\Omega(S)$, and use them in the analysis of stability of the meniscus in the HRG process. From a purely mathematical point of view, the solution to this differential equation presents very interesting behaviours beyond the integration limits imposed by the conditions of the meniscus problem. Figures 4.9 and 4.10 show the analytical solution to the general form of the Young-Laplace equation for different values of H and θ. The solutions are plotted for a value of arc-length equal to 20. These curves vary greatly in their shape, exhibiting sinusoidal-type patterns and and cyclic-type patterns (the case when $H = 1$ and $\theta = 120°$ does exhibit a regular pattern when plotted beyond $S_T = 20$), which could never be captured by a single-valued function such as $X = F(Y)$.

Looking for an exception in this regular-pattern behaviour, we did a sensitivity analysis and plotted solutions for the same value of θ while changing the parameter H, and found that the system is very sensitive to small changes in this parameter. Figure 4.11 shows two solutions for the case when $\theta = -150°$. We see that the curves exhibits a regular pattern when $H = 0.52$, but does not when $H = 0.51$. The explanation for this behaviour is beyond the scope of this work, but this finding

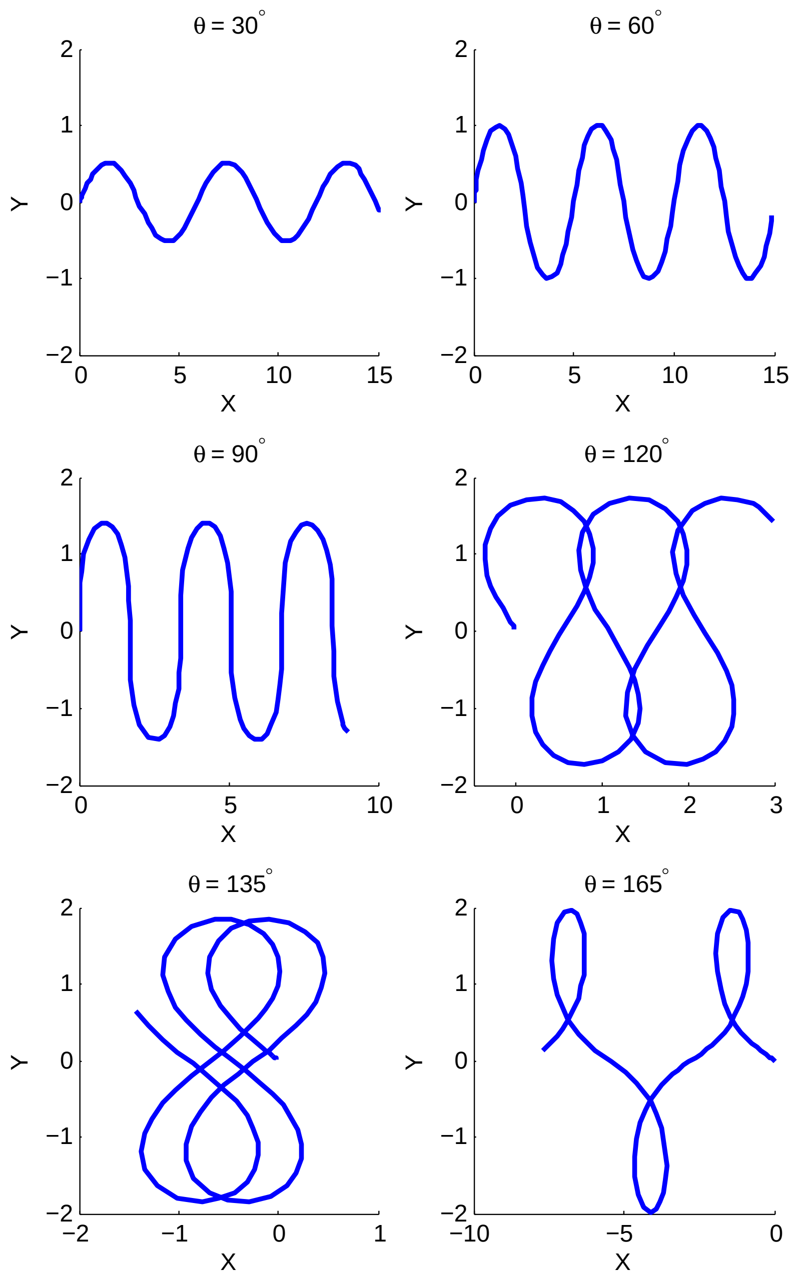

Figure 4.9: Several solutions to the Young-Laplace equation (equation (4.69)) for $H = 0$.

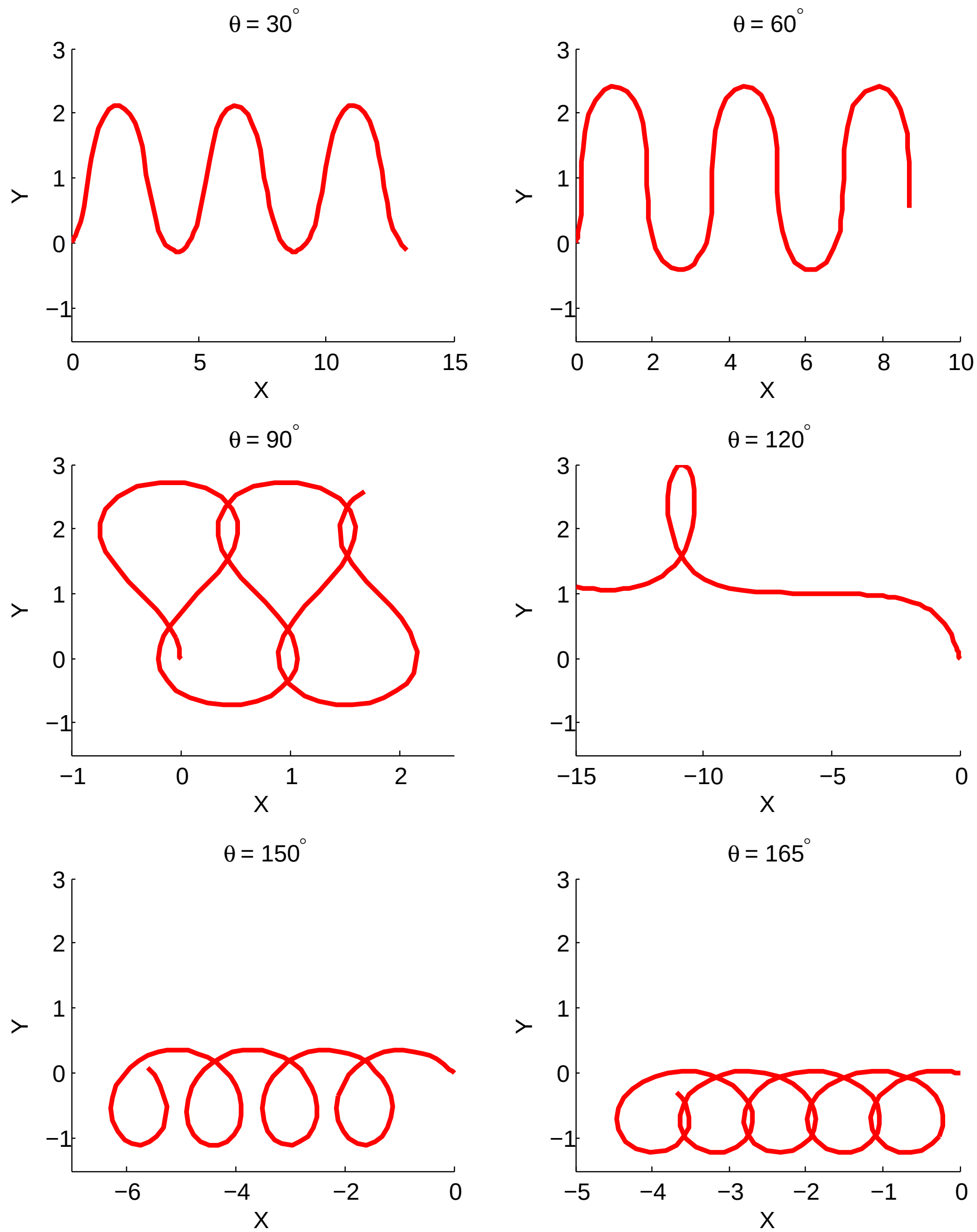

Figure 4.10: Several solutions to the Young-Laplace equation (equation (4.69)) for $H = 1$.

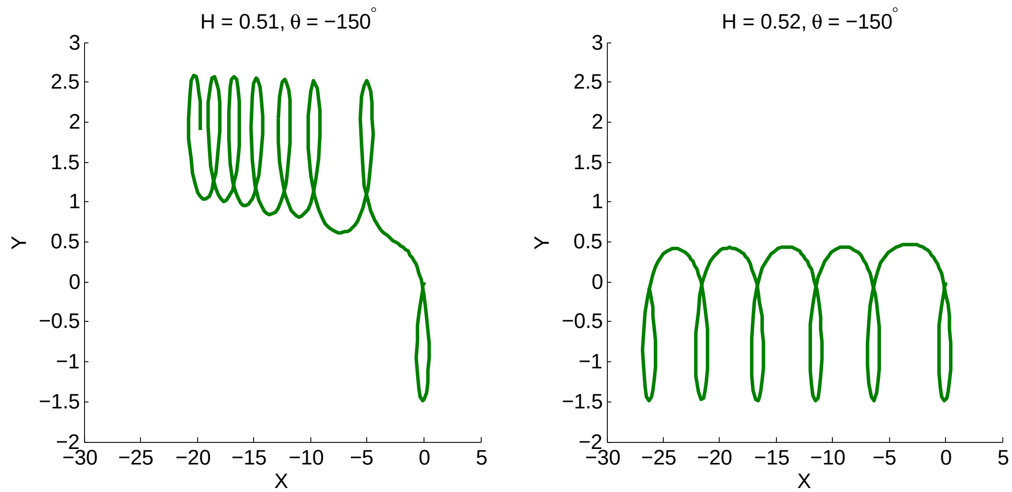

Figure 4.11: Sensitivity of solutions to a small change in the parameter H.

explains very well the fact that, even though the system of differential equations looks very simple, the underlying behaviour of its solution is rather complex. And this is very well seen in the mathematical structure of the analytical solution. To the best of the author's knowledge, this analytical solution in parametric form has not yet been reported in the literature. We believe that these analytical solutions could not only be studied and exploited in a purely mathematical sense, but also be applied in many physical and engineering applications, far beyond crystal growth processes.

4.8 Conclusions and contributions

In this chapter, we formulated and solved the generalized meniscus problem of the HRG process. Using Weierstrass's variational theory, we found analytical expressions describing the shapes of the additional meniscii in parametric form. These curves, which are represented in terms of Jacobi's elliptic functions and Legendre's elliptic integrals, are statically unstable whenever the contact angle is below zero.

This criterion, along with the fact that such curves are beyond the pinning conditions established by Gibbs, imply that the newly obtained meniscii can be interpreted as "snapshots" of a spill-over configuration. We supported this argument by doing a simple experiment, in which we recreate the spill-over phenomena using a polyethlyene ribbon resting on a bath of water. The shapes of the spill-over configurations are in good qualitative agreement with the shapes found with our theoretical calculation. Finally, we noted that the analytical shapes of the meniscii in the HRG process are part of a general solution space of a type of Young-Laplace equations. All these findings are novel contributions to the field.

4.9 List of symbols used in previous two chapters

Symbol	Definition
α	Contact angle in Swartz et. al [59] work
α_g	Growth angle in Balint and Balint [2] work
α_c	Contact angle in Balint and Balint [2] work
β	Pulling angle
γ	Liquid-gas interfacial energy
γ_{sl}	Solid-liquid interfacial energy
γ_{sv}	Solid-vapor interfacial energy
θ	Angle between horizontal and meniscus curve
θ_{eq}	Equilibrium contact angle
θ_g	Contact angle (supplement of θ)
κ	Elliptic modulus
σ	Silicon growth angle
ρ_l	Density of molten silicon
ρ_s	Density of solid silicon
Ω	Tangential angle to the meniscus
ϕ_0	Growth angle in Swartz et. al study [59]
a	Capillary constant
g	Acceleration of gravity
h_1	Meniscus height
h_2	Melt level
h_{eff}	Effective height in Swartz et al. [59] work
l	Length of the ribbon
t	Ribbon thickness

Table 4.1: List of variables and parameters used in the previous two chapters.

Chapter 5

Crystallization Dynamics and Interface Stability in the HRG Process

5.1 Introduction

In the growth of the silicon ribbon, it may be necessary to process a raw material with a wide range -and often large amount- of impurities. The quality and efficiency of the solar panel depends critically on the purity level of the elements present in the wafer. Impurities such as iron, nickel, cobalt and copper diminish considerably the minority carrier lifetime, whereas aluminum and titanium reduce the effciency of the cell. Metallurgical grade silicon, the predecessor of solar-grade silicon, containts at least ten or more impurities, each of them affecting the quality of the final product (see Table 5.1). In addition, some impurities present in the final product are incorporated in the growth process: crystals grown in quartz crucibles are prone to oxygen entrainment into the melt, and those grown in graphite crucibles are susceptible to carbon entrainment and the formation of silicon carbide. Lastly, crystallization of the silicon melt also affects the amount of impurities of

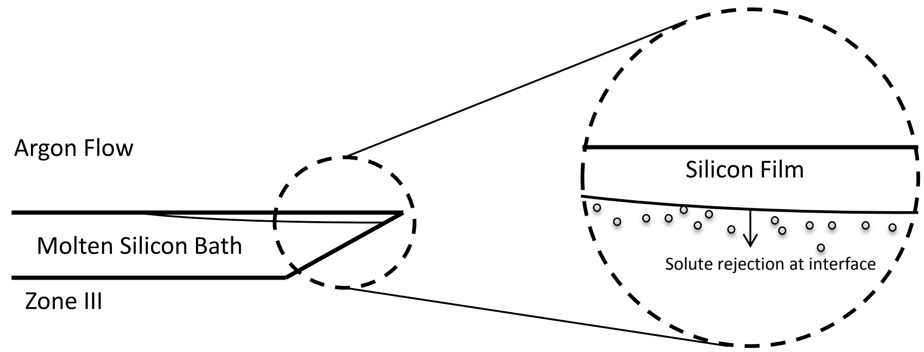

Figure 5.1: Solute is rejected at the interface due to the large difference in impurity solubility in the two phases.

the final material, due to the difference in the segregation coefficients between the solid and liquid phase. The segregation of impurities might induce the formation of a solute-enriched boundary layer close to the interface, which might trigger the growth of dendrites, which in turn affect the quality of the wafer. In the HRG process, Kudo [33] and Kellerman [63] reported the formation of dendrites at the interface, which we attribute to perturbations applied to a crystallization system with a high concentration of solutes near the interface.

In this chapter we focus on the phenomena of solute rejection and its effect on the stability of the solid-liquid interface in the HRG process. First, we give a brief overview of the fundamentals of crystallization and interfacial stability; then we develop a mathematical model to describe the crystallization dynamics in the HRG system, when a given concentration of aluminum is present in the silicon melt. Once the unperturbed dynamics have been studied, we formulate and solve the problem of stability for the conditions given by the mathematical problem.

5.2 Basic principles of solute segregation in crystal growth from the melt

The process of crystallization is also a process of purification, since there is usually a large difference in the solubility of impurities between the melt and the crystal. Impurity atoms tend to diffuse preferentially in the liquid; as the crystal grows, impurities are rejected from the solid and transported from the interface to the melt. This manifests in the formation of a solute enriched boundary layer close to the crystallization front. Quantitatively, this difference in solubility is given by the segregation coefficient, which represents the extent of solute rejection from the solid to the liquid. As solidification proceeds, solute is redistributed among the two phases depending on the magnitude of this coefficient and the mass diffusivities of each individual impurity. The velocity of the crystallization front determines the extent of the diffusion boundary layer at the interface [55]. At low velocities, the concentration profile in the melt is uniform throughout the sample, whereas at high velocities, solute will build up close the the front. In many cases, low solidification velocities guarantee an equilibrium type behaviour in the system, i.e. segregation follows the exact path of the phase diagram. An estimate of the extent of the boundary layer thickness dependency on both the interface velocity, V, and the liquid diffusivity, D_L, of the solute neglecting the effects of convection is given by

$$\delta = \frac{D_L}{V}. \tag{5.1}$$

For a given diffusivity coefficient, large interface velocities tend to “trap” the solute in a small region close to the interface. The formation of the impurity layer at the liquid-solid interface is detrimental for the process since it can cause steep concentration gradients that induce morphological instabilities, i.e. dendritic growth [41]. The inclusion of impurities in the ribbon leads to defects that cause recombination and reduced solar cell efficiency.

Element	k_0	Element	k_0
B	0.75	Ti	3.6×10^{-4}
Al	0.002	Cr	1.1×10^{-5}
Ga	0.008	Mn	1×10^{-5}
N	7×10^{-4}	Fe	8×10^{-6}
P	0.35	Co	8×10^{-6}
As	0.3	Ni	8×10^{-6}
C	0.07	Cu	4×10^{-4}
O	0.85	Zn	1×10^{-5}

Table 5.1: Segregation coefficients for some elements in silicon at the melting point. Adapted from [8].

5.3 Basic principles of the Mullins-Sekerka stability theory

Mullins and Sekerka [41] developed the theoretical foundation for the conditions required to maintain a stable crystallization front when it is subject to an arbitrary sinusoidal perturbation of the form $I(x,t) = \delta(t)sin(\omega x)$ (see Figure 5.2). Under this theory, surface tension and temperature gradients at each side of the interface promote stability and favor the decay of the perturbation. On the other hand liquid concentration gradients next to the interface caused by solute rejection, promote the growth of the perturbation. The physical explanation of this phenomena is the following: by applying a perturbation to a flat surface, the thermal and concentration fields are also perturbed. A hill or valley of the sinusoidal wave ahead or behind the rest of the interface, finds itself in a thermally unfavorable situation. If a tip of solid protruded into the liquid is surrounded by a domain that is at a higher temperature (above the melting point), heat will flow from the liquid to the solid tip to equilibrate the thermal profile. Thermal gradients -in the form of heat flow-, then, are stabilizing forces. The stabilizing effect of surface tension is given

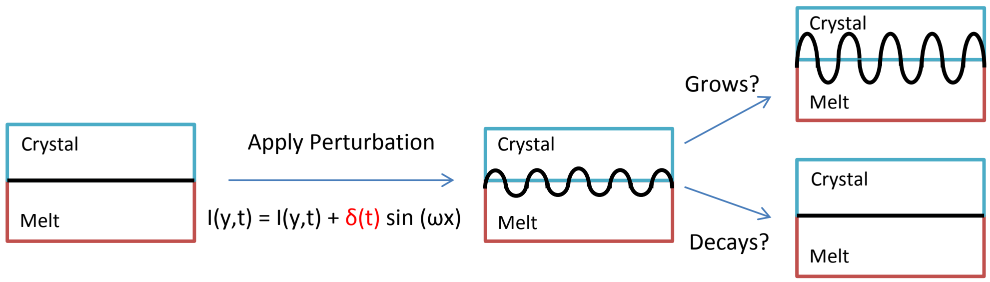

Figure 5.2: Representation of the Mullins-Sekerka stability analysis.

by the fact that it will always try to minimize the surface area of the system, hence the low free energy planar morphology is preferred over the high free energy curved interface.

Concentration gradients, on the other hand, are destabilizing. It has been demonstrated through experiments that these gradients can overcome the stabilizing effects of the thermal gradients and the interfacial free energy. The destabilizing effect can be understood as follows: the effect of melting point depression due to the presence of solutes creates a phenomenon known as solutal undercooling close to the front. When a sufficiently undercooled tip is protruded into the melt, it might not be immediately surrounded by a domain of a higher temperature since the undercooling lowers the temperature around the tip and acts as a counteracting force to the heat flow coming from the liquid. If the undercooled tip overcomes the heat flux and surface tension, the morphology of the interface changes from planar to a cellular pattern, and the flat interface breaks down. These cellular patterns are the precursors of the dendritic structure generally present in most casting operations. For our system, the formation of these dendrites is detrimental since we aim to produce a crystal with a morphologically smooth surface, leading to the production of a perfect, mono-crystalline sheet of silicon.

Mullins and Sekerka derived stability conditions that take into account the phenomena described above to show how stability depends on mass and energy transport together with material properties. In their analysis, they assumed a system operating at steady state with a constant interfacial velocity (in an experimental set-up, this is equivalent to having a furnace moving at a velocity V relative to the sample). These factors allowed them to find an analytical expression for the growth or decay of the perturbation. The stability conditions were given in terms of a frequency dependent ratio between a perturbation in the gradient of the velocity of the freezing front relative to a perturbation in its velocity so that

$$\frac{\dot{\delta}}{\delta} = F(\omega). \tag{5.2}$$

The parameter ω represents the angular frequency and

$$\begin{aligned} F(\omega) = {} & \frac{V\omega\left\{-2T_M\Gamma\omega^2\left[\omega^* - \left(\frac{V}{D_l}\right)p\right] - (G'+G)\left[\omega^* - \left(\frac{V}{D_l}\right)p\right]\right\}}{(G'-G)\left[\omega^* - (V/D)p\right] + 2\omega m G_c} \\ & + \frac{2mG_c\left[\omega^* - \left(\frac{V}{D_l}\right)\right]}{(G'-G)\left[\omega^* - (V/D)p\right] + 2\omega m G_c}. \end{aligned} \tag{5.3}$$

They show that the flat surface is stable if $F(\omega) < 0$ for all $\omega > 0$. In this expression V is the velocity of the interface, T_M the melting point, Γ a capillary constant, D_l is the solute diffusivity in the liquid, G' and G are the temperature gradients of the crystal and the melt at the interface respectively, multiplied by an average conductivity, $\bar{k} = 0.5 \times (k_s + k_l)$, m is the slope of the liquidus line in a binary phase diagram. G_c is the concentration gradient at the interface and $p = 1 - k_{seg}$, where k_{seg} is the segregation coefficient. Finally

$$\omega^* = \frac{V}{2D_l} + \left[\left(\frac{V}{2D_l}\right)^2 + \omega^2\right]^{\frac{1}{2}}. \tag{5.4}$$

With these concepts in mind, the goal of the proceeding analysis is to calculate the extent of purification that can be achieved in the crystallization of the thin wafer via the HRG process and the potential formation of a solute enriched boundary layer. Then, we perform a stability analysis based on our mathematical model, which accounts for transient effects, variable interface velocities and a finite domain.

5.4 Modeling crystallization in the HRG process

We describe crystallization in the HRG process by assuming a system composed by a solid and liquid subdomains divided by a sharp interface. We assume that transport phenomena at the surface of the melt will be dominated by heat and mass diffusion, since for the formation of the film, only a thin layer of the melt is affected (less than half a milimeter) and bulk phenomena such as the fluid currents can be offset by maintaining an appropriate thermal gradient and inlet velocity. These assumptions transform the mathematical formulation of the problem into an extension of the classical Stefan (1835-1893) problem [43]. Also, we calculate the shape of the ribbon by constructing a one-dimensional model which is embedded in a moving reference frame, which has a velocity V_{pull}. So we follow the growth of the the crystal as we move along the horizontal coordinate.

In the liquid domain (melt), the transient heat transfer and mass diffusion equations are respectively

$$\frac{\partial T_l}{\partial t} = \alpha_l \frac{\partial^2 T_l}{\partial y^2}, \tag{5.5}$$

$$\frac{\partial C_l}{\partial t} = D_l \frac{\partial^2 C_l}{\partial y^2}, \tag{5.6}$$

where α_l is the thermal diffusivity and D_l is the mass diffusivity of the impurity in the melt.

In the solid domain (silicon film) we assume that solute diffusion is negligible, hence we calculate the the amount of impurities present in the solid using the segregation coefficient obtained from the phase diagram. Thus, the mathematical description for heat and mass transport reads respectively

$$\frac{\partial T_s}{\partial t} = \alpha_s \frac{\partial^2 T_s}{\partial y^2}, \tag{5.7}$$

$$C_s = k_{seg} C_l, \tag{5.8}$$

where α_s is the thermal diffusivity in the solid and k_{seg} is the segregation coefficient.

The conditions at the interface must be such that energy and mass are conserved throughout the system. For the case of energy transport, the heat conducted from

Parameter	Symbol	Value
Ambient temperature (radiation case)	T_{amb}	1084 $[K]$
Top temperature (heat clamp case)	T_{cold}	1684 $[K]$
Melting temperature	T_{melt}	1687 $[K]$
Bottom temperature	T_b	1773 $[K]$
Initial temperature	T_{ini}	1773 $[K]$
Conductivity of solid silicon	k_s	18 $[W\ m^{-1}\ K^{-1}]$
Conductiviy of liquid silicon	k_l	58 $[W\ m^{-1}\ K^{-1}]$
Density of solid silicon	ρ_s	2293 $[kg\ m^{-3}]$
Density of liquid silicon	ρ_l	2570 $[kg\ m^{-3}]$
Heat capacity solid silicon	C_p	1040 $[J\ kg^{-1}\ K^{-1}]$
Thermal diffusivity liquid silicon	α_l	2.33 $\times 10^{-5}[m^2\ s^{-1}]$
Thermal diffusivity solid silicon	α_s	7.54 $\times 10^{-6}[m^2\ s^{-1}]$
Mass diffusivity Al-Si	D_l	7 $\times 10^{-8}[m^2\ s^{-1}]$
Emissivity	ϵ	0.64
Stefan-Boltzmann constant	σ	5.67 $\times 10^{-8}[W\ m^{-2}\ K^4]$
Latent heat of fusion	ΔH	1.79 $\times 10^{6}[J\ kg^{-1}]$
Segregation coefficient Al-Si	k_{seg}	2.83 $\times 10^{-3}$
Capillary constant	Γ	8.99 $\times 10^{-11}[m]$
Slope of the liquidus line	m	-9.5 $\times 10^{-5}[K\ ppm^{-1}]$
Height of the bath	B	0.03 $[m]$

Table 5.2: Material properties and parameters used in the crystallization model.

the liquid bath to the interface and the heat conducted from the film to the surface of the system must balance the heat of crystallization released at the interface. For mass transport, since we assume that no diffusion occurs in the solid, the amount of impurities rejected from the solid to the interface must be equal to the amount of impurities diffusing in the liquid. An additional relation between the thermal and concentration field is required due to the dependency of the melting point of the material on the amount of impurities, a colligative property. This dependency can be found in phase diagrams and accurate information is readily available for several materials, including silicon and its impurities. The mathematical description of the moving boundary conditions at the interface are:

$$\text{Energy Balance:} \qquad \rho_s \Delta H \frac{\partial y}{\partial t} = k_s \frac{\partial T_s}{\partial y} - k_l \frac{\partial T_l}{\partial y}. \tag{5.9}$$

$$\text{Mass Balance:} \qquad -D_l \frac{\partial C_l}{\partial y} = \frac{\partial y}{\partial t}(C_{l_{int}} - C_{s_{int}}). \tag{5.10}$$

$$\text{Melting Point for Binary Mixture:} \qquad T_{int} = T_{melt} + \frac{dT_{liq}}{dC} C_l. \tag{5.11}$$

In these equations, dy/dt represents the velocity of the crystallization front, ΔH is the latent heat of crystallization, ρ_s is the density of the solid phase, k_s and k_l are the thermal conductivities of the solid and the liquid respectively, $C_{l_{int}}$ and $C_{s_{int}}$ are the solute concentration the liquid and solid respectively, the term dT_{liq}/dC is the slope of the liquidus line in a binary phase diagram. In general it is assumed that the slope of the liquidus line does not vary within a specific temperature range, hence it can be assumed that dT_{liq}/dC = constant. Hence, the last expression represents a linear decrease in the melting point as impurities accumulate close to the interface, a phenomenon commonly known as undercooling. At the bottom of the silicon melt, we keep the temperature constant, i.e.

$$T = T_{bottom}. \tag{5.12}$$

With respect to the top boundary condition, we test two cases, first, the so called "heat-clamp" [67] case (active cooling), where we crystallize the ribbon by placing a cold plate at a temperature slightly above the melting point, i.e.

$$T = T_{cold}, \tag{5.13}$$

and radiative (passive) cooling

$$k\frac{\partial T}{\partial y} = \varepsilon\sigma(T^4 - T_{amb}^4). \tag{5.14}$$

These last conditions provide a complete description of the transient energy and mass transport dynamics of the solid-liquid phase system. The equations were discretized using finite differences [43] and solved using MATLAB. The values of the parameters and properties used in the simulation are shown in Table 5.2.

As a case study we use aluminum as the only impurity present in the melt, with a concentration of 50 ppm, which is the usual content in metallurgical grade silicon [17]. Our goal is to find the thermal and concentration profiles resulting from the crystallization of a silicon ribbon of 350 microns in thickness. The height of the silicon bath is assumed to be 3 centimeters.

5.4.1 Crystallization under the heat clamp condition

Figure 5.3 shows the velocity profile as the interface moves from zero to around 350 microns, our desired thickness in this example. Starting crystallization by suddenly cooling the melt surface ($T_{cold} = 1411°C$) makes the interface to initially move fast due to the sharp temperature gradients created in the melt (initially at $1500°C$) and in the first layer of crystal formed. As latent heat starts dissipating from the interface and heat starts flowing from the bottom of the bath (kept at $1500°C$), the difference between temperature gradients at each side of the interface diminishes and the velocity of the interface descreases proportionately. This effect can be seen in Figure 5.4, where we plot the decreasing trend in both temperature gradients as a function of the position of the interface. The values of the temperature gradients are relatively high (compared to the radiative cooling shown in the next section), ranging from 120 K/mm to 10 K/mm in the solid, and 25 K/mm to 5 K/mm in the liquid.

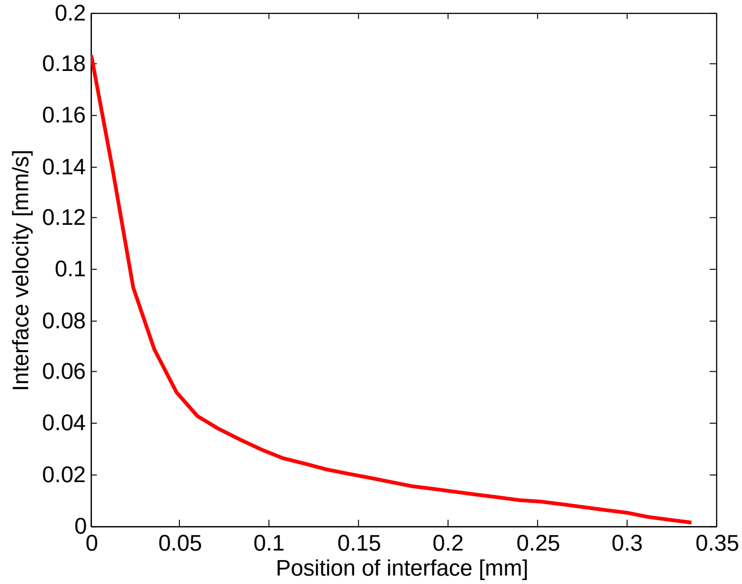

Figure 5.3: The velocity of the interface for the heat clamp boundary condition.

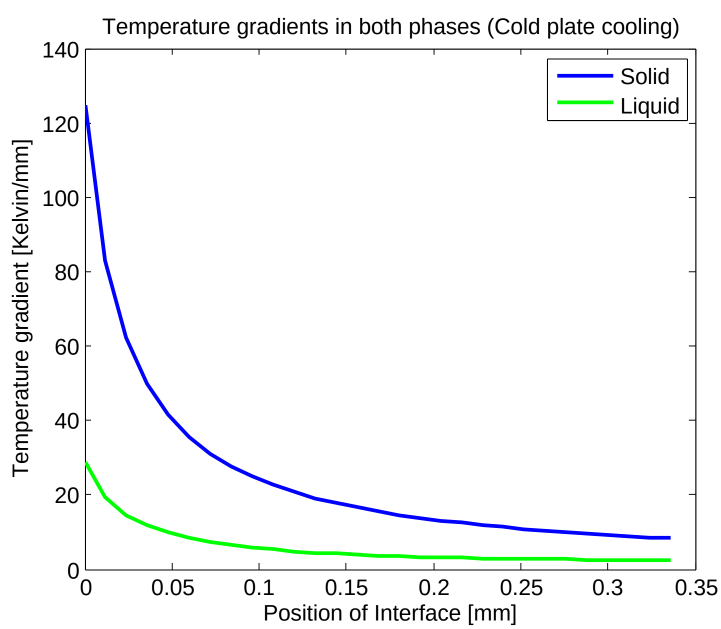

Figure 5.4: The temperature gradients at each phase for the heat clamp boundary condition.

Fast interfacial velocities and steep temperature gradients have a strong impact on the segregation of aluminum in the melt and its distribution across the silicon wafer. Figure 5.5 shows the concentration profile of aluminum in the silicon melt. These concentration profiles are very typical of a classical solidification system under diffusive conditions [55]. It can be seen that the high initial interfacial velocities tend to trap aluminum impurities very close to the interface. A solute enriched boundary layer harboring almost 65 ppm of aluminum is formed at the beginning of crystallization, while keeping the bottom of the bath almost pure. As the interface velocity decreases, the impurities start diffusing throughout the bath, as it can be seen in the final concentration profile of the melt. Nonetheless, most of the aluminum remains concentrated in only the top fifth of the bath height. In the HRG process, this could become a problem, since more impurities will be present next to the interface as more of the ribbon crystallizes. In a continuous operation, one would expect a non-homogeneous impurity distribution across the length of the silicon ribbon.

The decrease in impurity concentration and the "broadening" of the boundary layer as crystallization proceeds, generates a nonhomegenous impurity distribution across the silicon wafer as well. Figure 5.6 shows the aluminum distribution in resulting silicon film. The concentration at each point of the wafer is proportional to the concentration of aluminum in the liquid immediately below the solid-liquid interface, and thus also proportional to the length of the boundary layer. However, even under this rather "aggressive" crystallization conditions, it is still possible to obtain a 50-fold reduction in the impurities present across the ribbon. This suggests that the rejection of aluminum -coming from metallurgical grade silicon- can be effectively performed by the proposed crystallization process under heat-clamp thermal conditions. The maximum amount of impurities allowed in solar-grade silicon is less that 2 ppm, which is much more than the maximum concentration found in our simulated wafer.

Finally, Figure 5.7 shows the resulting shapes of the ribbon using the Lagrangian

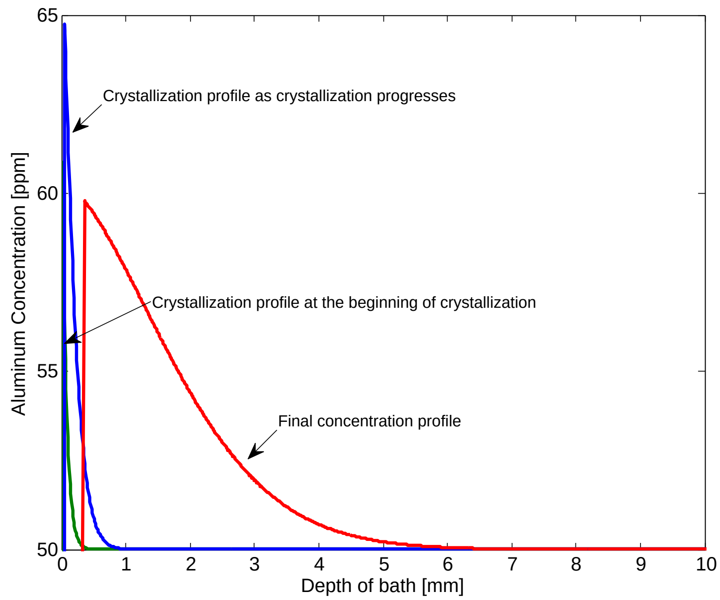

Figure 5.5: Impurity concentration profiles in the melt at different stages of the crystallization process. Vertical lines represent the position of the interface.

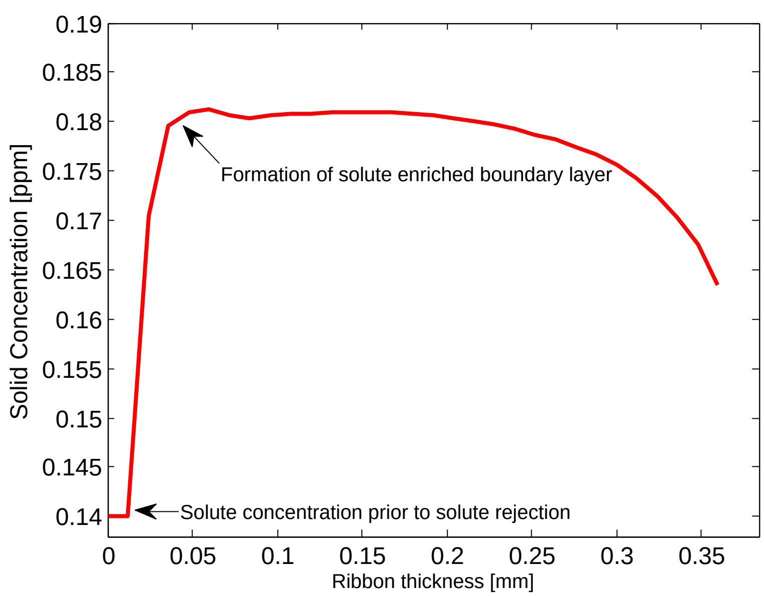

Figure 5.6: Distribution of aluminum in the wafer for the heat-clamp case.

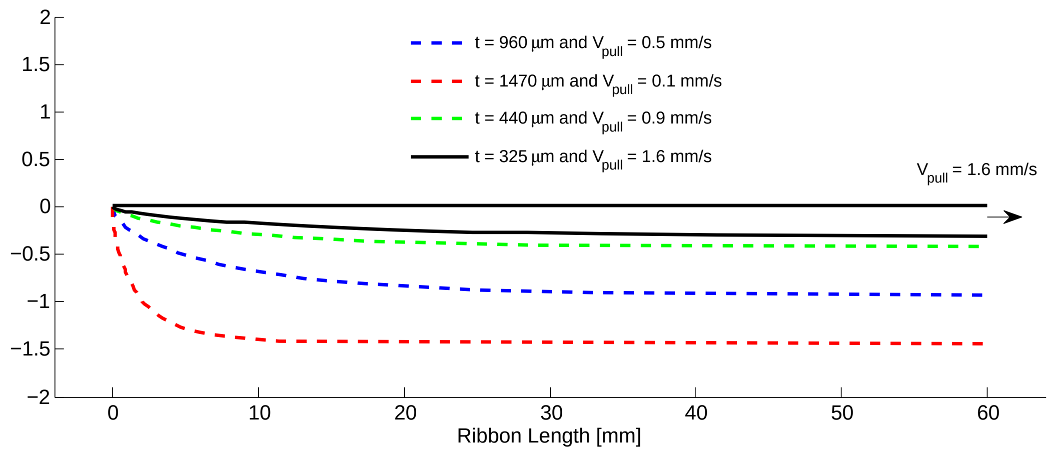

Figure 5.7: The shape of the ribbon for different pulling velocities.

approach. We plot the shape of the wedge for four different thickness values, 325 μm, 440 μm, 960 μm and 1470 μm. The profiles were obtained assuming that the length of the cooling plates is 6 centimeters. The shape of the wedge exhibits a parabolic profile, which is the same result that Zoutendyk found in his theoretical calculations [67] on the heat-clamp case, as shown qualitatively in Figure 5.8. In his theoretical model, he found the characteristic shape of the wedge by neglecting the effect of the liquid temperature gradient adjacent to the interface ($\partial T_l/\partial y = 0$). We show that the parabolic profile is preserved when accounting for this term as well. The thickness of the wafer decreases as the pulling speed increase, as it is expected.

5.4.2 Crystallization under radiative cooling

Figure 5.9 shows the evolution of the temperature profiles in the melt and the silicon ribbon for the case when the surface is being cooled via radiation. The slope discontinuity represents the interface. The linear profiles are explained by the slow dynamics of the crystallization process. Cooling due to radiation is slow compared to the heat-clamp cooling, hence any change in the thermal and solutal fields on the surface of the system or close to the crystallization front is reflected in a "diffusion

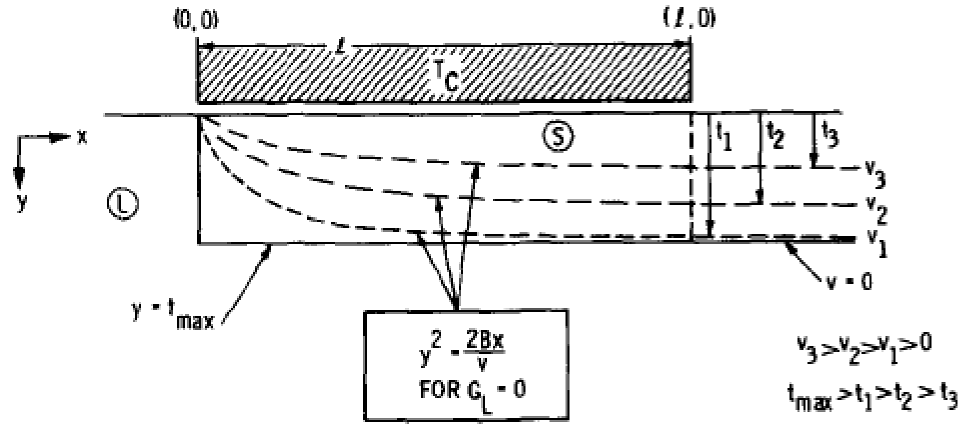

Figure 5.8: Zoutendyk's [67] theoretical prediction of the shape of the wedge.

time" away from the interface.

The shallow thermal gradients close to the interface are reflected in low velocities of the crystallization front, resulting in a high quality wafer. The results in Figure 5.10 show that the temperature gradients are approximately 9.36 K/mm towards the solid and 2.9 K/mm towards the liquid, respectively. The conductivity of the solid silicon film is approximately three times lower than the conductivity of molten silicon and it follows that the magnitude of the gradient in the solid domain is about three times higher than the liquid. In his experimental analysis, Kudo suggested that a temperature gradient of 2 K/mm is present in the liquid phase [33]. This corresponds well with our results and shows that simple models of the type above can provide accurate results at the conceptual design stage for this process.

Figure 5.11 shows the concentration profile of aluminum in molten silicon close to the crystallization front. The velocity of the crystallization front is shown in Figure 5.12. As the velocity of the crystallization front decreases ($dy/dt \approx 0$) the length of the solute enriched boundary layer increases and the concentration profile "flattens".

Figure 5.13 shows the solute distribution across the thin film. We see that the

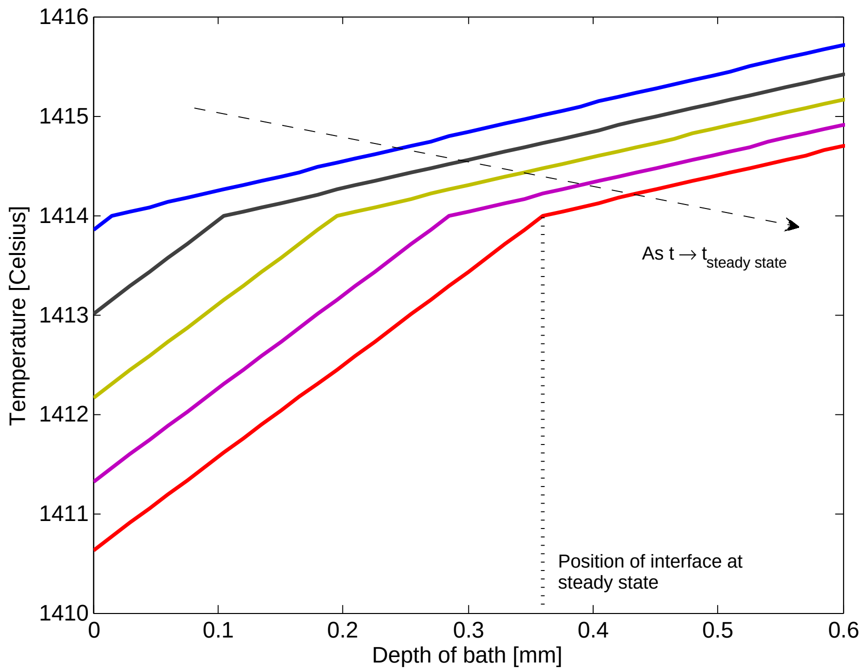

Figure 5.9: Evolution of the temperature profile in both phases close to the crystallization front.

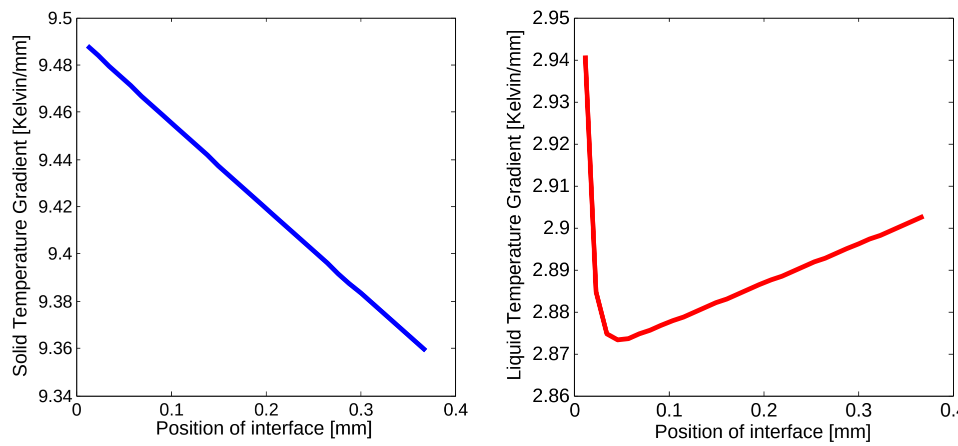

Figure 5.10: Evolution of the temperature gradient in both phases.

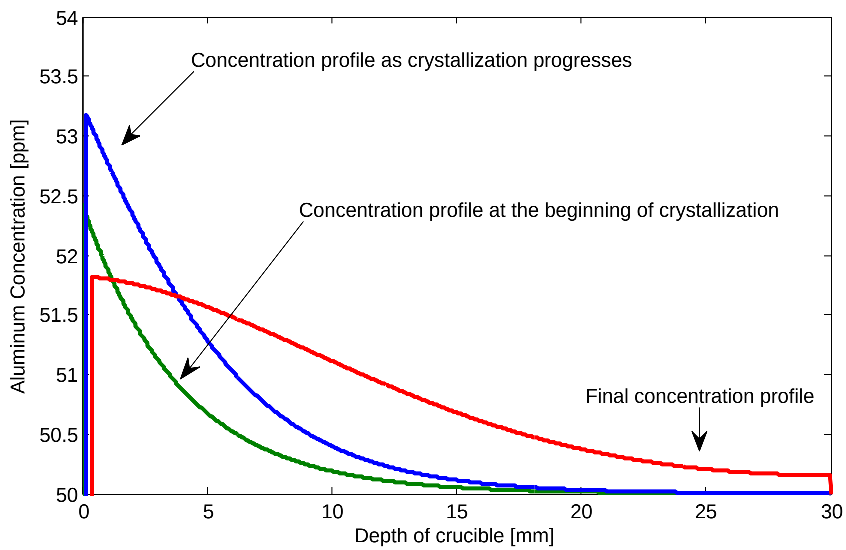

Figure 5.11: Impurity concentration profiles at different stages of the crystallization process. Vertical lines represent the position of the interface.

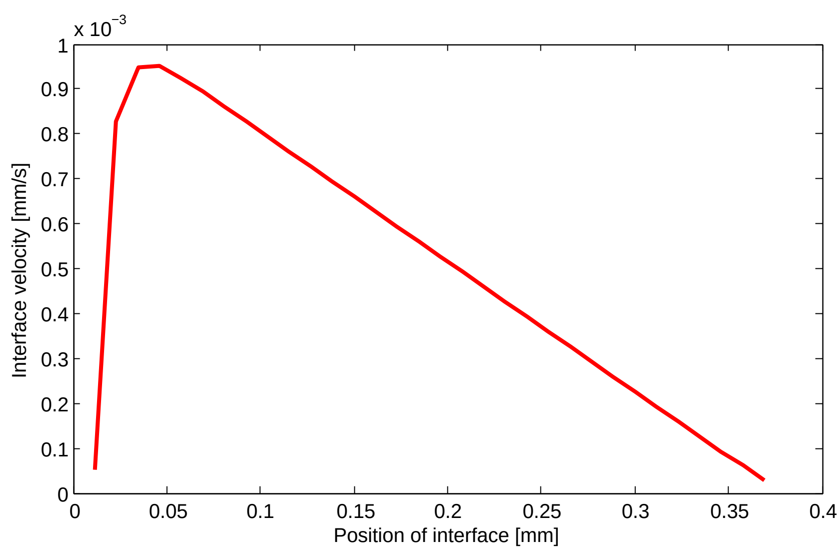

Figure 5.12: The velocity of the interface for the case of radiative cooling.

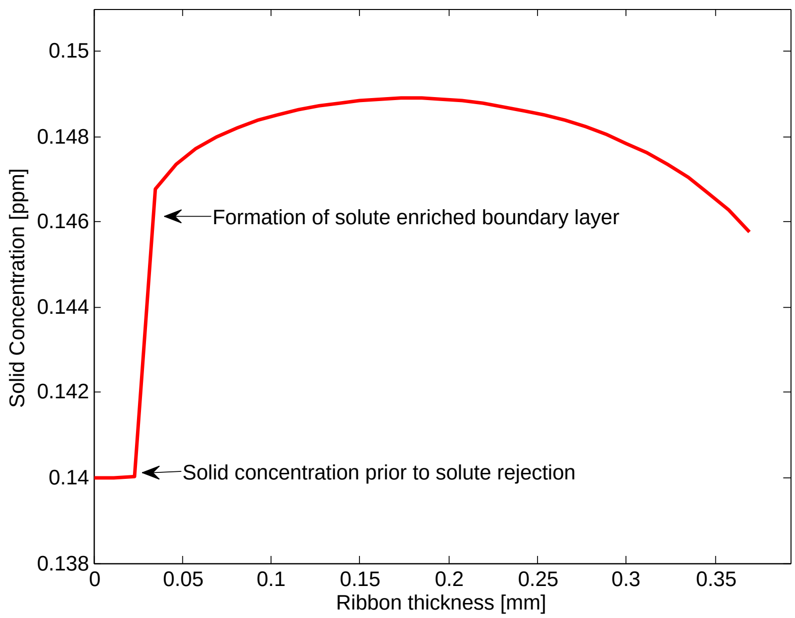

Figure 5.13: Final impurity concentration across the silicon film.

film contains much less than 1 ppm aluminum impurity. This is due to the low crystallization velocities in the system which allows a homogeneous distribution of aluminum in the melt. This contrasts with the case when the melt is subject to a heat-clamp type of cooling, where most of the impurities remain close to the solid-liquid interface.

Several important design implications follow: first, impurity levels of 50 ppm or (or slightly higher) for elements with segregation coefficient higher than aluminum are tolerated. Second, as we see in the next section, the morphological stability of the system is guaranteed. Finally, solute buildup in the melt can be calculated as well as the maximum concentration of impurities that the wafer can withhold without trespassing the quality requirements for the manufacturing of the solar cell. Once the system reaches a saturation limit, the system can be purged and replenished with fresh melt.

5.5 Transient Mullins-Sekerka stability analysis for the heat clamp case

In this section, we formulate the problem of interface stability of the crystallization system, using a Mullins-Sekerka-type analysis. We extend the classical formulation to account for the time dependency of the system, the non-constant interface velocity and the finite nature of the domain. A few extensions of this kind have been reported in the literature. In the work of Coriell and co-workers [14], they compare the classical stability criterion with an extented model that accounted for the initial transient, while assuming a constant interface velocity. They found a similar trend between both models, but observed that the transient constant-velocity system is slightly more stable that the classical approach. They attributed this to the fact that the time dependent model accounts for past concentration gradients in the system, which tend to be lower for a constant interface velocity, and therefore more stable. Greven and collaborators [24] built a rapid solidification model of a Si-Sn alloy, and compared the results with experimental data. They also performed a stability analysis, similar to that of Coriell [14], and observed that in some experiments, the interfacial breakdown occured at the initial transient.

In the previous two models, it is assumed that the interface velocity, dI/dt, of the interface remains constant. In our model, as we showed in the previous section, the velocity of the interface varies as the crystal is growing (the initial transient). We account for this variable in the formulation of our stability problem.

Considering small perturbations, we state the temperature and concentration profiles as the superposition of a base state and a Fourier-perturbed state as follows:

$$T_l(y,t) = T_l(y,t)^{base} + T_l(y,t)^{pert} sin(\omega x) \tag{5.15}$$

$$T_s(y,t) = T_s(y,t)^{base} + T_s(y,t)^{pert} sin(\omega x) \tag{5.16}$$

$$C_l(y,t) = C_l(y,t)^{base} + C_l(y,t)^{pert} sin(\omega x) \tag{5.17}$$

$$h(t) = y(t) + \delta(t) sin(\omega x) \tag{5.18}$$

The unperturbed and perturbed modes are independent from each other in both subdomains (solid and liquid) due to the linearity of the diffusion equations. The only coupling occurs at the solid-liquid interface, where the perturbation is applied. The perturbed interfacial conditions are found by equating the perturbed coefficients up to the first order that result from a Taylor series expansion around δ:

$$\begin{aligned} T_l(y,t) &= T_l(y,t)^{base} + \left(T_l(y,t)^{pert} + \delta(t)\frac{\partial T_l(y,t)^{base}}{\partial y}\right) sin(\omega x), && (5.19)\\ T_s(y,t) &= T_s(y,t)^{base} + \left(T_s(y,t)^{pert} + \delta(t)\frac{\partial T_s(y,t)^{base}}{\partial y}\right) sin(\omega x), && (5.20)\\ C_l(y,t) &= C_l(y,t)^{base} + \left(C_l(y,t)^{pert} + \delta(t)\frac{\partial C_l(y,t)^{base}}{\partial y}\right) sin(\omega x), && (5.21)\\ \frac{dh(t)}{dt} &= \frac{dy(t)}{dt} + \frac{d\delta(t)}{dt} sin(\omega x). && (5.22) \end{aligned}$$

where in the last expression we take the time derivative of the position function. Equating coefficents of Fourier modes, yield the following perturbed interfacial conditions

$$\rho\Delta H \left(\frac{d\delta}{dt}\right) = k_s\left(\frac{\partial T_s^{pert}}{\partial z} + \delta\frac{\partial^2 T_s^{base}}{\partial z^2}\right) - k_l\left(\frac{\partial T_l^{pert}}{\partial z} + \delta\frac{\partial^2 T_l^{base}}{\partial z^2}\right), \tag{5.23}$$

$$-D\left(\frac{\partial C_l^{pert}}{\partial z} + \delta\frac{\partial^2 C_l^{base}}{\partial z^2}\right) = \frac{dy}{dt}(1-k)\left(C_l^{pert} + \delta\frac{\partial C_l^{base}}{\partial y}\right) + \frac{d\delta}{dt}(1-k)C_l^{base} \tag{5.24}$$

$$T_l^{pert} + \delta\frac{\partial T_l^{base}}{\partial z} = T_s^{pert} + \delta\frac{T_s{}^{base}}{\partial z}, \tag{5.25}$$

$$T_l^{pert} + \delta\frac{\partial T_l^{base}}{\partial z} = \frac{dT_{liq}}{dC}\left(C_l^{pert} + \delta\frac{\partial C_l^{base}}{\partial z} - T_{melt}\Gamma\omega^2\delta\right). \tag{5.26}$$

The boundary conditions are such that the perturbed fields vanish at the boundaries.

This system of four linear equations provide the solution for the evolution for the four perturbed fields T_l^{pert},T_s^{pert},C_l^{pert} and δ. In practical applications, the value of the angular frequency, ω, must be such that the wavelength of the perturbation is much more smaller than the characteristic length of the system, i.e

$$\frac{D_{Al}}{V} \gg \frac{2\pi}{\omega}. \tag{5.27}$$

Figure 5.14 shows the perturbation δ as a function of the position of the interface, for both the numerical case and the classical case. To better show the

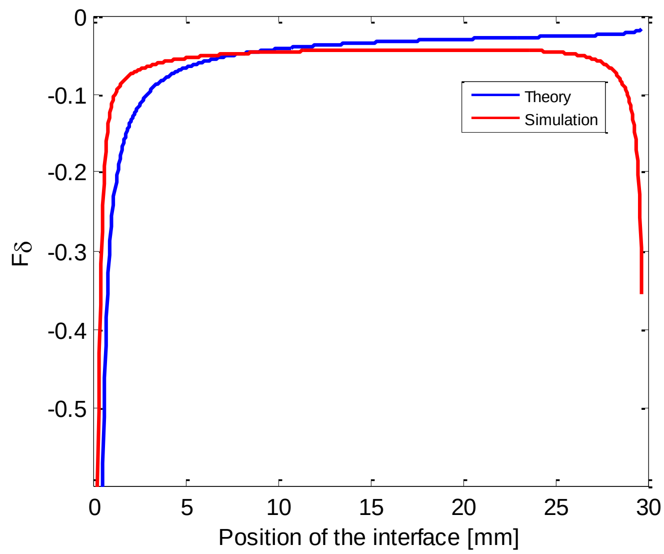

Figure 5.14: Transient Mullins-Sekerka perturbation function versus the classical Mullins-Sekerka criterion.

difference between the two cases, we crystallize the whole system (we keep in mind that our region of interest is the region where the depth of the bath is less than 0.5 milimeters).

In the classical case, we apply the stability criterion (equation (5.2)) at each time step, using the instantaneous values of the temperature and concentration gradients. We see that for the proposed amount of impurities, the interface remains stable in both cases. Nonetheless, we see that, with the modified Mullins-Sekerka formulation, the stability function is higher and the initial transient, since the interface velocity is higher (so more solute is trapped close to the front). Also, the perturbation tends to decrease rapidly as the the interface reaches the bottom of the bath (where the velocity of the front tends to zero).

5.6 Conclusions and contributions

In this chapter, we assessed the problem of stability of the interface in the HRG process. We constructed a crystallization model to show that a 50 fold improvement can be expected in the final wafer purity when there are aluminum impurities present in the feed. Thus the process can reduce 50 ppm aluminum impurities to 1 ppm or less.

The Mullins-Sekerka theory shows that the flat interface is stable for the proposed operating conditions. Interfacial breakdown does not occur for large amount of impurities. The calculations show that continuous solutal build-up in the system is not a serious concern in insuring a morphologically stable front in the HRG process. The instabilities observed as dendritic growth in the Kudo study are likely to be due to impurity levels higher than 50 ppm or other factors leading to sharp gradients near the interface. Such factors include mechanical perturbations/vibrations in the system, very high cooling levels when pulling at high velocities, and Marangoni and buoyant currents in the melt.

The findings in this chapter can serve as a starting point for future experimental validation of the HRG process, model refinement, control and optimization. One major problem that eludes solution at this point is how to remove a uniform thin sheet from the melt in a continuous manner.

Chapter 6

Conclusions and Future Work

6.1 Conclusions

In this thesis, we assessed three of the main technical challenges of the Horizontal Ribbon Growth process for manufacturing silicon wafers. Namely, the problem of the melt spilling over the crucible, the problem of the ribbon crystallizing onto the surface of the crucible, and the problem of dendritic growth.

In order to solve the first two problems, we relied on the the first law of thermodynamics and the tools of variational calculus, to find the conditions of existence and stability of the meniscus located between the ribbon and the surface of the crucible. The shape and existence conditions of the feasible meniscii are found by solving the Euler-Lagrange equation, derived from the vanishing of the first variation of the energy functional. This equation yields the governing Young-Laplace equation of the HRG system, which we solve analytically in terms of a single-valued function $X(Y)$. The stability of the feasible meniscii is calculated by finding the conditions under which the second variation of the energy functional is positive. We found that all the single-valued functions describing the shape of feasible meniscii are statically stable.

The question of whether there existed additional meniscii that were statically unstable, was answered using Weierstrass's parametric approach to the variational problem. With this approach, we found parametric solutions to the governing Young-Laplace equation, which broadened the solution space of the original problem. The new curves that we can capture with the solution correspond to values of contact angle below zero, which we proved to be statically unstable. The shapes of the unstable meniscii are in good qualitative agreement with a simple proof-of-concept experiment, where we mimicked the process of meniscus detachment and melt-spill over.

We also found a solution to a type of Young-Laplace equation of the form $H - Y = (X'Y'' - X''Y')/(X'^2 + Y'^2)^{3/2}$. To the best of the author's knowledge, this analytical solution has not been reported in the literature, and constitutes one of the contributions of this thesis.

To solve the problem of dendritic growth, we developed a crystallization model incorporating an extended form of the classical Mullins-Sekerka analysis. The mathematical model is used to described the evolution of the thermal profile in the melt and the ribbon, as well as the segregation of solute in the melt. As an illustrative example, we use a silicon system with 50 ppm of aluminum present in the melt. We show that for the proposed crystallization velocities, it is possible to achieve a stable crystallization front and the purification of the ribbon.

6.2 Future work

Several issues remain to be addressed in the study of the HRG process. In the context of the developments and findings of this work, the effects of capillarity next to the triple phase of the system (melt top surface-ribbon-gas) would be a natural next step in the analysis. The tools that we developed in Chapters 3 and 4 can be directly applied to this section of the system. As of now, it is assumed that the top surface of the melt remains flat, but we conjecture that this is not the case given the non-zero contact angle between the ribbon and the melt.

The coupling of interfacial and thermal phenomena could be another step to take in the HRG analysis. It is well known that the surface tension of silicon is highly dependant on temperature; this dependency gives rise to surface-tension driven flows, commonly known as Marangoni convection, which affects the thermal profile at the interface, and also alter the shape of the free surfaces of the system, including the lower meniscus. A potential line of research could be developed by formulating a theoretical model (or set of models) describing the interaction between these two phenomena in the HRG process. Since the nature of the mathematical problem is expected to be complex, we suggest the use of asymptotic/analytical techniques to study the interaction between the thermal field and the evolution of the free surfaces. The computational calculations of Marangoni convection that have been reported in the HRG literature [44, 45] could be used to validate the approximations of the theoretical model. From the computational observations, we would expect a more restricting stability criterion for the pinning of the meniscus to the corner of the crucible, since Marangoni currents can be viewed as an additional disturbance at the free surface.

Another possible direction of this project is the analysis of heat transport in the silicon ribbon, in order to obtain a more accurate theoretical relationship between the thickness and the pulling speed of the ribbon. The building block for this idea is the analysis by Zoutendyk [67]. In his theoretical model, Zoutendyk neglected the effects of convection, the heat removed due to ribbon pulling, and the transient effects. From these three assumptions, accounting for the heat removal due to the pulling seems to be the less challenging improvement that could be made to the model. Mathematically this would be done by adding the additional convective term to the energy equation. Zoutendyk's analysis is limited to low pulling speeds, which might be inaccurate for future technical advances, where large pulling speeds can be accomplished. The laboratory experiments currently being realized at CMU with ice and water could help in testing the validity of an improved theoretical expression.

The development of improved theoretical approximations describing the physics of the HRG process would serve as the basis of two research activities: the design of theory-based experiments and the computational implementation of control strategies. The theoretical models could be used to find sets of optimal configurations and operating guidelines prior to experimenting. These include: the optimal length of the ribbon resting on the melt (which determines the length of the cooling plates), the most favorable pulling angles, the lower and upper limits of the melt level, the amount of heat that needs to be removed from the surface of the melt, the optimal melt temperature profile that minimizes Marangoni convection, et cetera. With regards to potential control strategies, we would be interested in testing the ability of a controller to maintain the thickness of the ribbon constant when the system is subject to disturbances in the cooling profile and the pulling velocity.

All these previous tasks concern mostly the macroscopic scale of the crystallization system. Looking at the smaller length and time scales of the HRG process, there are many issues that were not addressed in this work. Mainly, the effect of momentum, mass and heat transport in the microscopic structure of the silicon crystal. The question to answer would be, how does transport variables affect the arrangement of the atoms along the crystal? Two approaches to "micromodel" the crystallization processes could be used to solve this issue [55]: the deterministic and the stochastic. In the first approach we would solve the continuity and conservation equations coupled with the nucleation and growth kinetics model [64]. In the second, we would use physics-based rules describing dendritic growth kinetics along with "randomization" of the attachment location of the atoms. Among these techniques are the cellular automata and Monte Carlo methods [47].

Appendix A

Method for solving the governing Young-Laplace equation in the HRG process

We begin the mathematical treatment with equation (3.49)

$$\frac{dY}{dX} = \frac{\sqrt{1 - \left(\frac{Y^2}{2} \mp H_{12}Y + \cos\theta\right)^2}}{\frac{Y^2}{2} \mp H_{12}Y + \cos\theta}. \tag{A.1}$$

1. *Invert ODE and factorize the characteristic polynomial:*

$$\frac{dX}{dY} = \frac{\frac{1}{2}\left[(Y \mp H_{12})^2 + A\right]}{\sqrt{1 - \frac{1}{4}\left[(Y \mp H_{12})^2 + A\right]^2}}, \tag{A.2}$$

where

$$A = 2\cos(\sigma + \beta) - \left(\frac{\rho_s}{\rho_l}T - L\sin\beta\right)^2. \tag{A.3}$$

2. *Split and factorize the square root of the denominator:*

$$\frac{dX}{dY} = \frac{(Y \mp H_{12})^2 + A}{\sqrt{2-A}\sqrt{2+A}\sqrt{1 - \left(\frac{Y \mp H_{12}}{\sqrt{2-A}}\right)^2}\sqrt{1 - \left(\frac{Y \mp H_{12}}{\sqrt{-2-A}}\right)^2}}. \tag{A.4}$$

3. Perform a change of variables:

$$r = \frac{Y \mp H_{12}}{\sqrt{2-A}}, \tag{A.5}$$

$$dr = \frac{dY}{\sqrt{2-A}}. \tag{A.6}$$

The ODE becomes:

$$\frac{dX}{dr} = \frac{(2-A)r^2 + A}{\sqrt{2+A}\sqrt{1-r^2}\sqrt{1-\kappa^2 r^2}}, \tag{A.7}$$

with

$$\kappa^2 = \frac{A-2}{A+2}. \tag{A.8}$$

4. Expand right hand side in partial fractions:

$$\begin{aligned}\frac{dX}{dr} = \frac{2-A}{\sqrt{2+A}}\left(\frac{1}{\kappa^2\sqrt{1-r^2}\sqrt{1-\kappa^2 r^2}} - \frac{\sqrt{1-\kappa^2 r^2}}{\kappa^2\sqrt{1-r^2}}\right)& \\ + \frac{A}{\sqrt{2+A}\sqrt{1-r^2}\sqrt{1-\kappa^2 r^2}}&.\end{aligned} \tag{A.9}$$

5. Group similar terms:

$$\frac{dX}{dr} = \sqrt{2+A}\left(\frac{\sqrt{1-\kappa^2 r^2}}{\sqrt{1-r^2}}\right) - \frac{2}{\sqrt{2+A}}\left(\frac{1}{\sqrt{1-r^2}\sqrt{1-\kappa^2 r^2}}\right). \tag{A.10}$$

6. Integrals of terms in parentheses are the elliptic integrals of the first and second kind respectively. We integrate and change the variables back to Y to obtain the analytical solution:

$$X(Y) = X_c + \sqrt{A+2}[\mathbf{E}(\Psi_Y,\kappa) - \mathbf{E}(\Psi_0,\kappa)] - \frac{2}{\sqrt{A+2}}[\mathbf{F}(\Psi_Y,\kappa) - \mathbf{F}(\Psi_0,\kappa)]. \tag{A.11}$$

where $\mathbf{F}(\Theta,\kappa)$ and $\mathbf{E}(\Theta,\kappa)$ are the incomplete elliptic integrals of the first and second kind respectively and,

$$\Psi_Y = \arcsin\left(\frac{Y \mp \sqrt{2\cos\theta - A}}{\sqrt{2-A}}\right), \tag{A.12}$$

$$\Psi_0 = \arcsin\left(\mp\sqrt{\frac{2\cos\theta - A}{2-A}}\right). \tag{A.13}$$

Appendix B

Analyzing meniscus existence in the HRG process in Cartesian form

Starting from expression (3.57), the solution branch corresponding to $f(Y)_+$ requires that

$$\min\left(\frac{Y^2}{2} + H_{12}Y + \cos\theta\right) > -1, \tag{B.1}$$

$$\max\left(\frac{Y^2}{2} + H_{12}Y + \cos\theta\right) < 1. \tag{B.2}$$

The critical point of the function $f(Y)_+$ is located at $Y = -H_{12}$, which is always negative number for real valued meniscii, and thus located outside of the physical domain of Y. We thus have that the function $f(Y)_+$ is a monotonic function in the $[0, H_{1-}]$ interval. In this case is monotonically increasing, so we have

$$\min f(Y)_+ = f(0) = \cos\theta, \tag{B.3}$$

$$\max f(Y)_+ = f(H_{1-}) = \cos(\sigma + \beta). \tag{B.4}$$

Therefore we require

$$\theta > \sigma + \beta. \tag{B.5}$$

Besides this condition, we require the existence of positive real values of the equilibrium height H_{1_-}. In other words, equation (3.46) must hold, and, from (3.47), we see that in order to obtain positive values for H_{1_-} we require the pulling angle to be above a critical value,

$$\beta > \arcsin\left(\frac{\rho_s T}{\rho_l L}\right). \tag{B.6}$$

Using the same procedure, the solution branch corresponding to $f(Y)_-$ has to satisfy

$$\min\left(\frac{Y^2}{2} - H_{12}Y + \cos\theta\right) \geq -1, \tag{B.7}$$

$$\max\left(\frac{Y^2}{2} - H_{12}Y + \cos\theta\right) \leq 1. \tag{B.8}$$

The critical point of the function in parenthesis is located at $Y = H_{12}$, which is a minimum. So we have that

$$\min f(Y)_- = f(H_{12}) \geq -1. \tag{B.9}$$

which gives

$$1 + \cos(\sigma + \beta) \geq \frac{1}{2}\left(\frac{\rho_s}{\rho_l}T - L\sin\beta\right)^2. \tag{B.10}$$

The maximum is then located at either $f_-(0) = \cos\theta$ or at $f_-(H_{1_+}) = \cos(\sigma + \beta)$, whose values always lie within the [-1,1] interval. If $\max f(Y)_- = \cos\theta$, it implies

$$\theta < \sigma + \beta, \tag{B.11}$$

and from (3.47), we see that H_{1_+} is always positive under these conditions. However if $\max f(Y)_- = \cos(\sigma + \beta)$, then we have that

$$\theta > \sigma + \beta \tag{B.12}$$

and from (3.47), we require that

$$\beta > \arcsin\left(\frac{\rho_s T}{\rho_l L}\right), \tag{B.13}$$

in order to obtain positive values of the equilibrium height.

Appendix C

Method to solve the governing Young-Laplace equation in the HRG process in parametric form

Dividing equation (4.46) by (4.43) yields

$$\frac{d\Omega}{dY} = \frac{H_1 - L\sin\beta - Y + \frac{\rho_s}{\rho_l}T}{\sin\Omega}. \tag{C.1}$$

In the previous chapter we showed that separating variables in this equation and integrating Y from 0 to H_1, and Ω from θ to $\sigma + \beta$, and then solving for H_1, we obtain

$$H_{1_\pm} = L\sin\beta - \frac{\rho_s}{\rho_l}T \pm \sqrt{\left(\frac{\rho_s}{\rho_l}T - L\sin\beta\right)^2 + 2\cos\theta - 2\cos(\sigma+\beta)} = H_{11} \pm H_{12}. \tag{C.2}$$

We also showed that integrating the differential equation from the lower limits ($Y = 0$ and $\Omega = \theta$) to an arbitrary set of values Y and Ω, we solved for the angle Ω in terms of Y

$$\Omega(Y) = \arccos\left(\frac{Y^2}{2} \mp H_{12}Y + \cos\theta\right). \tag{C.3}$$

Plugging this value in equation (4.43) yields the following ODE:

$$\frac{dY}{dS} = \sqrt{1 - \left(\frac{Y^2}{2} \mp H_{12}Y + \cos\theta\right)^2}, \tag{C.4}$$

We separate variables and factorize the polynomial inside the parenthesis to obtain,

$$\frac{2dY}{\sqrt{2-A}\sqrt{2+A}\sqrt{1 - \frac{(Y \mp H_{12})^2}{2-A}}\sqrt{1 + \frac{(Y \mp H_{12})^2}{2+A}}} = dS, \tag{C.5}$$

where,

$$A = 2\cos(\sigma + \beta) - \left(\frac{\rho_s}{\rho_l}T - L\sin\beta\right)^2. \tag{C.6}$$

Using the substitution,

$$r = \frac{Y \mp H_{12}}{\sqrt{2-A}}, \qquad dr = \frac{dY}{\sqrt{2-A}}, \tag{C.7}$$

transforms the differential equation into

$$\frac{2dr}{\sqrt{2+A}\sqrt{1-r^2}\sqrt{1-\kappa^2 r^2}} = dS, \tag{C.8}$$

where

$$\kappa = \frac{A-2}{A+2}. \tag{C.9}$$

Integrating the left hand side from $r(Y=0)$ to an arbitrary r, the right hand side from $S = 0$ to an arbitrary S, and changing back to the variable Y, we obtain

$$S(Y) = \frac{2}{\sqrt{2+A}}\left[\mathbf{F}\left(\arcsin\left(\frac{Y \mp H_{12}}{\sqrt{2-A}}\right)\middle|\kappa\right) - \mathbf{F}\left(\arcsin\left(\frac{\mp H_{12}}{\sqrt{2-A}}\right)\middle|\kappa\right)\right]. \tag{C.10}$$

In this expression $\mathbf{F}(\Omega|\kappa)$ is the incomplete elliptic integral of the first kind. In order to find an expression for $Y(S)$, we use the inverse of $\mathbf{F}(\Omega|\kappa)$, given by the Jacobi amplitude

$$\mathbf{F}^{-1}(\Theta|\kappa) = \mathbf{am}(\Theta|\kappa), \tag{C.11}$$

so we get,

$$\arcsin\left(\frac{Y \mp H_{12}}{\sqrt{2-A}}\right) = \mathbf{am}\left[\frac{\sqrt{2+A}}{2}S + \mathbf{F}\left(\arcsin\left(\frac{\mp H_{12}}{\sqrt{2-A}}\right)\middle|\kappa\right)\middle|\kappa\right]. \tag{C.12}$$

Solving for Y and using the property

$$\sin(\mathbf{am}(\Theta|\kappa)) = \mathbf{sn}(\Theta|\kappa), \tag{C.13}$$

yields equation (4.50).

The expression for $Y(S)$ is used to solve for $X(S)$ in the following way:

$$\frac{dX}{dS} = \cos\Omega = \frac{Y^2}{2} \mp H_{12}Y + \cos\theta = \frac{A}{2} + \frac{2-A}{2}\,\mathbf{sn}\left(\frac{\sqrt{2+A}}{2}S + \mathbf{F}(\Psi_0|\kappa)\middle|\kappa\right)^2. \tag{C.14}$$

We separate variables and use the following property:

$$\int \mathbf{sn}(\Theta|\kappa)^2 d\Theta = \frac{\Theta}{\kappa} - \frac{\mathbf{E}(\mathbf{am}(\Theta|\kappa)|\kappa)\sqrt{1-\kappa\mathbf{sn}(\Theta|\kappa)^2}}{\kappa\,\mathbf{dn}(\Theta|\kappa)} + C, \tag{C.15}$$

to get expression (4.54).

Lastly, we solve for $\Omega(S)$. With the aid of equation (3.45) we put equation (4.46) in the following form:

$$\frac{d\Omega}{dS} = \pm H_{12} - Y. \tag{C.16}$$

An expression for $Y(\Omega)$ is derived using expression (3.48) and plugged into the above ODE to get:

$$\frac{d\Omega}{dS} = \mp\sqrt{2\cos\Omega - A}. \tag{C.17}$$

Using simple manipulation and trigonometric properties we transform the right hand side of the ODE:

$$\frac{d\Omega}{dS} = \mp\sqrt{2-A}\sqrt{1 - \frac{4}{2-A}\sin^2\left(\frac{\Omega}{2}\right)}. \tag{C.18}$$

Separating variables and integrating yields equation (4.56).

The test case we use to compare and validate the analytical solution with the numerical simulationis that corresponding to $\beta = 10°$ and $\theta = -63°$. The shape of the corresponding meniscus is shown in figure 4.2. We compare the analytical solution values of $X(S)$, $Y(S)$ and $\Omega(S)$ with the computer simulation values. Both calculations are carried in Mathematica. The input script is shown in figure C.1 and the output is shown in figure C.2. The analytical solution matches perfectly the numerical simulation.

```
In[1183]:= ClearAll["Global`*"]
Off[General::spell1];
Off[General::spell];
rhol = 2570;
rhos = 2293;
g = 9.8;
gamma = 0.72;
a = Sqrt[gamma / (rhol * g)];
t = 400 * 10 ^ -6;
l = 6 * 10 ^ -2;
T = t / a;
L = l / a;
sigma = 11 * Pi / 180;
thetadeg = -63;
limsup = 5.78;
theta = thetadeg * Pi / 180;
beta = 10 * Pi / 180;
H1pos == L * Sin[beta] - (rhos * T / rhol) +
   Sqrt[ ( (rhos * T / rhol) - L * Sin[beta]) ^2 - 2 * Cos[sigma + beta] + 2 * Cos[theta] ];
H1neg = -L * Sin[beta] - (rhos * T / rhol) +
   Sqrt[ ( (rhos * T / rhol) - L * Sin[beta]) ^2 - 2 * Cos[sigma + beta] + 2 * Cos[theta] ];
H12 = Sqrt[ ( (rhos * T / rhol) - L * Sin[beta]) ^2 - 2 * Cos[sigma + beta] + 2 * Cos[theta] ];
psiode = -H12;
A = 2 * Cos[theta] - H12 ^ 2;
ksq = (A - 2) / (A + 2);
phizero = ArcSin[H12 / Sqrt[2 - A]];
parametricsystem :=
  {x '[s] == Cos[z[s]], y '[s] == Sin[z[s]], z '[s] == -psiode - y[s], x[0] == 0, y[0] == 0, z[0] == theta};
NDSolve[parametricsystem, {x, y, z}, {s, 0, limsup}];
{xans[s_], yans[s_], zans[s_]} =
  {x[s], y[s], z[s]} /. Flatten[NDSolve[parametricsystem,  {x[s], y[s], z[s]}, {s, 0, limsup}]];
graphx = Plot[xans[s], {s, 0, limsup}, PlotStyle → {Blue, Dashed, Thick},
  PlotLabel → "Numerical solution of X(S)", AxesLabel → {S, X[S]}, PlotLegends → {"Numerical"}]
graphy = Plot[yans[s], {s, 0, limsup}, PlotStyle → {Blue, Dashed, Thick},
  PlotLabel → "Numerical solution of Y(S)", AxesLabel → {S, Y[S]}, PlotLegends → {"Numerical"}]
grapho = Plot[zans[s], {s, 0, limsup}, PlotStyle → {Blue, Dashed, Thick},
  PlotLabel → "Numerical solution of Ω(S)", PlotLegends → {"Numerical"}, AxesLabel → {S, Ω[S]}]
graphxan = Plot[-s + Sqrt[A + 2] *
    {(EllipticE[JacobiAmplitude[(Sqrt[2 + A] * s / 2) + EllipticF[phizero, ksq], ksq], ksq] *
        Sqrt[1 - ksq * JacobiSN[(Sqrt[2 + A] * s / 2) + EllipticF[phizero, ksq], ksq] ^2] /
         JacobiDN[(Sqrt[2 + A] * s / 2) + EllipticF[phizero, ksq], ksq]) - (EllipticE[phizero, ksq]
        Sqrt[1 - ksq * JacobiSN[EllipticF[phizero, ksq], ksq] ^2] / JacobiDN[EllipticF[phizero, ksq], ksq])},
  {s, 0, limsup}, PlotLabel → "Analytical solution of X(S)",
  AxesLabel → {S, Y[S]},
  PlotStyle → {Red},
  PlotLegends → {"Analytical"}]
graphyan = Plot[H12 + Sqrt[2 - A] *
    JacobiSN[(-Sqrt[2 + A] / 2) * s + EllipticF[-ArcSin[Sqrt[(2 * Cos[theta] - A) / (2 - A)]], ksq], ksq],
  {s, 0, limsup}, PlotLabel → "Analytical solution of Y(S)", AxesLabel → {S, Y[S]},
  PlotStyle → {Red}, PlotLegends → {"Analytical"}]
graphoman = Plot[2 * JacobiAmplitude[((Sqrt[2 - A] * s / 2)) + EllipticF[theta / 2, 2 / (2 - A)], 4 / (2 - A)],
  {s, 0, limsup}, PlotLabel → "Analtyical solution of Ω(S)",
  AxesLabel → {S, Ω[S]}, PlotStyle → {Red}, PlotLegends → {"Analytical"}]
Show[graphx, graphxan, PlotLabel → "Analytical Solution vs. Numerical Solution for X(S)"]
Show[graphy, graphyan, PlotLabel → "Analytical Solution vs. Numerical Solution for Y(S)"]
Show[grapho, graphoman, PlotLabel → "Analytical Solution vs. Numerical Solution for Ω(S)"]
```

Figure C.1: Mathematica script showing the commands to solve the system of differential equations and the commands to plot the analytical solution.

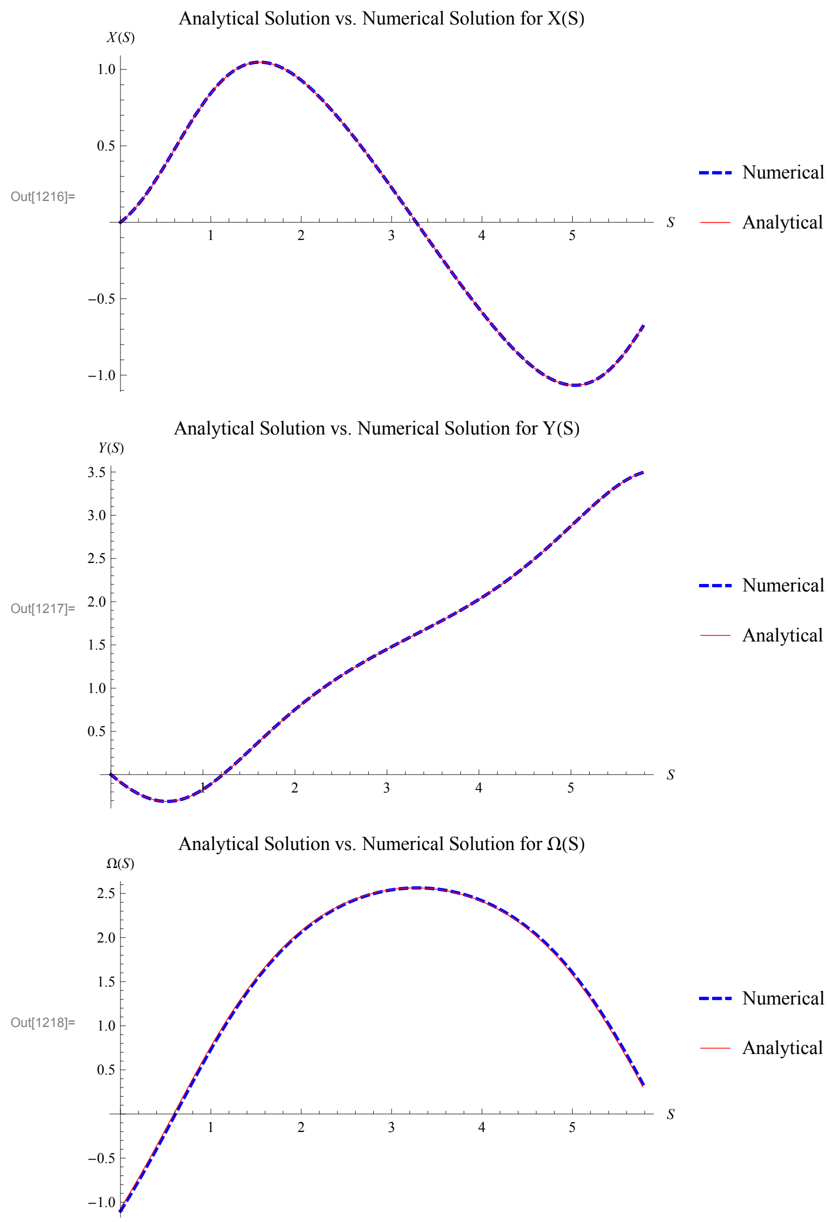

Figure C.2: Mathematica output showing the comparison between the analytical and numerical solution for $X(S)$, $Y(S)$ and $\Omega(S)$.

Appendix D

Elliptic integrals and elliptic functions

The incomplete elliptic integral of the first and second kind are defined respectively as

$$u = \mathbf{F}(\Theta, \kappa) = \int_0^{\Theta} \frac{d\theta}{\sqrt{1 - \kappa^2 \sin^2 \theta}}, \tag{D.1}$$

$$u = \mathbf{E}(\Theta, \kappa) = \int_0^{\Theta} \sqrt{1 - \kappa^2 \sin^2 \theta}\, d\theta. \tag{D.2}$$

In these expressions, κ is the elliptic modulus and the angle Θ is called the amplitude of u. The Jacobi amplitude is the inverse function of $\mathbf{F}(\Theta, \kappa)$, so that

$$\Theta = \mathbf{am}(u, k) = \mathbf{F}^{-1}(u, k). \tag{D.3}$$

The Jacobi functions are defined as follows

$$\sin\Theta = \mathbf{sn}(u, \kappa), \tag{D.4}$$

$$\cos\Theta = \mathbf{cn}(u, \kappa), \tag{D.5}$$

$$\sqrt{1 - k^2 \sin^2 \Theta} = \mathbf{dn}(u, k). \tag{D.6}$$

Additional properties of the elliptic integrals and elliptic functions can be found in the book by Abramowitz and Stegun [37].

Appendix E

Derivation of the Gibbs' limit

In his work, Gibbs [21] derived the conditions under which a liquid surface remains pinned at the edge of a solid surface (see figure E.1)

$$\gamma_{sv} - \gamma_{sl} \geq \gamma_{lv} \cos\theta, \tag{E.1}$$

$$\gamma_{sl} - \gamma_{sv} \geq \gamma_{lv} \cos\alpha, \tag{E.2}$$

where γ are the surface tensions, and the subindices correspond to the interacting surfaces (liquid l, vapor v, solid s). These set of inequalities can be put in the following way:

$$-\cos\alpha \geq \frac{\gamma_{sv} - \gamma_{sl}}{\gamma_{lv}} \geq \cos\theta. \tag{E.3}$$

From Young's equation [21] we also have that if the liquid is resting on a flat surface, the following equilibrium condition holds:

$$\gamma_{sv} - \gamma_{sl} = \gamma_{lv} \cos\theta_{eq}. \tag{E.4}$$

Therefore, we can relate the Gibbs' conditions to the equilibrirum angle as follows:

$$-\cos\alpha \geq \cos\theta_{eq} \geq \cos\theta, \tag{E.5}$$

which is equivalent to

$$\cos\theta_{eq} \geq \cos\theta, \tag{E.6}$$

$$-\cos(2\pi - \theta - \phi) \geq \cos\theta_{eq}. \tag{E.7}$$

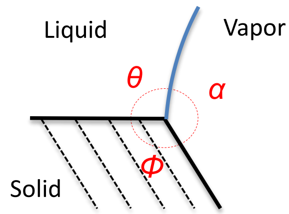

Figure E.1: The meniscus pinned at the edge of a solid surface must satisfy the Gibbs' conditions.

From the first inequality it follows that, for all values of θ and θ_{eq} between 0 and π,

$$\theta \geq \theta_{eq}. \tag{E.8}$$

We simplify the second inequality using trigonometric properties. Since $-\cos(2\pi - \theta - \phi) = \cos(\theta + \phi - \pi)$, we have that

$$\cos(\theta + \phi - \pi) \geq \cos\theta_{eq}. \tag{E.9}$$

For all values of $\theta + \phi - \pi$ between 0 and π, it follows that

$$\theta \leq \pi - \phi + \theta_{eq}. \tag{E.10}$$

Putting the two inequalities together yields the Gibbs' limits in terms of the contact angles:

$$\theta_{eq} \leq \theta \leq \pi - \phi + \theta_{eq}. \tag{E.11}$$

This condition put in terms of the supplementary angle of θ gives equation (3.75) in section 3.5.2. In order for the meniscus to stay pinned, the strict inequalities must be satisfied. Whenever the equality holds, the meniscus is displaced to either of the flat surfaces, receding or spilling-over. It can also be seen that if we have a flat surface, i.e. $\phi = \pi$, the Gibbs condition reduces to the equilibrium condition given by equation (E.4), which is the classic Young's equation. In case the reader is interested, the work by White [66] provides a theoretical explanation of the Gibbs' limit using variational principles.

Bibliography

[1] M.L. Anderson, A.P. Bassom, and N. Fowkes. Exact solutions of the Laplace-Young equation. *Proceedings of The Royal Society A*, 462:3645 – 3656, 2006.

[2] St Balint and A.M. Balint. The effect of the pressure difference across the free surface on the static meniscus shape in the case of ribbon growth by edge-defined film-fed growth (E.F.G) method. *Journal of Crystal Growth*, 311:32–37, 2008.

[3] C.E. Bleil. A new method for growing crystal ribbons. *Journal of Crystal Growth*, 5:99–104, 1969.

[4] O. Bolza. *Lectures on the Calculus of Variations.* Chelsea Publishing Company, New York, 1960.

[5] L. Braescu. Shape of menisci in terrestrial dewetted Bridgman growth. *Journal of Colloids and Interface Science*, 319:309–315, 2008.

[6] L. Braescu, S. Epure, and T. Duffar. Mathematical and numerical analysis of capillarity problems and processes. In *Crystal Growth Processes Based on Capillarity: Czochralski, Floating Zone, Shaping and Crucible Techniques*, pages 465–524. John Wiley and Sons, Ltd, New York, 2010.

[7] R.A. Brown. Theory of Transport Processes in Single Crystal Growth from the Melt. *AICHE Journal*, 34:881–991, 1998.

[8] B. Ceccaroli and O. Lohne. Solar Grade Silicon Feedstock. In *Handbook of Photovoltaic Science and Engineering*, pages 169–193. John Wiley and Sons, Ltd, United Kingdom, 2011.

[9] B. Chalmers. High Speed Growth of Sheet Crystals. *Journal of Crystal Growth*, 70:3–10, 1984.

[10] B. Chalmers, H.E. LaBelle Jr, and A.I. Mlavsky. Edge-defined Film Fed Crystal Growth. *Journal of Crystal Growth*, 13-14:84–87, 1972.

[11] J.A Champion, B.J. Keene, and S. Allen. Wetting of refractory materials by molten metallides. *Journal of Materials Science*, 8:423–426, 1973.

[12] T.F. Ciszek. Edge-defined, Film Fed Growth (EFG) of Silicon Ribbons. *Materials Research Bulletin*, 7:731–737, 1972.

[13] R.F. Clark. Method and apparatus for the production of crystalline silicon substrates. US Patent 8,262,795 B2, September 11, 2012.

[14] S.R. Coriell, R.F. Boisvert, G.B. McFadden, L.N. Brush, and J.J. Favier. Morphological Stability of a Binary Alloy during Directional Solidification. *Journal of Crystal Growth*, 140:139–147, 1994.

[15] P. Daggolu, A. Yeckel, and J.J Derby. An analysis of segregation during horizontal ribbon growth of silicon. *Journal of Crystal Growth*, 390:80–87, 2014.

[16] S. Epure. Analytical and numerical studies of the meniscus equation in the case of crystals grown in zero gravity conditions by the dewetted Bridgman technique. *International Journal of Mathematical Models and Methods in Applied Sciences*, 4:50–57, 2010.

[17] G. Flamant, V. Kurtcuoglu, J. Murray, and A. Steinfeld. Purification of metallurgical grade silicon by a solar process. *Solar Energy Materials and Solar Cells*, 90:2099–2106, 2006.

[18] Renewable Energy Policy Network for the 21st Century. *Renewables 2014 Global Status Report*, 2014.

[19] A.R. Forsyth. *Calculus of Variations*. Dover Publications, Inc, New York, 1960.

[20] C. Fox. *An Introduction to the Calculus of Variations*. Dover Publications, Inc, New York, 1987.

[21] J.W. Gibbs. *The Collected Works of J. Willard Gibbs*, volume 1. Yale University Press Reprint, New Haven, 1948.

[22] M.E. Glicksman and P.W. Voorhees. Analysis of morphologically stable horizontal ribbon growth. *Journal of Electronic Materials*, 12:161–179, 1983.

[23] M. Gratzel. Mesoscopic Solar Cells for Electricity and Hydrogen Production from Sunlight. *Chemistry Letters*, 34:8–14, 2005.

[24] K. Greven, A. Ludwig, and P.R. Sahm. Time dependent interface stability during rapid solidification. *Journal of Applied Physics*, 86:3682–3687, 1999.

[25] D.T.J. Hurle. Surface aspects of crystal growth from the melt. *Advances in Colloids and Interface Science*, 15:101–130, 1981.

[26] D.T.J. Hurle. Analytical representation of the shape of the meniscus in Czochralski growth. *Journal of Crystal Growth*, 63:13–17, 1983.

[27] P.L. Kellerman, F. Carlson, and F. Sinclair. Sheet thickness control. US Patent US 2010/0038826 A1, February 18, 2010.

[28] P.L. Kellerman, F. Carlson, and F. Sinclair. Method for continuous formation of a purified sheet from a melt. US Patent 8,545,624 B2, October 1, 2013.

[29] P.L. Kellerman, F. Carlson, and F. Sinclair. Method of controlling a thickness of a sheet formed from a melt. US Patent 8,475,591 B2, July 2, 2013.

[30] P.L. Kellerman and F. Sinclair. Floating sheet production apparatus and method. US Patent 7,855,087 B2, December 21, 2010.

[31] P.L. Kellerman, D. Sun, B. Helebrook, and S.H. Harvey. Removing a sheet from the surface of a melt using elasticity and buoyancy. US Patent Application number 20110272115, November 10, 2011.

[32] P.L. Kellerman, G.D. Thronson, and D. Sun. Removing a sheet from the surface of a melt using gas jets. US Patent 8,685,162 B2, April 1, 2014.

[33] B. Kudo. Improvements in the horizontal ribbon growth technique for single crystal silicon. *Journal of Crystal Growth*, 50:247–259, 1980.

[34] H. Lange. Ribbon Growth on Substrate RGS - A New Approach to High Speed Growth of Silicon Ribbons for Photovoltaics. *Journal of Crystal Growth*, 104:108–112, 1990.

[35] P.S. Laplace and N. Bowditch. *Celestial Mechanics*, volume 4. Chelsea Pub. Co, New York, 1966.

[36] A.M. Legendre. *Traite des Fonctions Elliptiques*, volume 1. Huzard-Courcier, Paris, 1828.

[37] Abramowitz M. and I.A. Stegun. *Handbook of Mathematical Functions with Formulas, Graphs, and Mathematical Tables*. Dover, New York, 1972.

[38] B.H. Mackintosh, P.L. Kellerman, and D. Sun. Method for achieving sustained anisotropic crystal growth on the surface of a silicon melt. US Patent US 013/0213295 A1, August 22, 2013.

[39] K. Mazuruk and M.P. Volz. Static stability of menisci detached Bridgman growth. *Physics of Fluids*, 25:094106, 2013.

[40] K. Mika and W. Uelhoff. Shape and stability of menisci in Czochralski growth and comparison with analytical approximations. *Journal of Crystal Growth*, 30:9–20, 1975.

[41] W.W. Mullins and R.F. Sekerka. Stability of a Planar Interface during Solidification of a Dilute Binary Allow. *Journal of Applied Physics*, 35:444–451, 1964.

[42] A.D. Myshkis, V.G. Babskii, Kopachevskii N.D., L.A. Slobozhanin, and A.D Tyuptsov. *Low-Gravity Fluid Mechanics*. Springer-Verlag, Berlin, 1987.

[43] N.M. Ozisik. *Finite Difference Methods in Heat Transfer*. CRC Press, Boca Raton, FL, USA, 1994.

[44] Daggolu. P., A. Yeckel, C.E. Bleil, and J.J Derby. Thermal-capillary analysis of the horizontal ribbon growth of silicon crystals. *Journal of Crystal Growth*, 355:129–139, 2012.

[45] Daggolu. P., A. Yeckel, C.E. Bleil, and J.J Derby. Stability limits for the horizontal ribbon growth of silicon crystals. *Journal of Crystal Growth*, 363:132–140, 2013.

[46] E. Pitts. The stability of pendent liquid drops. Part 1. Drops formed in a narrow gap. *Journal of Fluid Mechanics*, 59:753–767, 1973.

[47] M. Rappaz and Ch.-A. Gandin. Probabilistic Modelling of Microstructure Formation in Solidification Processes. *Acta Metallurgica et Materialia*, 41:345–360, 1993.

[48] C.A. Rhodes, M.M. Sarraf, and C.H. Liu. Investigation of the meniscus stability in horizontal crystal ribbon growth. *Journal of Crystal Growth*, 50:94–101, 1980.

[49] H. Rodriguez, I. Guerrero, W. Koch, A.L. Endrös, D. Franke, C. Häbler, J.P. Kalejs, and H.J. Möller. Bulk Crystal Growth and Wafering for PV. In *Handbook of Photovoltaic Science and Engineering*, pages 218–239. John Wiley and Sons, Ltd, United Kingdom, 2011.

[50] C.A. Rowland, P.L. Kellerman, F. Sinclair, J.G. Blake, and N.P.T Bateman. Floating sheet measurement apparatus and method. US Patent US2009/0231597 A1, September 17, 2009.

[51] R.G. Seidenstricker. Dendritic Web Silicon for Solar Cell Application. *Journal of Crystal Growth*, 39:17–22, 1977.

[52] R.G. Seidenstricker and R.H. Hopkins. Silicon Ribbon Growth by the Dendritic Web Process. *Journal of Crystal Growth*, 50:221–235, 1980.

[53] W. Shockley. Process for growing ssingle crystals. U.S. Patent 3,031,275, April 24,1962.

[54] F. Sinclair and P.L. Kellerman. Apparatus for float grown crystalling sheets. US Patent US014/0096713 A1, April 10, 2014.

[55] D.M Stefanescu. *Science and Engineering of Casting Solidification*. Springer, New York, 2009.

[56] T. Surek. Theory of shape stability in crystal growth from the melt. *Journal of Applied Physics*, 47:4384–4393, 1976.

[57] T. Surek and B. Chalmers. The direction of growth of the surface of a crystal in contact with its melt. *Journal of Crystal Growth*, 8:1–11, 1975.

[58] T. Surek, B. Chalmers, and A.I. Mlavsky. The Edge-defined Film Fed Growth of Controlled Shape Crystals. *Journal of Crystal Growth*, 42:453–465, 1977.

[59] J.C. Swartz, T. Surek, and B. Chalmers. The EFG process applied to the growth of silicon ribbons. *Journal of Electronic Materials*, 4:255–279, 1975.

[60] V.A. Tatarchenko. Capillary shaping in crystal growth from melts: I. Theory. *Journal of Crystal Growth*, 37:272–284, 1977.

[61] V.A. Tatarchenko. The possibility of shape stability in capillary crystal growth and practical realization of shaped crystals. In *Crystal Growth Processes Based*

on Capillarity: Czochralski, Floating Zone, Shaping and Crucible Techniques, pages 51–114. John Wiley and Sons, Ltd, New York, 2010.

[62] V.A. Tatarchenko, V.S. Uspenski, E.V. Tatarchenko, J.Ph. Nabot, and T. Duffar. Theoretical model of crystal growth shaping process. *Journal of Crystal Growth*, 180:615–626, 1997.

[63] R. Thronson and P.L. Kellerman. Floating silicon method (FSM). Technical report, Applied Materials, Varian Semiconductor/DOE Final Report, December 21, 2013.

[64] G. Tryggvason, B. Bunner, A. Esmaeeli, D. Juric, N. Al-Rawahi, W. Tauber, J. Han, S. Nas, and Y.-J. Jan. A Front-Tracking Method for the Computations of Multiphase Flow. *Journal of Computational Physics*, 169:708–759, 2001.

[65] M.P. Volz and K. Mazuruk. Existence and shapes of menisci in detached Bridgman growth. *Journal of Crystal Growth*, 321:29–35, 2011.

[66] L.R. White. The equilibrium of a liquid drop on a nonhorizontal substrate and the Gibbs criteria for advance over a sharp edge. *Journal of Colloid and Interface Science*, 73:256–259, 1980.

[67] J.A. Zoutendyk. Theoretical analysis of heat flow in horizontal ribbon growth from a melt. *Journal of Applied Physics*, 49:3927–3932, 1978.

[68] J.A. Zoutendyk. Analysis of forced convection heat flow effects in Horizontal Ribbon Growth from the melt. *Journal of Crystal Growth*, 50:83–93, 1980.